Recovery Based Error Estimation for the Method of Moments

by

Willem Jacobus Strydom

Thesis presented in partial fulfilment of the requirements for the degree of Master of Engineering in the Faculty of Engineering at Stellenbosch University

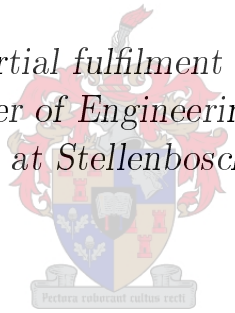

Department of Electrical and Electronic Engineering,
University of Stellenbosch,
Private Bag X1, Matieland 7602, South Africa.

Supervisor: Professor Matthys M. Botha

March 2015

Declaration

By submitting this thesis electronically, I declare that the entirety of the work contained therein is my own, original work, that I am the sole author thereof (save to the extent explicitly otherwise stated), that reproduction and publication thereof by Stellenbosch University will not infringe any third party rights and that I have not previously in its entirety or in part submitted it for obtaining any qualification.

March 2015

Abstract

The Method of Moments (MoM) is routinely used for the numerical solution of electromagnetic surface integral equations. Solution errors are inherent to any numerical computational method, and error estimators can be effectively employed to reduce and control these errors. In this thesis, gradient recovery techniques of the Finite Element Method (FEM) are formulated within the MoM context, in order to recover a higher-order charge of a Rao-Wilton-Glisson (RWG) MoM solution. Furthermore, a new recovery procedure, based specifically on the properties of the RWG basis functions, is introduced by the author. These recovered charge distributions are used for *a posteriori* error estimation of the charge. It was found that the newly proposed charge recovery method has the highest accuracy of the considered recovery methods, and is the most suited for applications within recovery based error estimation.

In addition to charge recovery, the possibility of recovery procedures for the MoM solution current are also investigated. A technique is explored whereby a recovered charge is used to find a higher-order divergent current representation. Two newly developed methods for the subsequent recovery of the solenoidal current component, as contained in the RWG solution current, are also introduced by the author. *A posteriori* error estimation of the MoM current is accomplished through the use of the recovered current distributions. A mixed second-order recovered current, based on a vector recovery procedure, was found to produce the most accurate results.

The error estimation techniques developed in this thesis could be incorporated into an adaptive solver scheme to optimise the solution accuracy relative to the computational cost.

Opsomming

Die Moment Metode (MoM) vind algemene toepassing in die numeriese oplossing van elektromagnetiese oppervlak integraalvergelykings. Numeriese foute is inherent tot die prosedure: foutberamingstegnieke is dus nodig om die betrokke foute te analiseer en te reduseer. Gradiënt verhalingstegnieke van die Eindige Element Metode word in hierdie tesis in die MoM konteks geformuleer. Hierdie tegnieke word ingespan om die oppervlaklading van 'n Rao-Wilton-Glisson (RWG) MoM oplossing na 'n verbeterde hoër-orde voorstelling te neem. Verder is 'n nuwe lading verhalingstegniek deur die outeur voorgestel wat spesifiek op die eienskappe van die RWG basis funksies gebaseer is.

Die verhaalde ladingsverspreidings is geïmplementeer in *a posteriori* fout beraming van die lading. Die nuut voorgestelde tegniek het die akkuraatste resultate gelewer, uit die groep verhalingstegnieke wat ondersoek is.

Addisioneel tot ladingsverhaling, is die moontlikheid van MoM-stroom verhalingstegnieke ook ondersoek. 'n Metode vir die verhaling van 'n hoër-orde divergente stroom komponent, gebaseer op die verhaalde lading, is geïmplementeer. Verder is twee nuwe metodes vir die verhaling van die solenodiale komponent van die RWG stroom deur die outeur voorgestel. *A posteriori* foutberaming van die MoM-stroom is met behulp van die verhaalde stroom verspreidings gerealiseer, en daar is gevind dat 'n gemengde tweede-orde verhaalde stroom, gebaseer op 'n vektor metode, die beste resultate lewer.

Die foutberamingstegnieke wat in hierdie tesis ondersoek is, kan in 'n aanpasbare skema opgeneem word om die akkuraatheid van 'n numeriese oplossing, relatief tot die berekeningskoste, te optimeer.

Acknowledgements

The following people and organisations must be acknowledged for their support and special contribution to this project.

- My loving family, and especially my girlfriend, Stacy-Leigh, for their support and patience through the years of my studies.
- Professor Matthys M. Botha, for introducing me to the field of Computational Electromagnetics and for his outstanding academic guidance.
- Altair Development S.A. (Pty) Ltd. for the financial support they provided me with.
- The other office members of the Radar Lab, for sharing the postgraduate journey with me and always offering their support and insights during my research. Special thanks to Ryno and Anneke for keeping the coffee-bean supply steady!
- The University of Stellenbosch and the Department of Electrical and Electronic Engineering, for the excellent quality of education they provided me with.

Contents

List of Figures

List of Tables

Chapter 1

Introduction

Electromagnetic problems often revolve around the prediction of fields in the presence of complicated structures. Solving these problems involves extensive numerical procedures that aim to appropriately approximate Maxwell's equations. Surface integral equation formulations are discussed in several texts [1, 2]. Typically, a numerical solution is found on a sub-sectioned model (also referred to as a meshed model) that represents the surface of a structure. The numerical formulation represents surface currents on the structure with piecewise-polynomial basis functions, and a large linear system of equations is constructed and solved, by imposing boundary conditions on the fields. One such process, which is considered in this work, is known as the *Method of Moments* (MoM).

The MoM is a method for solving surface integral equations of radiation and scattering and is one of the most widely used numerical methods in the field of computational electromagnetics (CEM). The use of MoM is prevalent in scattering applications, such as radar cross section predictions, as well as radiation applications, such as antenna analyses and electromagnetic interference and compatibility analyses. The electric field integral equation (EFIE) formulation of the MoM, suited to arbitrary surface modelling of open and closed perfect electric conducting (PEC) bodies, is considered in this work.

Although simulation forms a central part of any design or analysis process, the approximate nature of the MoM solution should always be considered. Inherent to the MoM procedure is a solution error due to the discretisation approximation. An increase in the order of the polynomial basis functions employed, known as *p-adaptation*, or a decrease in the element size of the surface discretisation, known as *h-adaptation*, can be applied to reduce the solution error [3]. It should however be apparent that the error can only be minimised, and never completely removed. Control over the solution error is still desirable, and as such, reliable estimation of the error is needed. The application of adaptive refinement procedures can also be selectively applied to regions of high local error in the mesh, effecting a desired reduction in the global error while minimising the computational costs involved. These procedures are desirable simulation tools that are heavily reliant on the availability of a local estimate of the solution error.

With this in mind, the aim of this research is to formulate an a posteriori method for global and local quantitative error estimation within the Rao-Wilton-Glisson (RWG) MoM.

Chapter 2 offers an overview of MoM error estimation, as well as some related work within the *Finite Element Method* (FEM) context. It also provides the motivation for the focus of this research, recovery based error estimation, which is a well-known topic in the FEM-context but an unexplored topic within the MoM-context. The EFIE-based MoM formulation is presented in Chapter 3. The structure of Chapter 3 is similar to the paper of Rao, Wilton, and Glisson [4], where a mixed first-order MoM formulation is provided. Results obtained in this study are also compared with those presented in that paper. In Chapters 4 and 5, the topics of numerical integration and basis functions are explored. These themes are central to numerical methods and thus crucial to the development and implementation of a rigorous and accurate MoM formulation. Chapter 6 investigates some possible methods of charge recovery and looks at charge error estimators based on a recovered numerical charge. A new method for charge recovery, as developed by the author, is also introduced in this chapter. The concept of charge recovery is then extended to current recovery in Chapter 7. Two current recovery methods, developed by the author, are introduced in this chapter, and error estimations of the solution current are investigated and discussed. The document is concluded in Chapter 8 with a summary of the research. Recommendations for future research are also provided.

Chapter 2

Error Estimation: The Setting

CEM methods involve the discretisation of a continuum model of electromagnetic behaviour in order to obtain a numerical solution. Inherent to all these methods are numerical solution errors. Control, analysis and effective minimisation of the approximation error of a numerical solution rest heavily on the availability of a reliable estimate of such an error.

Broadly speaking, error estimators may be grouped according to *a priori* and *a posteriori* estimators [3]. The former is based on a theoretical approach that is independent of the problem data and numerical solution, while the latter is derived directly from the numerical solution. This study focuses on *a posteriori* error estimation, as needed for adaptive refinement in the MoM.

2.1 Error estimation in the Method of Moments

Two approaches for dealing with the numerical error in the MoM are often encountered. The first involves simple validation and verification procedures that employ test cases and analytical solutions. The second is the theoretical functional analysis approach of the applied mathematics community.

For the engineer using a CEM tool, indirect methods such as benchmarking problems with quasi-analytical solutions or measured data are of little use. Benchmarking of a MoM solver would only serve to verify a numerical implementation against pre-validated solutions. The issue of a measure of the solution accuracy of a general problem is not addressed. The *a priori* theoretical approach to the problem of error analysis seen in the applied mathematics community also does not deal with this problem. Numerical analysts studying computational methods often attempt to quantify the rate of reduction in the error of the solution of a given problem as the mesh is refined. The asymptotic convergence rate of the MoM, and whether the solution converges to the correct answer for a given problem, are well documented by many authors, including [5]. When quantitatively evaluating the solution accuracy of a particular problem, or driving an adaptive

model refinement, it is however desirable to have a problem-specific measure of the error. *a posteriori* error estimation, where the numerical solution itself is used to calculate a measure of the error, is required in such cases.

2.1.1 Residual based error estimators

In a basic MoM solver, the surface of a conducting structure is modelled by flat elements on which the surface current density is represented by an expansion of piecewise-linear basis functions. Each basis function is tangential on the local elements that form its support. The electric field integral equation (EFIE) relates this surface current to the scattered electric field $\mathbf{E^s}$ according to

$$\mathbf{E^s} = \mathcal{L}\,\mathbf{J}, \tag{2.1}$$

where $\mathcal{L}$ is a mathematical operator to be performed on the surface current $\mathbf{J}$. By utilising the known incident electric field $\mathbf{E^i}$, the boundary condition for the total electric field on the conducting surface, $\hat{\mathbf{n}} \times (\mathbf{E^i} + \mathbf{E^s}) = 0$, is enforced in a weighted-residual manner with a second set of tangential testing functions. For a full discussion of the formulation of the MoM, see Chapter 3.

Since the boundary condition is only satisfied in a weighted manner, a local non-zero residual exists according to

$$R(\mathbf{r}) = (\mathcal{L}\,\tilde{\mathbf{J}})_{tan} + \mathbf{E^i}_{tan}, \tag{2.2}$$

where $\tilde{\mathbf{J}}$ is the approximation of the true surface current $\mathbf{J}$. It is this local residual value that can be utilised to determine the numerical error of a MoM solution. A correlation of the true error $\mathbf{e} = \mathbf{J} - \tilde{\mathbf{J}}$ and the residual error has been established and illustrated in the literature [6, 7, 8].

A boundary condition error metric is introduced in [6] along with accurate expressions of scattered fields that are valid at observation points on the surface of the structure. This error metric allows an estimate of the numerical solution error to be constructed from Equation 2.2. It is further noted in [8], that care should be taken when computing the field values of the residual of Equation 2.2, as a similar method to that used in the MoM formulation would not yield insightful information. It is thus necessary to compute the residual error with an alternative formulation to obtain a useful measure of the error.

It is also possible to calculate the current approximation $\tilde{\mathbf{J}}$ from an overdetermined system of equations [9], for which the boundary condition can not be exactly satisfied at every testing point. A least-squares approach would yield an approximation for which the error in the residual is minimised. For such an approach, the error is extracted from the formulation of the original system of equations.

A residual error estimator can also be based on an evaluation of the boundary condition of the normal component of the total electric field on the surface of a closed PEC

structure [8]. The normal boundary condition is given as

$$\hat{\mathbf{n}} \cdot (\mathbf{E^i} + \mathbf{E^s}) = \frac{\rho_s}{\epsilon}, \tag{2.3}$$

with ρ_s the surface charge density at a point on the surface and ϵ the permittivity of the surrounding space. A measure of the accuracy with which the boundary condition is satisfied can be calculated in a local or global manner so as to predict the error of the numerical solution.

Yet another implicit *a posteriori* residual method can be constructed from local calculations that incorporate higher-order basis functions. In [10], such a method is suggested and shown to be computationally inexpensive, consistent and suitable for use within an adaptive refinement scheme.

2.1.2 Recovery based error estimators

The development of an *a posteriori* error estimator based on a post-processing recovery procedure is the primary goal of this thesis. This is a topic that has not received much attention in the literature, with most *a posteriori* error estimators being developed around the residual concept.

The notion behind a recovery based error estimator is built on a post-processing step that somehow provides an improved version of a derivative of the solution field. A detailed discussion of similar methods employed in the Finite Element Method (FEM), where the gradient of the solution field is recovered, can be found in [11]. Within the MoM context the value being recovered is the surface charge density, obtained as

$$\rho_s = -\frac{1}{j\omega}\nabla_s \cdot \mathbf{J}, \tag{2.4}$$

with $\omega = 2\pi f$ the angular frequency. The error in the charge may then be evaluated as the difference between the true charge ρ_s, and the charge associated with the solution current as

$$e_\rho = \rho_s - \tilde{\rho}_s, \tag{2.5}$$

where $\tilde{\rho}_s$ is the discontinuous charge related to a first-order MoM solution. A recovery procedure seeks to find an estimate of the true charge, with which an estimate of the charge error can be constructed as

$$e_\rho^* = \tilde{\rho}_s^* - \tilde{\rho}_s, \tag{2.6}$$

where $\tilde{\rho}_s^*$ is the recovered charge distribution.

Documented rigorous recovery based *a posteriori* error estimators for the MoM are not available in the mainstream literature. Some error estimation techniques that roughly resemble recovery based error estimation are constructed around the idea that significant discontinuities in the charge, or even a rapid change in the surface current, are indications of local errors. These methods, although somewhat useful, are not well documented and carry significant limitations.

2.2 Error estimation in the Finite Element Method

Within the FEM community, error estimation is a topic that is well explored. An exhaustive treatment of this subject does however not fall within the scope of this study, but some parallels may be drawn between *a posteriori* error estimation for the FEM and possible MoM adaptations. An extensive study of *a posteriori* error estimators in the FEM can be found in [11].

2.2.1 Residual based error estimators

Explicit residual based methods are thoroughly examined in [11]. With these methods, an upper bound for the error is derived based on inter-element field discontinuities.

Implicit residual based error estimators, where the global problem that characterises the residual error is replaced by a sequence of problems calculated on local sub-domains, are also well explored. The original ideas put forth by Babuska and Rheinboldt [12] have been extended and generalised for many different types of equations. Significant contributions to both explicit and implicit residual methods for the FEM in EM analysis were also made by Botha and Davidson in [13] and [14], respectively.

2.2.2 Gradient recovery based error estimators

The focus is now shifted towards error estimators in the FEM context that compare the derivative of the solution field to improved representations of the derivative, obtained through post-processing procedures. In the field of structural mechanics, the recovery of derivatives of a FEM solution is frequently implemented to arrive at more accurate stress values [11]. Consider the case where the original solution was sought in a space of piecewise-linear continuous functions on a conformal mesh of triangular elements. A gradient recovery scheme then attempts to find a continuous, piecewise-linear approximation to the discontinuous piecewise-constant gradient of the original solution. Such an approach, also referred to as a *smoothing* method, is based on the concept of the true gradient having a smooth and continuous form. As such, these methods seek to eliminate discontinuities between triangular elements by intelligently choosing fixed nodal values through a recovery procedure. The final recovered gradient is then a linear interpolation between recovered nodal values. Two existing nodal recovery methods are now discussed.

Nodal averaging

An especially simple method of nodal recovery involves the calculation of a fixed value for each node by averaging the gradient values around that node. Averaging techniques have been implemented in numerous FEM formulations for *a posteriori* error prediction applications [15]. Averaging is a rather crude method of recovery but remains appealing mainly due to the simplicity and low computational cost of an implementation. A similar approach is taken by Kelly et al. [16] with a FEM approximation of Poisson's equation in two dimensions. Their approach involves nodal averaging and a piecewise-bilinear interpolation on a mesh consisting of square elements.

Zienkiewicz-Zhu patch recovery

The nodal derivative recovery procedure of a FEM solution in one and two dimensions, proposed by Zienkiewicz and Zhu [17], has been widely cited since its publication. This method may be applied to a two-dimensional first-order FEM discretisation. The basis functions used in such a discretisation, are the first-order Lagrange basis functions, which are unity at a single node, and zero at all other nodes [2]. For a full description of these basis functions, refer to Section 5.3.2. The *patch recovery* procedure is a local method that recovers a nodal value by looking at the data from the union of elements that share the relevant vertex node. This *ZZ-patch* is also the support of the first-order basis function used in the discretisation.

A first-order polynomial representation is employed in a least squares fit to derivative values at the centroids of elements within the local patch. From this polynomial fit, the derivative value at the shared central node of the patch is recovered. Linear interpolation is then applied after recovering all nodal values [17].

For completeness, it is noted that an interesting method has been proposed recently by Horváth and Izsák in [18]. Here the ideas of an implicit residual and a patch recovery approach are combined.

2.2.3 Applicability to the Method of Moments

Many concerns should be addressed when considering adaptations of FEM based procedures to MoM problems. Firstly, both nodal averaging and the ZZ-recovery enforce global continuity, even though numerical charge distributions associated with typical higher-order MoM solutions do not. Enforcing continuity at surface junctions is not sensible, and the performance of these methods will degrade at junctions.

Secondly, the MoM is to be formulated for arbitrary surfaces in three-dimensional space. This would complicate a straightforward implementation of the ZZ-procedure, since the elements surrounding a vertex node are not necessarily co-planar, and a polynomial function could not be directly employed if they are not.

Lastly, with open structures, choices need to be made with regards to the recovery of nodal values that fall on the boundary of the surface. The charge of a MoM solution often varies most rapidly at and near domain edges, and the performance of a recovery procedure at these elements is thus of particular importance.

2.3 Conclusions

This study seeks to develop an *a posteriori* estimate of the error in a MoM solution, based on a procedure developed around charge recovery, with the goal of evaluating the solution accuracy of a particular problem or driving an adaptive refinement procedure. The ideas of averaging and the ZZ-recovery procedure form a suitable starting point, with parallels between the FEM process and the MoM drawn. The problems encountered when considering the MoM adaptation of these methods are dealt with in Chapter 6.

Chapter 3

Formulation of the Method of Moments

This chapter provides a formal overview of the Method of Moments (MoM) as well as an explicit discussion of the author's implementation of a mixed first-order MoM solver. Three-dimensional perfectly conducting radiators and scatterers are considered, with the underlying theory based on the work presented by Rao, Wilton, and Glisson [4]. Generated results are also compared to results that can be found in [4].

3.1 The Rao-Wilton-Glisson (RWG) MoM formulation for arbitrary surfaces

In this section, an integral equation for the surface current on a conducting structure is derived from the boundary conditions on the electric field. The MoM formulation that is discussed solves the integral equation with the use of a set of expansion functions and a testing procedure as introduced by [4].

The frequency domain based MoM is concerned with obtaining a mathematical expression for the discretised phasor current distribution on an arbitrary electromagnetic scatterer or radiator. Such structures are modelled using planar triangular patch elements which are capable of accurately conforming to any geometrical surface or boundary [4]. A varying patch density, as determined by the surface geometry and current resolution requirements, can be used for the model. Integrodifferential equations, often simply referred to as integral equations [2], are formulated for the surface currents flowing on the structure. The formulation is typically achieved by imposing either the magnetic or the electric boundary condition on the surface of the structure. For closed structures, the magnetic field integral equation (MFIE) can be used. However, in arbitrary surface modelling, the electric field integral equation (EFIE) has the advantage of being applicable to both open and closed bodies and is therefore selected as the foundation for most MoM applications. The challenges of an EFIE implementation are related to the presence of derivatives appearing in conjunction with a singular kernel in the integral equation [4, 2, 3]. In the following section, the EFIE formulation is presented, based on the work discussed in [4].

3.1.1 Electric field integral equation (EFIE)

Consider an incident electric field, $\mathbf{E^i}$, inducing surface currents $\mathbf{J}$ on the surface S of a perfect electric conducting (PEC) structure. Such an incident field is defined to be the field due to an impressed source in the absence of the structure. For open structures, $\mathbf{J}$ represents the vector sum of surface currents on opposite sides of the surface, and as such, the normal components of the current must vanish on the boundary of the structure. The scattered electric field, $\mathbf{E^s}$, can then be calculated from the induced surface current by

$$\mathbf{E^s} = -j\omega\mathbf{A} - \nabla\Phi, \tag{3.1}$$

where $\mathbf{A}$ is the *magnetic vector potential*, defined as

$$\mathbf{A} = \frac{\mu}{4\pi}\int_s \mathbf{J}\cdot G(\mathbf{r},\mathbf{r}')\,dS' \tag{3.2}$$

and Φ is the *scalar potential*, defined as

$$\Phi = \frac{1}{4\pi\epsilon}\int_s \rho_s \cdot G(\mathbf{r},\mathbf{r}')\,dS'. \tag{3.3}$$

$G(\mathbf{r},\mathbf{r}')$ is the free-space scalar Green's function and can be expressed as

$$G(\mathbf{r},\mathbf{r}') = \frac{e^{-jk|\mathbf{r}-\mathbf{r}'|}}{4\pi|\mathbf{r}-\mathbf{r}'|}, \tag{3.4}$$

where $k = \omega\sqrt{\mu\epsilon} = 2\pi/\lambda$ is the wavenumber, λ is the wavelength, μ and ϵ are the permeability and permittivity of the surrounding medium, and $|\mathbf{r}-\mathbf{r}'|$ is the distance between an arbitrarily located source point $\mathbf{r}'$ and an observation point $\mathbf{r}$ on the surface S. The continuity equation gives the relation between the surface charge density, ρ_s, and the surface divergence of the current density as

$$\nabla_s \cdot \mathbf{J} = -j\omega\rho_s. \tag{3.5}$$

To derive an integral equation for the current $\mathbf{J}$, the boundary condition for the electric field on the PEC surface S is enforced as

$$\hat{\mathbf{n}} \times (\mathbf{E^i} + \mathbf{E^s}) = 0, \tag{3.6}$$

with $\hat{\mathbf{n}}$ the unit normal vector on S. The EFIE is then obtained as

$$-\,\mathbf{E^i}_{tan} = (-j\omega\mathbf{A} - \nabla\Phi)_{tan}\,, \quad \text{with } \mathbf{r} \text{ on } S. \tag{3.7}$$

Equation 3.7, together with 3.2–3.5, describes the relation between the *unknown* induced current $\mathbf{J}$ and the *known* incident field $\mathbf{E^i}$. The derivatives of $\mathbf{J}$, present in the formulation of the EFIE, necessitate a careful approach to the development of expansion functions. In the next section the basis functions used for discretising the surface current in [4] are discussed.

3.1.2 RWG basis functions

A mathematical approximation $\tilde{\mathbf{J}}$ of the current distribution $\mathbf{J}$, on an arbitrary PEC surface S, is to be obtained. It is assumed a model of S, using planar triangular patch elements, is available. A set of suitable basis functions $\mathbf{f}$, is required with which the surface current may be approximated as

$$\tilde{\mathbf{J}} = \sum_{n=1}^{N} I_n \mathbf{f}_n(\mathbf{r}) \cong \mathbf{J}, \tag{3.8}$$

where I_n belongs to the set of N coefficients needed for the discretisation. In this context, suitable basis functions would be functions defined for triangular elements, suited to the EFIE used for the underlying formulation. Furthermore, these functions need to be free of fictitious line or point charges [4]. The set of basis functions introduced here, known as the Rao-Wilton-Glisson (RWG) basis functions, is a set of functions defined at the N *interior* edges (i.e. edges not on the domain boundary) of the surface model. Figure 3.1 illustrates the n^{th} interior edge of a triangulated surface with its two associated triangles, T_n^+ and T_n^-.

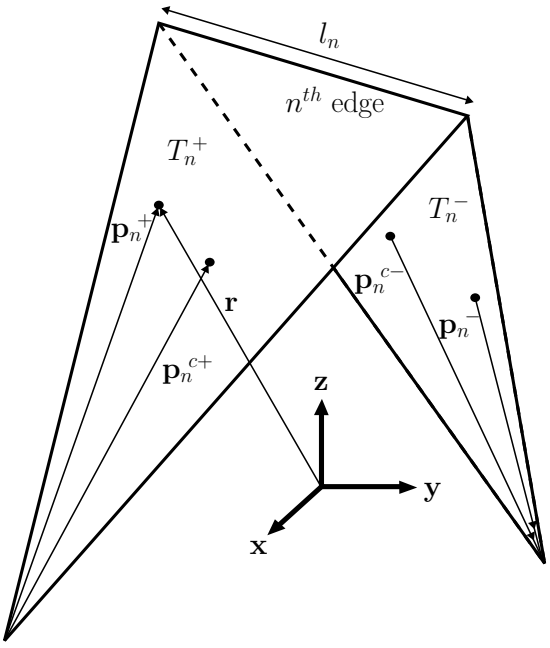

Figure 3.1: Triangle pair associated with interior edge n, along with geometrical parameters used during the construction of the RWG basis functions [4].

Each function in the set vanishes everywhere on the surface S, except in the two triangles $T_n^{\pm}$ attached to the associated edge. The edge associated coefficient I_n, describes the total current flowing over the n^{th} edge. The position of any point within a triangle, as described by the global coordinate position vector $\mathbf{r}$, can also be defined by the local position vector $\mathbf{p}_n^{\pm}$. This local position vector is defined in terms of the free vertex of $T_n^{\pm}$, as introduced

in Figure 3.1. The plus and minus designations of the triangles are determined by a choice of current reference direction across the n^{th} edge, and also determines whether the local position vector is directed from or towards the free vertex of the triangle. With these definitions and parameters in place, the RWG basis functions are given as

$$\mathbf{f}_n(\mathbf{r}) = \begin{cases} \dfrac{l_n}{2A_n^+}\,\mathbf{p}_n^+ & \mathbf{r} \text{ in } T_n^+ \\ \dfrac{l_n}{2A_n^-}\,\mathbf{p}_n^- & \mathbf{r} \text{ in } T_n^- \\ 0 & \text{otherwise,} \end{cases} \tag{3.9}$$

where l_n is the length of the n^{th} edge and $A_n^{\pm}$ is the area of triangle $T_n^{\pm}$.

When using RWG basis functions to approximate a surface current, as in Equation 3.8, a few important observations can be made. Firstly, $\mathbf{f}_n$ requires no line charges to exist along the boundary formed by the triangle pair $T_n^{\pm}$ since the current of this basis function has no component normal to this boundary. Secondly, $\mathbf{f}_n$ requires no line charges to exist along the n^{th} edge since the component of current normal to this edge is constant and continuous across the edge. This is ensured by the normalising factors present in $\mathbf{f}_n$, as seen in Equation 3.9. The function is divided by a factor equal to the normal component of the vectors $\mathbf{p}_n^{\pm}$ respectively. Lastly, it is found that the total charge associated with each basis function is zero. The surface charge density is seen from Equation 3.5, to be proportional to the surface divergence of $\mathbf{f}_n$, which is found as

$$\nabla_s \cdot \mathbf{f}_n(\mathbf{r}) = \begin{cases} \dfrac{l_n}{A_n^+} & \mathbf{r} \text{ in } T_n^+ \\ -\dfrac{l_n}{A_n^-} & \mathbf{r} \text{ in } T_n^- \\ 0 & \text{otherwise.} \end{cases} \tag{3.10}$$

The charge density is thus constant in each triangle and the total charge associated with the triangle pair $T_n^{\pm}$ is zero.

Up to three basis functions may have a non-zero value in a triangle, since a basis function is defined at each interior edge of the triangulated model, but only the basis function associated with a particular edge has a current component normal to that edge. Since the normal component of $\mathbf{f}_n$ is also normalised, the coefficients I_n in Equation 3.8 may be interpreted as the normal component of the current density flowing across the n^{th} edge. Edges on the domain boundary are omitted from the current approximation since current continuity requires the components of the current normal to the boundary edge on opposite sides of the surface to cancel out. The basis functions are also linearly independent of each other, since the current normal to an edge is an independent quantity. This observation is important when considering how the EFIE is utilised to calculate the set of current coefficients I_n, as discussed in the next section.

3.1.3 Galerkin testing

With the surface current now discretised, the next step in setting up the MoM is to develop a testing procedure for the EFIE. The goal of this process is to generate N independent equations to solve the N unknowns that are present in the EFIE when using the current approximation of Equation 3.8. One such testing procedure, known as the *Galerkin* method, uses the same expansion functions $\mathbf{f}_n$, developed in Section 3.1.2, as testing functions. This practical choice is popular in many MoM applications [2, 3]. By defining a symmetric inner product between two vectors as

$$\langle \mathbf{f}, \mathbf{g} \rangle \equiv \int_S \mathbf{f} \cdot \mathbf{g} \, dS, \tag{3.11}$$

the EFIE of Equation 3.7 can be tested with the set of N functions, $\mathbf{f}_m$ as follows

$$\langle \mathbf{E^i}, \mathbf{f}_m \rangle = j\omega \langle \mathbf{A}, \mathbf{f}_m \rangle + \langle \nabla \Phi, \mathbf{f}_m \rangle. \tag{3.12}$$

Applying the gradient operator in the last term of Equation 3.12 directly, is ill-advised, since the expansion of the surface charge ρ_s in Φ has a discontinuous piecewise-constant form, as can be seen in Equation 3.10. As explained in [4], utilising a surface vector calculus identity and the properties of the testing function $\mathbf{f}_m$, the last term in Equation 3.12 may be rewritten as

$$\begin{aligned} \langle \nabla \Phi, \mathbf{f}_m \rangle &= -\int_S \Phi \nabla_s \cdot \mathbf{f}_m \, dS \\ &= -\left(\frac{l_m}{A_{m^+}} \int_{T_{m^+}} \Phi \, dS - \frac{l_m}{A_{m^-}} \int_{T_{m^-}} \Phi \, dS \right) \end{aligned} \tag{3.13}$$

The differentiation operator ∇_s has thus been transferred to the testing function, which yields a finite result. At this stage, the authors in [4] approximate the average values of the incident electric field $\mathbf{E^i}$, the magnetic vector potential $\mathbf{A}$, and the scalar potential Φ over each triangle $T_m^{\pm}$ as the value of the respective quantities at the centre of the triangles. Such an approximation effectively eliminates the integration over the testing domain $T_m^{\pm}$, allowing a double integration to be approximated by a single integration in the source domain $T_n^{\pm}$. This procedure is however no different to doing a centre point numerical integration over the two triangles of the testing domain. Using a quadrature rule of only one point is justified in [4] by noting that the values being evaluated are locally smooth within each of the triangles.

All the developments presented here, are brought together in the next section, where the set-up and numerical evaluation of the MoM matrix equation elements are discussed.

3.1.4 MoM matrix equation derivation and solution

An $N \times N$ system of linear equations is described by the weighted EFIE of Equation 3.12, and the current approximation of Equation 3.8. This can be written in matrix form as

$$[Z]\{I\} = \{V\} \tag{3.14}$$

where $[Z]$ is an $N \times N$ impedance matrix, and $\{I\}$ and $\{V\}$ are current and voltage column vectors of length N respectively. The entries of $[Z]$ are calculated by

$$Z_{mn} = \frac{j\omega l_m}{2A_m^+} \int_{T_m^+} \mathbf{A}_{mn}{}^+ \cdot \mathbf{p}_m{}^+ \, dS + \frac{j\omega l_m}{2A_m^-} \int_{T_m^-} \mathbf{A}_{mn}{}^- \cdot \mathbf{p}_m{}^- \, dS - \frac{l_m}{A_m^+} \int_{T_m^+} \Phi_{mn}{}^+ \, dS + \frac{l_m}{A_m^-} \int_{T_m^-} \Phi_{mn}{}^- \, dS, \tag{3.15}$$

and the entries of $\{V\}$ are calculated by

$$V_m = \frac{l_m}{2A_m^+} \int_{T_m^+} \mathbf{E}_m{}^+ \cdot \mathbf{p}_m{}^+ \, dS + \frac{l_m}{2A_m^-} \int_{T_m^-} \mathbf{E}_m{}^- \cdot \mathbf{p}_m{}^- \, dS, \tag{3.16}$$

where

$$\mathbf{A}_{mn}{}^{\pm} = \frac{\mu}{4\pi} \int_s \mathbf{f}_n(\mathbf{r}') \, G(\mathbf{r}_m{}^{\pm}, \mathbf{r}') \, dS', \tag{3.17}$$

$$\Phi_{mn}{}^{\pm} = -\frac{1}{4\pi j\omega\epsilon} \int_s \nabla_{s'} \cdot \mathbf{f}_n(\mathbf{r}') \, G(\mathbf{r}_m{}^{\pm}, \mathbf{r}') \, dS', \tag{3.18}$$

and

$$\mathbf{E}_m{}^{\pm} = \mathbf{E}^{\mathbf{i}}(\mathbf{r}_m{}^{\pm}). \tag{3.19}$$

In the above equations, $\mathbf{r}_m{}^{\pm}$ is the position vector of the testing point as determined by the testing integrals of Equations 3.15 and 3.16. A centre point approximation is utilised by [4] when evaluating the testing integrals. The integration is accomplished with a single testing point per triangle, located at the triangle centroid $\mathbf{r}_m{}^{c\pm}$, and the testing integrals are evaluated as

$$\int_{T_m^{\pm}} [\cdot](\mathbf{r}_m{}^{\pm}) \, dS = [\cdot](\mathbf{r}_m{}^{c\pm}) \, A_m^{\pm}, \tag{3.20}$$

where $A_m^{\pm}$ is the area of triangle $T_m^{\pm}$.

The calculation of the impedance matrix entries Z_{mn}, is a computationally costly procedure of $\mathcal{O}(N^2)$. Although it does not decrease the complexity, [4] suggests using face pairs, as opposed to edge pairs, when setting up the integrals. This results in a reduction in computational cost, but forfeits the simplicity of an edge pair implementation [3]. Regardless of how the source and testing integrals are set up, there will be a number of integrations to be carried out in the triangular domains. Numerical quadrature techniques specially developed for triangular sub-domains can be utilised for this purpose. Care should however be taken when the $T_m^{\pm}$ source and $T_n^{\pm}$ testing domains overlap as the integrands for these cases are singular. Handling these cases generally requires an involved approach whereby the singularity is extracted and integrated analytically, or a singularity cancellation transformation method is applied. Using these methods to deal with the singularity appropriately will result in highly accurate terms of the impedance matrix but introduces extensive implementation overhead and additional computational costs. It is however found that the approach of using non-overlapping quadrature points for the two integrals adequately avoids the singularity to produce fair results. In the results presented in the next section, the use of a centre-point quadrature rule for the outer integral, and

a six-point quadrature rule for the inner integral is illustrated. The six-point quadrature rule does not have a node point at the triangle centroid, and the singularity is thus avoided. Singularity cancellation, as required for the accurate handling of general problems, is fully discussed in Section 4.3.

3.1.5 Verification

Two results given in [4] are replicated, to verify the formulation as presented in this section. The two problems analyse the dominant current component on square PEC plates of dimensions 0.15λ and 1.0λ respectively. Uniform plane wave excitation of an x-directed normally incident electric field is used. Both plates were meshed as in the

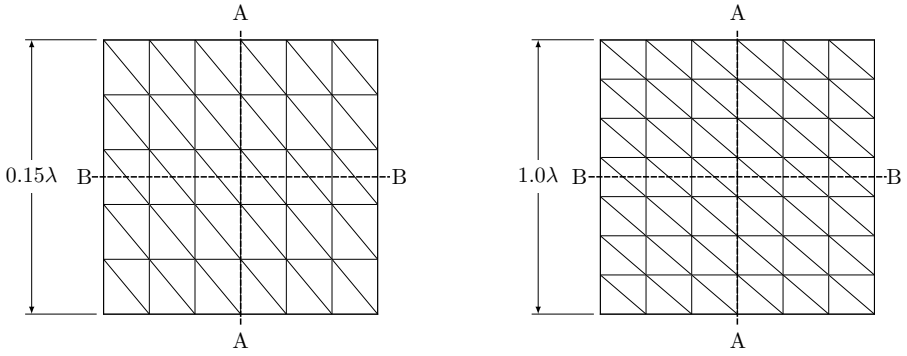

Figure 3.2: Two square PEC plates of dimensions 0.15λ and 1.0λ respectively. The meshes and principal cuts, AA and BB, as used in [4] are illustrated.

original and are shown in Figure 3.2. Cut AA is a centred vertical cut at $x = 0$ and cut BB is a centred horizontal cut at $y = 0$ (in the original the plates were however not centred at the origin). The meshes are generated by dividing the problem domain into rectangular cells that are each split into two triangles. A division in x and y of 6×5 for the first plate, and 6×7 for the second plate, results in a 60 triangle and 84 triangle mesh for the two respective problems. Such a meshing scheme allows for the straightforward extraction of the dominant current component, $\mathbf{J}_X$, along the principal cuts. Note that along the BB cuts, as in [4], only those edges with an x-directed current reference vector can be used in this simple extraction.

The results given in [4, Figs. 5 and 6] are compared to results computed with a code implementing this theory in Figures 3.3 and 3.4. In both figures, *Literature* refers to [4], *non-overlapping quadrature* refers to a one- and six-point quadrature rule combination, and *singularity cancellation* refers to solutions obtained with a Radial-Angular-R^1-Sqrt singularity cancellation scheme [19]. Singularity cancellation is fully discussed in Section 4.3.

The results for the electrically smaller problem of a 0.15λ square plate are illustrated in Figure 3.3. Some discrepancies between the data reported in [4] and a solution obtained

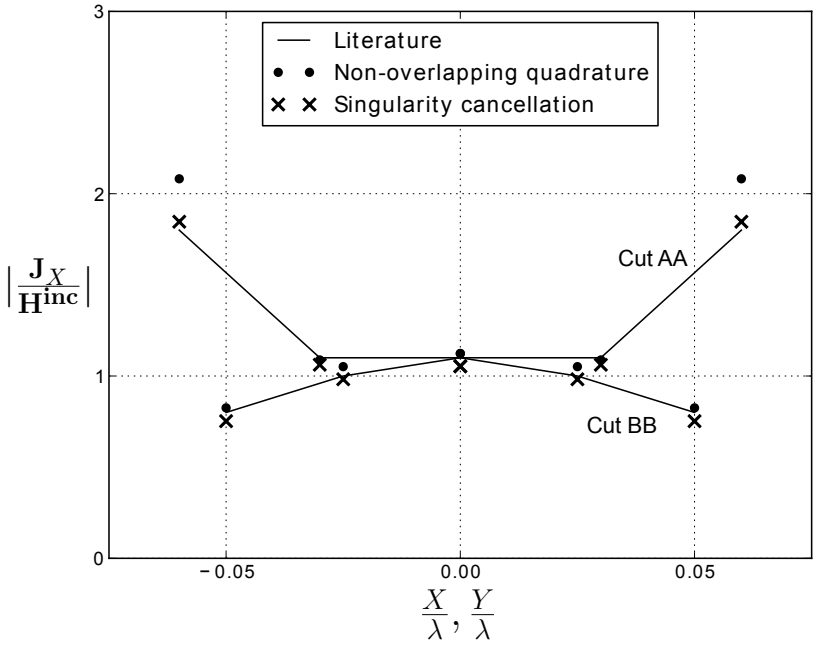

Figure 3.3: Dominant current component, $\mathbf{J}_X$, on a 0.15λ square flat plate.

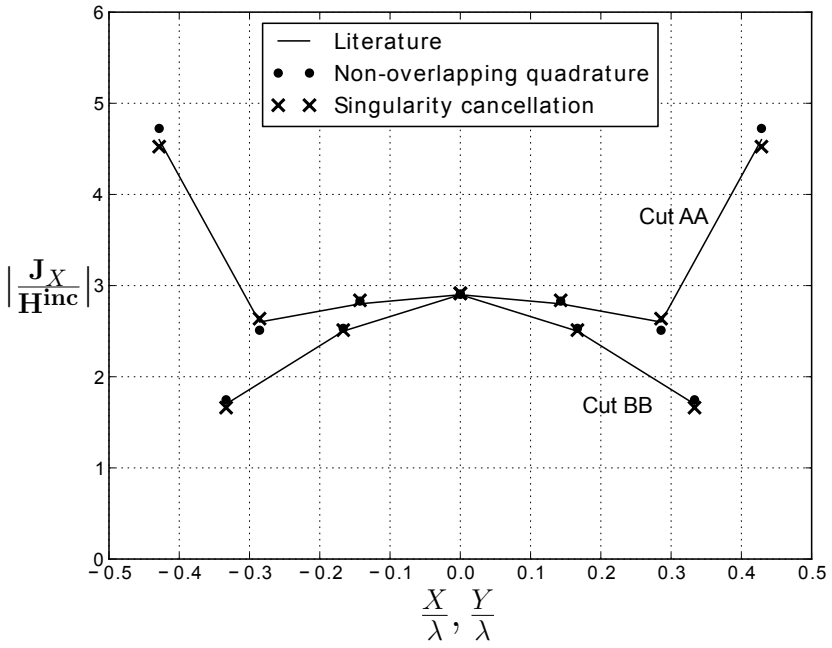

Figure 3.4: Dominant current component, $\mathbf{J}_X$, on a 1.0λ square flat plate.

with a scheme that merely avoids the singular point can be observed. It is clear that the rigorous handling of the singularity was needed and has effected a significant increase in the accuracy of the solution for this case. The 1.0λ square plate is excited in the resonant regime, and excellent agreement with [4] is observed with or without a rigorous handling

of the singularity. Further details of the differences in the physics of the two problems are discussed in [4].

In the following section, a practical implementation of the MoM formulation discussed in this section will be presented.

3.2 An implementation of the RWG MoM

The previous section introduced the MoM formulation as presented by Rao, Wilton and Glisson [4]. It was shown from first principles how the EFIE can be derived and how the surface current on an arbitrary structure can be computed. This section presents the practical implementation of a MoM solver along with some standard post-processing and visualisations.

3.2.1 Geometry set-up

Assuming that some suitable model of the structure under investigation is available, the first step is to discretise the surface into triangular sub-domains. This process is referred to as *meshing*. Many software packages and CAD programs offer meshing utilities, some of which are distributed as free software like Gmsh [20], and others that form part of commercial software packages like FEKO [21]. Triangular meshes can also be created in Matlab or GNU Octave with the Delaunay function. For very simple geometries, it could also be viable to define the nodes and connectivity that describes the simplest possible mesh manually, and to apply uniform mesh refinement until the desired mesh density is achieved.

It is common to set up a mesh with edge lengths chosen relative to the wavelength of the frequency at which the MoM will be solved. Values are typically selected in the range of $\frac{\lambda}{20} \leq h \leq \frac{\lambda}{10}$. Figure 3.5 shows comparative meshes for a $1.5\lambda \times 0.5\lambda$ PEC plate, as generated by four different approaches. With the surface successfully discretised, an RWG basis function is allocated to every non-boundary edge. A current reference direction is required for every basis function, but no convention is defined or necessary for this allocation. A suitable data structure is however needed to ensure consistent application.

3.2.2 Calculation of integrals and singularity cancellation

The required mathematical expressions for the RWG MoM matrix equation elements are listed in Section 3.1.4, on page 13. As mentioned, numerical quadrature techniques specifically tailored to the triangular sub-domains of the mesh can be utilised when evaluating these expressions. The approach involves approximating an integral by a summation of integrand samples. Each of the samples has a weighting coefficient applied in the summation. Gaussian quadrature for triangles is chosen for this task.

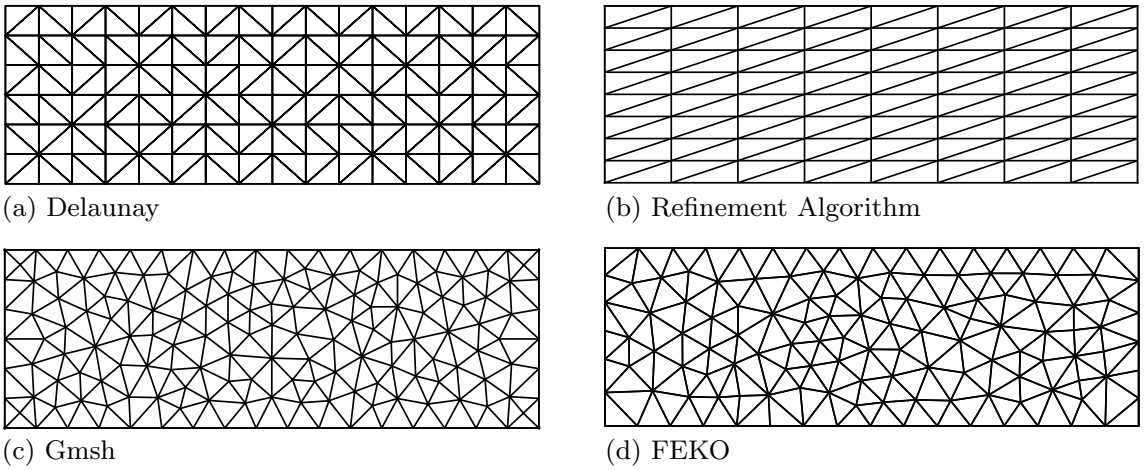

(a) Delaunay (b) Refinement Algorithm

(c) Gmsh (d) FEKO

Figure 3.5: A $1.5\lambda \times 0.5\lambda$ PEC plate triangulated with (a) the Delaunay function in GNU Octave, (b) a factor-8 uniform h-refined version of a two triangle mesh, (c) the free software package Gmsh and (d) the software package FEKO.

In the following discussion, simplex coordinates will be used as an alternate way to locate a point at $\mathbf{r}$ that falls on the surface of a triangle. A full discussion of simplex coordinates is offered in Section 5.2. At this stage it is sufficient to know that simplex coordinates (L_1, L_2, L_3) provide both a local description of a point that is independent of the triangle orientation and position, and also a global description in terms of Cartesian coordinates as

$$\mathbf{r} = L_1\mathbf{r}_1 + L_2\mathbf{r}_2 + L_3\mathbf{r}_3, \tag{3.21}$$

with $\mathbf{r}_1$, $\mathbf{r}_2$ and $\mathbf{r}_3$ the coordinates of the vertices of the triangle containing $\mathbf{r}$.

Gaussian quadrature schemes offer triangular symmetry with regards to the sample points and weights [22]. This is done by defining the sampling points in sets of three, where all three points carry the same weight, and the simplex coordinates of the sampling points take on the cyclical form of (α, β, β), (β, α, β) and (β, β, α). Naturally, the triangle centroid can also be utilised on its own as it inherently offers symmetry. Table 3.1 shows the one-, three- and six-point Gaussian quadrature rules. A full discussion of triangular Gaussian quadrature rules is provided in Section 4.2.2.

Table 3.1: The one-, three- and six-point Gaussian quadrature rules [22].

N	weight	L_1	L_2	L_3
1	1	1/3	1/3	1/3
3	1/3	2/3	1/6	1/6
6	0.10995	0.81685	0.09158	0.09158
	0.22338	0.10810	0.44595	0.44595

A visualisation of the six-point quadrature rule reported in Table 3.1 is provided in Figure 3.6 for two rotations of a triangle. The symmetry of the scheme is clearly observed, and it is also seen that the locations of the sampling points are unaffected by the rotation.

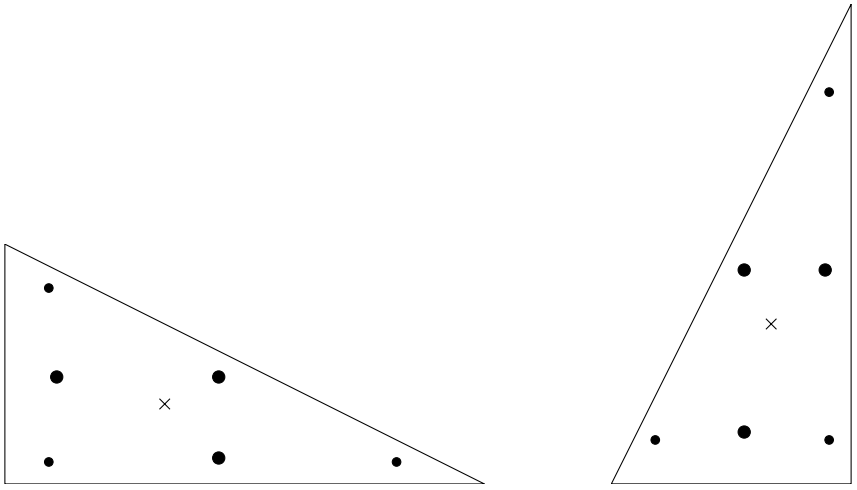

Figure 3.6: Sample points on two rotations of a triangle for a six-point Gaussian quadrature scheme with dot sizes indicative of weighting coefficients. Triangle centroids indicated for reference.

To perform the numerical evaluation of an integral, quadrature rules are applied as

$$\int_T f(\mathbf{r})\, dS = A \sum_{i=1}^{N} w_i f(L_1, L_2, L_3), \tag{3.22}$$

with A as the area of the triangular domain T, N the total number of sampling points of the quadrature rule and w_i the weighting coefficient associated with the i^{th} sampling point. A larger selection of the Gaussian quadrature formulas for triangles, as reported in [22], is available in Table 4.2.

Quadrature rules, such as the ones presented here, are formulated to integrate polynomial functions exactly, with the number of sampling points increasing as higher-order polynomials are considered. Although an increase in the number of sampling points used will enhance the accuracy of the simulation, it is important to consider the direct influence of this increase on the computational cost of setting up the MoM impedance matrix. The majority of the evaluated integrals needed for the MoM impedance matrix of this study employ three-point Gaussian quadrature for the outer testing integral, and seven-point Gaussian quadrature for the inner source-integral.

Particular interest now falls on the numerical integration of the free-space Green's function as is performed when evaluating Equations 3.17 and 3.18. For convenience, the free-space Green's function is repeated here,

$$G(\mathbf{r}, \mathbf{r}') = \frac{e^{-jk|\mathbf{r}-\mathbf{r}'|}}{4\pi|\mathbf{r}-\mathbf{r}'|}. \tag{3.23}$$

When the source point $\mathbf{r}'$ and the observation point $\mathbf{r}$ coincide, the free-space Green's function is singular. As illustrated in Section 3.1.5, the use of non-overlapping quadrature rules for the source and testing integrals avoids the singularity, but is not adequate if an accurate solution is required. Singularity cancellation quadrature rules, that are specially developed to deal with singular and near-singular integrals, are necessary if the accuracy is to be increased. These rules are explored in Section 4.3.

3.3 Conclusions

This chapter introduced the EFIE-based MoM, as presented in [4]. First-order RWG basis functions were used for the current discretisation and EFIE testing procedures. Non-overlapping quadrature was investigated as an alternative to the rigorous analytical approach of handling singularities, as used in [4]. Although this proved to be fairly accurate, this study opted for the use of singularity cancellation quadrature, which was found to produce results of sufficient accuracy.

Chapter 4

Numerical Integration

The numerical evaluation of integrals is a central theme in computational methods, and the field of CEM is no exception. Numerical integration procedures, often referred to as *quadrature*, involve approximating integrals by weighted summations of integrand samples.

This chapter explores some of the ideas behind one- and two-dimensional quadrature schemes. The relevance of each scheme to particular applications within a MoM implementation is noted, and discussions within the thesis frequently refer to sections of this chapter.

4.1 One-dimensional quadrature

Integration over a single variable offers a suitable starting point for considering numerical approximations. The integrals utilised in MoM solvers are primarily surface integrals in two dimensions, but one-dimensional quadrature rules are perhaps more intuitive and are thus introduced here. Definite integrals of the form

$$I = \int_a^b f(x)\,dx \tag{4.1}$$

are considered, and quadrature rules constructed for such cases are briefly reviewed in this section.

4.1.1 The rectangle method

The rectangle rule is perhaps the simplest one-dimensional quadrature rule. Suppose a known function $f(x)$ can be sampled at any point in the interval $[a, b]$, and the integral of the function over this range is to be evaluated. The rectangle rule approximates the integral as the area of a rectangle with a width equal to the length of the integration interval and height equal to a function sample taken within the interval. The rectangle method is a composite integration method constructed from the rectangle rule. By dividing the integration interval into N subintervals, the integral may be approximated as the sum of

the areas of N rectangles with the widths of the subintervals, and heights determined by sampling the function at some point within each of the subintervals. With this approach, the integration is numerically approximated as

$$\int_a^b f(x)\,dx \approx h\sum_{i=1}^{N} f(x_i), \tag{4.2}$$

with $h = (b-a)/N$ and $x_i = a + (i - \frac{1}{2})h$. If Equation 4.2 is evaluated in the limit with $N \to \infty$, then the approximation indeed becomes an equality. In the formulation of Equation 4.2, x_i is a mid-point sample within the i^{th} interval.

Many variations of this concept exist, including the trapezoidal rule and Newton-Cotes quadrature formulas. More accurate quadrature rules are however available for cases where functions samples can be taken at non-uniformly spaced points. When the function $f(x)$ is explicitly given, as is the case in CEM applications, Gaussian quadrature is preferred.

4.1.2 Gaussian quadrature

Gaussian quadrature involves an integral estimate of the form

$$\int_a^b f(x)\,dx \approx \sum_{i=1}^{N} w_i f(x_i), \tag{4.3}$$

that is optimised both for the weights w_i and the abscissas x_i. These parameters are selected so that the estimate is exact for polynomials up to degree p, and the derivation involves the computation of a related Legendre polynomial [2]. Table 4.1 reports the Gaussian quadrature rules from one to seven points. The abscissas x_i^* are defined on the interval $[-1, 1]$, with symmetry imposed on their positions and weights. A transformation to the interval $[a, b]$ can be achieved as

$$\begin{aligned} x_i &= \frac{b-a}{2}x_i^* + \frac{a+b}{2}, \\ w_i &= \frac{b-a}{2}w_i^*. \end{aligned} \tag{4.4}$$

One-dimensional quadrature rules are not typically found in MoM applications as the quantities of interest are usually dependent on two-dimensional fields. An example where one-dimensional quadrature might be used is the calculation of the total surface current, crossing a particular line on the surface of the structure.

4.2 Two-dimensional quadrature

Surface integrals are carried out over two variables. A straightforward approach to constructing a two-dimensional quadrature rule is nesting two one-dimensional quadrature

Table 4.1: Gaussian quadrature rules of order p with weights w_i^* and abscissas x_i^*.

p	N	w_i^*	x_i^*
1	1	2.0	0.0
3	2	1.0	±0.5773502691896257
5	3	0.8888888888888889	0.0
		0.5555555555555556	±0.7745966692414834
7	4	0.6521451548625461	±0.3399810435848563
		0.3478548451374538	±0.8611363115940526
9	5	0.5688888888888889	0.0
		0.4786286704993665	±0.5384693101056831
		0.2369268850561891	±0.9061798459386640
11	6	0.3607615730481386	±0.6612093864662645
		0.4679139345726910	±0.2386191860831969
		0.1713244923791704	±0.9324695142031521
13	7	0.4179591836734694	0.0
		0.3818300505051189	±0.4058451513773972
		0.2797053914892766	±0.7415311855993945
		0.1294849661688697	±0.9491079123427585

rules. The domain of integration should however be carefully considered when doing this. A square integration domain can be approached with ease, whereas a rectangular domain might justify using a different amount of quadrature points for the two dimensions. When considering triangular domains, where the integration variables are dependent on one another, the nesting approach is found to be far from optimal. Since integrals of the form

$$I = \int_T f(x, y)\, dxdy, \tag{4.5}$$

with T a triangular domain, are frequently evaluated in the MoM, integration schemes for these cases are explored in this section.

4.2.1 Composite methods

Integrals are often approximated by summing the contributions of approximations over sub-domains. In fact, the *rectangle method*, discussed in Section 4.1.1, is merely a summation of approximations done with the *rectangle rule*. The same can be said for the trapezoidal method. Newton-Cotes quadrature formulas are also often applied to smaller subintervals of the integration domain to construct a composite method.

A similar approach could be taken for the construction of two-dimensional triangular integration rules. For a surface integral on a triangle, the equivalent to a midpoint

rectangle rule is a centre-point approximation, given as

$$\int_T f(x,y)\,dS = Af(x_c,y_c), \tag{4.6}$$

where A is the area and (x_c, y_c) is the centroid of triangle T. Uniform triangular refinement of a factor $\alpha \in \mathbb{N}$ allows the construction of a composite centre-point integration rule as:

$$\int_T f(x,y)\,dS \approx \sum_{i=1}^{\alpha^2} A_i f(x_{ci},y_{ci}), \tag{4.7}$$

where A_i is the area and (x_{ci}, y_{ci}) the centroid of the i^{th} sub-triangle. Figure 4.1 shows the four-point and sixteen-point composite centre-point integration rules generated with a factor two and factor four refinement respectively. The sub-domains and the weighting coefficients (which are the areas of the sub-domains) are also indicated.

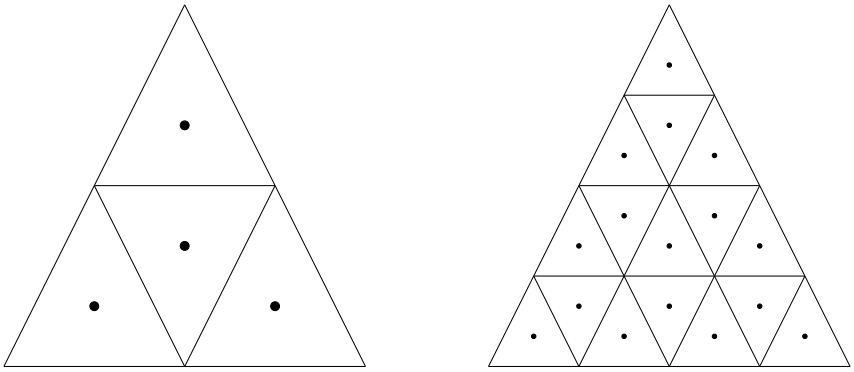

Figure 4.1: Sample points and integration sub-domains for a four-point and sixteen-point composite centre-point quadrature scheme with dot sizes indicative of weighting coefficients.

Composite centre-point quadrature allows for the construction of an integration rule consisting of many integration points. The desired integration accuracy can be achieved by choosing the required amount of integration points. This is especially useful when integrating over fields that are not represented by polynomial functions. In this study, composite centre-point quadrature rules are used for integrals of the absolute value of the difference of two fields.

In the next section, quadrature rules developed for polynomial fields on triangular domains are discussed.

4.2.2 Gaussian quadrature for triangular domains

With similar reasoning as that outlined in Section 4.1.2, Gaussian quadrature rules are developed for surface integrals of polynomial functions on triangular domains. The integration approximation concerned takes the form

$$\int_T f(x,y)\,dS \approx A\sum_{i=1}^{N} w_i f(x_i,y_i). \tag{4.8}$$

Cartesian coordinates were used in Equation 4.8 for consistency, but it is convenient to switch over to simplex coordinates now. For a full discussion of simplex coordinates, refer to Section 5.2. It is however noted here that a point (x, y) in a plane can be found from its simplex coordinates (L_1, L_2, L_3) as

$$\begin{aligned} x &= L_1 x_1 + L_2 x_2 + L_3 x_3 \\ y &= L_1 y_1 + L_2 y_2 + L_3 y_3, \end{aligned} \tag{4.9}$$

where (x_n, y_n) is the coordinates of the n^{th} vertex of the triangle containing the point (x, y). Gaussian quadrature rules are developed by imposing triangular symmetry with regards to the sample points and weights [22]. The sampling points are commonly chosen in sets of three, where all the points in the set share a weighting coefficient, and symmetry is kept by a cyclical definition of the simplex coordinates as (α, β, β), (β, α, β) and (β, β, α). The triangle centroid is another point available for quadrature construction.

The development of a three-point quadrature rule for quadratic functions is offered as an illustration. A general quadratic function on a triangular domain may be expressed as

$$f(L_1, L_2) = a + bL_1 + cL_2 + dL_1L_2 + eL_1^2 + fL_2^2, \tag{4.10}$$

with (L_1, L_2) a linearly independent subset of the set of simplex coordinates (L_1, L_2, L_3). The terms of Equation 4.10 imply that a quadrature rule able to integrate a quadratic function exactly, has to be able to integrate four distinct types of quadratic elements exactly [22]. The exact values of the four integrals are found as

$$\begin{aligned} \int_T dS &= A \\ \int_T L_1 \, dS &= \frac{A}{3} \\ \int_T L_1 L_2 \, dS &= \frac{A}{12} \\ \int_T L_1^2 \, dS &= \frac{A}{6}, \end{aligned} \tag{4.11}$$

with A the area of triangle T. From Equation 4.11, a system of four non-linear equations may be constructed, from which three sample points may be extracted [2] as

$$w = \tfrac{1}{3} \qquad (L_1, L_2, L_3) = \left(\tfrac{2}{3}, \tfrac{1}{6}, \tfrac{1}{6}\right), \tag{4.12}$$

with the cyclical rotation of the coordinates employed to find all three sample points. Similar orthogonal interpolation polynomials to those used for the one-dimensional Gaussian quadrature rules are not available for triangular domains, and the rules in [22] were calculated by iterative techniques solving the set of non-linear equations.

Table 4.2 reports the Gaussian quadrature rules for triangles from one to sixteen points. Note that for $p > 5$, the last set of points reported define six testing points as opposed to just three.

Table 4.2: Gaussian quadrature rules of order p with weights w_i for triangular domains.

p	N	w_i	L_{1i}	L_{2i}	L_{3i}
1	1	1.0000000000000	0.3333333333333	0.3333333333333	0.3333333333333
2	3	0.3333333333333	0.6666666666667	0.1666666666667	0.1666666666667
3	4	-0.5625000000000	0.3333333333333	0.3333333333333	0.3333333333333
		0.5208333333333	0.6000000000000	0.2000000000000	0.2000000000000
4	6	0.1099517436553	0.8168475729805	0.0915762135098	0.0915762135098
		0.2233815896780	0.1081030181681	0.4459484909160	0.4459484909160
5	7	0.2250000000000	0.3333333333333	0.3333333333333	0.3333333333333
		0.1259391805448	0.7974269853531	0.1012865073235	0.1012865073235
		0.1323941527885	0.0597158717898	0.4701420641051	0.4701420641051
6	12	0.0508449063702	0.8738219710170	0.0630890144915	0.0630890144915
		0.1167862757264	0.5014265096582	0.2492867451709	0.2492867451709
		0.0828510756184	0.6365024991214	0.3103524510338	0.0531450498448
7	13	-0.1495700444677	0.3333333333333	0.3333333333333	0.3333333333333
		0.1756152574332	0.4793080678419	0.2603459660790	0.2603459660790
		0.0533472356088	0.8697397941956	0.0651301029022	0.0651301029022
		0.0771137608903	0.0486903154253	0.3128654960049	0.6384441885698
8	16	0.1443156076778	0.3333333333333	0.3333333333333	0.3333333333333
		0.0950916342673	0.0814148234146	0.4592925882927	0.4592925882927
		0.1032173705347	0.6588613844965	0.1705693077518	0.1705693077518
		0.0324584976232	0.8989055433659	0.0505472283170	0.0505472283170
		0.0272303141744	0.0083947774100	0.2631128296346	0.7284923929554

The sampling points for the three-, six- and sixteen-point quadrature rules are plotted in Figure 4.2. The quadrature weights are indicated by the size of the dots and aids in

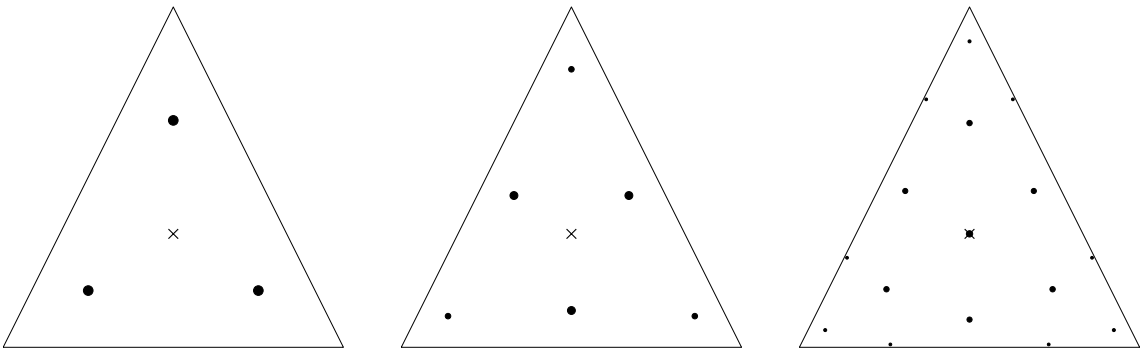

(a) $p = 2$, $N = 3$ (b) $p = 4$, $N = 6$ (a) $p = 8$, $N = 16$

Figure 4.2: Sample points N for three different Gaussian quadrature schemes of order p with dot sizes indicative of weighting coefficients. Triangle centroids indicated for reference.

the visualisation of the symmetry of the quadrature rules.

Gaussian quadrature rules are used in the majority of the evaluated integrals of this study. The MoM matrix elements are calculated with a double integral, where the outer testing-integral employs three-point Gaussian quadrature, and the inner source-integral uses seven-point Gaussian quadrature. The source integral is deemed singular if the testing point falls within, or is closer to the source triangle than $\frac{\dim(T)}{3}$, where $\dim(T)$ is the maximum edge length of T. The integral is then resolved by a singularity cancellation quadrature scheme. If the testing point falls within a triangle adjacent to the source triangle, but is not too close to the source triangle, a 25-point Gaussian quadrature rule is employed for increased accuracy.

4.3 Singularity cancellation quadrature

The full mathematical expressions for the RWG MoM matrix equation elements are listed in Section 3.1.4. This section is concerned with the numerical integration of the free-space Green's function, as is performed when evaluating Equations 3.17 and 3.18. The free-space Green's function is given as

$$G(\mathbf{r}, \mathbf{r}') = \frac{e^{-jk|\mathbf{r}-\mathbf{r}'|}}{4\pi|\mathbf{r}-\mathbf{r}'|}, \tag{4.13}$$

and becomes singular when the source point $\mathbf{r}'$ and the observation point $\mathbf{r}$ coincide. Section 3.1.5 illustrated the use of non-overlapping quadrature rules for the source and testing integrals. In this section, singularity cancellation quadrature, which is a rigorous approach, as opposed to the inherently approximate nature of the non-overlapping approach, will be explored.

Singularity cancellation avoids the overhead of an extraction and analytical integration process, such as discussed in [23], and has the further advantage of being directly applicable to any higher-order basis functions [24]. The application of cancellation quadrature rules involves a geometric transformation of the integration domain such that the Jacobian either cancels or softens the singularity. On the transformed domain, a product rule is constructed using the one-dimensional Gaussian quadrature rules introduced in Section 4.1.2. The integration points and weights are then transformed back to the original triangular domain and can be directly applied to the integrand.

Botha recently presented various transformations for specific near-singular kernels in [24], based on the well known Duffy transformation [25]. In [24], the presented transformations were also rigorously tested, and their performances were compared to those of existing schemes. The Augmented-Duffy-R^1-Constant scheme [24] handled the first-order near singularity quite well, and was shown to be equivalent to a Radial-Angular scheme previously presented in [19]. After investigating some of the available transformation schemes, and taking the guidelines given in [24] into account, the scheme that showed

superior handling of extreme near singularities, the Radial-Angular-R^1-Sqrt scheme [19], was chosen for the development of a singularity cancellation procedure.

4.3.1 Construction of sub-domains

Consider a singular integral of the form

$$I = \int_T \frac{g(\mathbf{r})}{|\mathbf{r} - \mathbf{r}'|}\, dS, \tag{4.14}$$

with $\mathbf{r}'$ falling within, or very near to the triangle T. The position of $\mathbf{r}'$ is used to divide the triangular domain into three sub-domains, each of which would now contain the singularity at one vertex. For the near singular case, the point $\mathbf{r}'$ can be projected onto the plane of T. For each sub-triangle, local x-y coordinates are defined so that the singularity is located at the origin, and the edge opposite to the singularity is parallel to the x-axis. Figure 4.3 shows an example of a triangle appropriately split at a singular point falling within the triangle domain, and also illustrates the local coordinates defined for one of the sub-triangles.

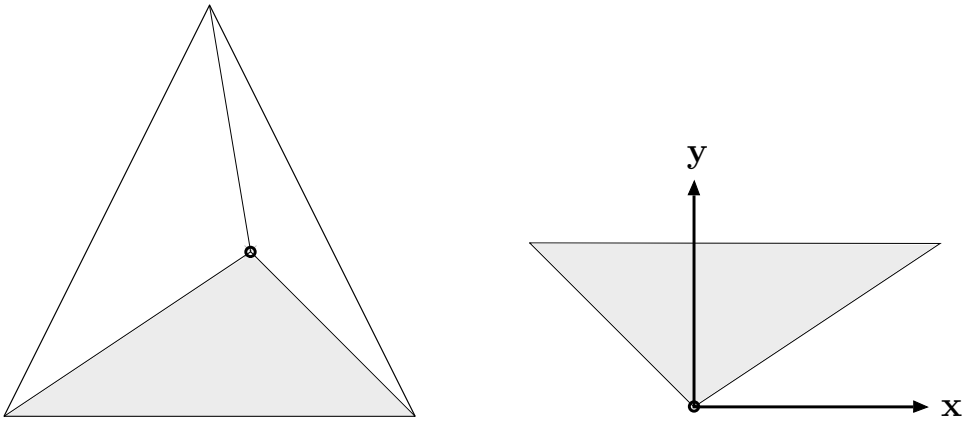

Figure 4.3: Triangular domain divided into three sub-triangles at the location of a singularity. Each sub triangle has local coordinates defined as shown right.

Equation 4.14 can now be evaluated as the sum of three integrals, each constructed on a sub-triangle as

$$I_{sub} = \int_{T_{sub}} \frac{g(x,y)}{\sqrt{x^2 + y^2 + \tilde{z}^2}}\, dxdy, \tag{4.15}$$

where $\tilde{z}$ is the height of the singularity for the near singular case. It should be noted that the point $\mathbf{r}'$ (or a projection thereof onto the plane of T) need not fall within the triangular domain T. For such cases, the procedure is modified such that the final integral is evaluated as the difference between all integrals of sub-triangles having an overlap with the domain of T, and all integrals of sub-triangles that fall entirely outside of the domain of T.

4.3.2 The transformation

The integral of Equation 4.15 undergoes a variable substitution given by [19] as

$$u = \ln\left(\tan\frac{\phi}{2}\right)$$

$$v = \sqrt{R - |\tilde{z}|}$$

$$dxdy = \frac{2R\sqrt{R-|\tilde{z}|}}{\cosh u}\, dudv, \tag{4.16}$$

where ϕ is the angular coordinate variable of a standard cylindrical coordinate representation, and $R = \sqrt{x^2 + y^2 + \tilde{z}^2}$. The substitution of the variables u, v for x, y sees the triangular domain of integration transformed into a quasi-rectangular domain with the singularity now *softened* along one edge. It can also be seen from Equation 4.16 that the transformation introduces an R-term in the Jacobian that affects the singularity cancellation. Figure 4.4 shows the quasi-rectangular integration domain on which a 6×6 Gaussian product rule was constructed, with six points along each of the u, v directions (see Section 4.1.2). Figure 4.4 also shows the integration points transferred back to the triangular domain.

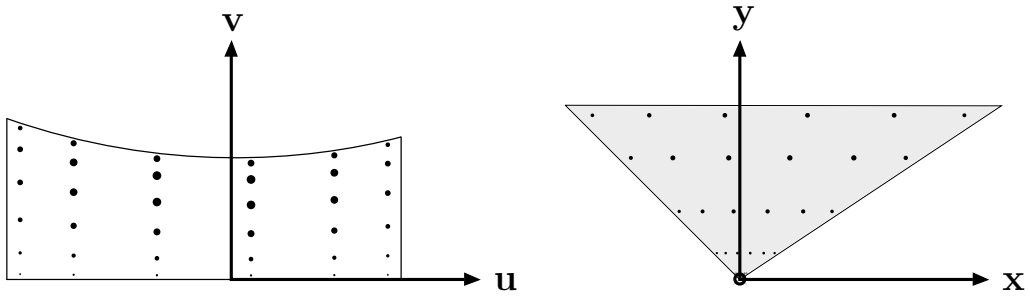

Figure 4.4: Sample points of a 6×6 Gaussian product rule on transformed and original sub-triangle integration domains. Dot sizes indicative of weighting coefficients.

Finally, Figure 4.5 shows the complete $3 \times 6 \times 6$ quadrature rule for the singularity introduced in Figure 4.3. It is important to note that the integral of Equation 4.14 is not evaluated in the transformed domain. The integration is executed in the original domain as shown in Figure 4.5, with the transformed domain only used to determine the weights and locations of the sample points.

4.3.3 Accuracy

To test the accuracy of the presented Radial-Angular-R^1-Sqrt scheme, the integral

$$I = \int_T \frac{1}{\sqrt{x^2 + y^2 + \tilde{z}^2}}\, dS, \tag{4.17}$$

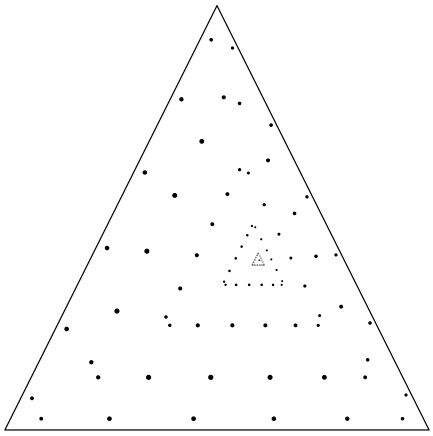

Figure 4.5: Sample points of a $3 \times 6 \times 6$ Radial-Angular-R^1-Sqrt quadrature scheme.

is considered for the near-singular case $\tilde{z} = 0.1 \times \dim(T)$, where $\dim(T)$ is the maximum edge length of triangle T. The triangular domain, and projection of the singular point are the same as depicted in Figure 4.3. The accuracy of the numerical integration will be measured by looking at the normalised error as

$$\text{error} = \left| \frac{I_* - I_{ref}}{I_{ref}} \right|, \tag{4.18}$$

where I_* is the numerical evaluation of the integral and I_{ref} is the reference solution, obtained by a quasi-analytical process. Composite centre-point quadrature, Gaussian quadrature, and the Radial-Angular-R^1-Sqrt schemes are compared in Figure 4.6.

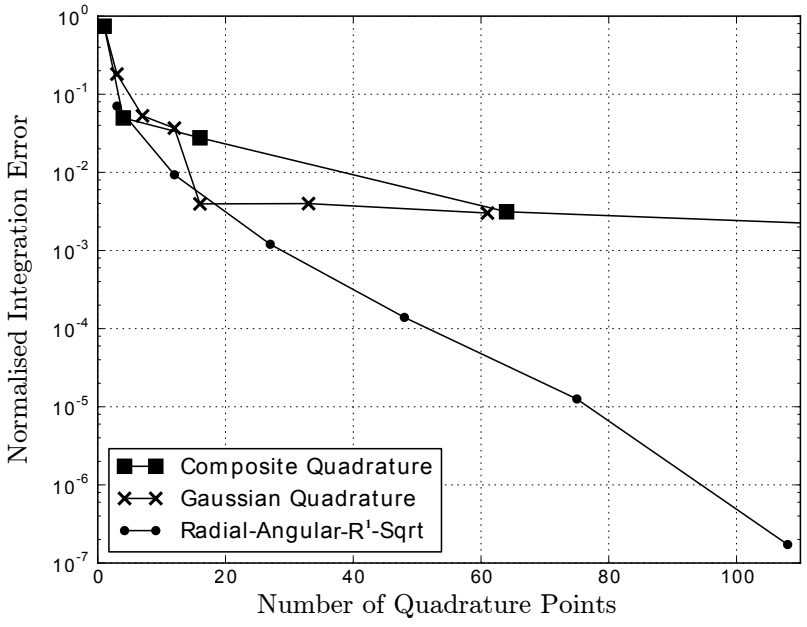

Figure 4.6: Normalised error of three quadrature rules as number of quadrature points increase.

The error in Figure 4.6 is plotted against the number of quadrature points used. It is clear that quadrature schemes that are not geared towards singularities (or near singularities) require a high amount of quadrature points to suppress integration errors. It is also seen in Figure 4.6 that the returns from an increase in quadrature points quickly diminishes. A singularity cancellation scheme is essential if the error is to be driven down significantly, and the Radial-Angular-R^1-Sqrt scheme is seen to be effective.

4.4 Conclusions

The accurate numerical evaluation of surface integrals is crucial to the development of a reliable MoM solver. This chapter discussed one- and two-dimensional quadrature schemes, and illustrated the relevance of each scheme to particular applications within a MoM implementation. An understanding of the differences between the quadrature schemes and extensive knowledge of the MoM formulation proved essential to the development and application of an accurate MoM solver.

Chapter 5

Basis Functions

The discretisation of continuous scalar and vector fields is a central theme in the CEM community and has led to much attention being afforded to the study of basis functions. This chapter provides some of the necessary insights into these basis functions from a MoM perspective.

5.1 One-dimensional scalar basis functions

Before investigating multi-dimensional vector basis functions, it is valuable to first look at some of the simplest one-dimensional scalar basis functions, since the concepts developed here are often extended for multi-dimensional cases. No quantity of the MoM formulation is constructed with one-dimensional basis functions. The polynomial-order of these functions are however easily visualised and provide a suitable introduction to their two-dimensional triangular counterparts, as used in the MoM.

Given a continuous function of one variable $f(x)$, and a domain of interest discretised into i subsections, a functional approximation of the following form is desired

$$f(x) \cong \sum_{i=1}^{N} f(x_i) B_i(x), \tag{5.1}$$

where $B_i(x)$ belongs to a predefined set of basis functions, and $f(x_i)$ is a sample of $f(x)$ taken at the start of the i^{th} interval. Pulse and rooftop basis functions offer piecewise-constant and piecewise-linear approximations respectively. The pulse basis function is defined as

$$p(x_i) = \begin{cases} 1 & x_i < x < x_{i+1} \\ 0 & \text{otherwise,} \end{cases} \tag{5.2}$$

and the rooftop basis function, also known as the triangle basis function, is defined as

$$t(x_i) = \begin{cases} \dfrac{x - x_{i-1}}{x_i - x_{i-1}} & x_{i-1} < x < x_i \\ \dfrac{x_{i+1} - x}{x_{i+1} - x_i} & x_i < x < x_{i+1} \\ 0 & \text{otherwise.} \end{cases} \tag{5.3}$$

The support of the pulse basis function is a single interval, whereas the rooftop basis function has a support falling over two intervals, and will overlap with adjacent basis functions. The two basis functions are illustrated in Figure 5.1.

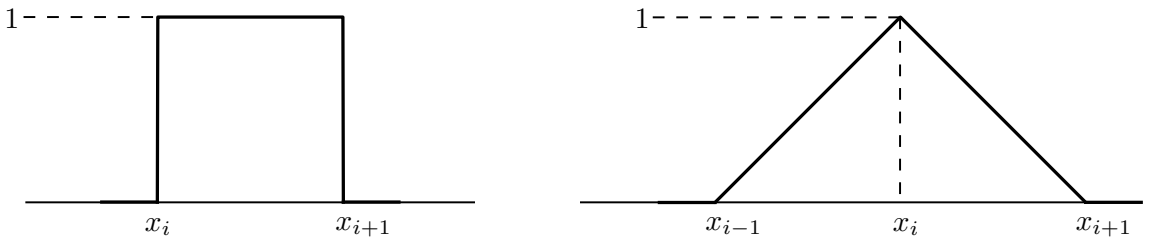

(a) Pulse function $p(x_i)$ (b) Rooftop function $t(x_i)$

Figure 5.1: One-dimensional scalar basis functions.

By utilising either pulse or rooftop basis functions, and the formulation of Equation 5.1, any function can be approximated through interpolation in either a piecewise-constant or a piecewise-linear fashion. This is illustrated in Figure 5.2.

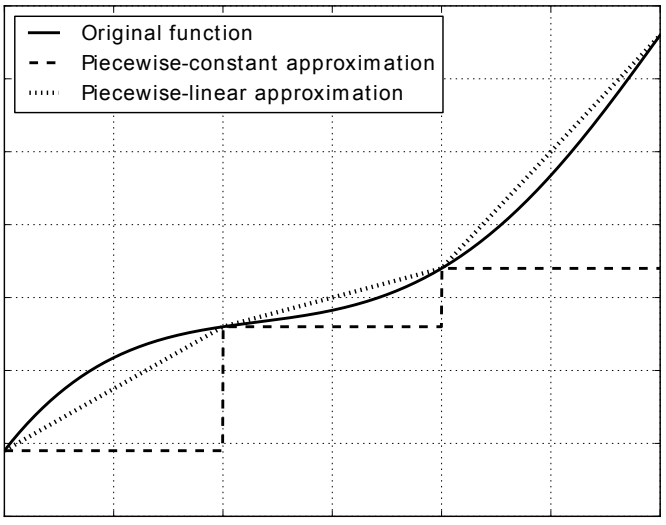

Figure 5.2: Piecewise-constant and piecewise-linear approximations of an arbitrary transcendental function.

5.1.1 Lagrange basis functions

The rooftop basis functions are linear (first-order) Lagrange basis functions, and form part of the larger set of polynomial Lagrange basis functions, which will be presented here up to second-order. The quadratic (second-order) Lagrange functions, shown in Figure 5.3, require a midpoint sample within the interpolation interval, and are defined as

$$\begin{aligned} Q_1(x) &= \tfrac{1}{2}x(x-1) \\ Q_2(x) &= 1-x^2 \\ Q_3(x) &= \tfrac{1}{2}x(x+1). \end{aligned} \tag{5.4}$$

The basis functions are defined on the interval $[-1, 1]$, are vanishing at two of the three interpolation points, and unity at the remaining point. When appropriately shifted, and

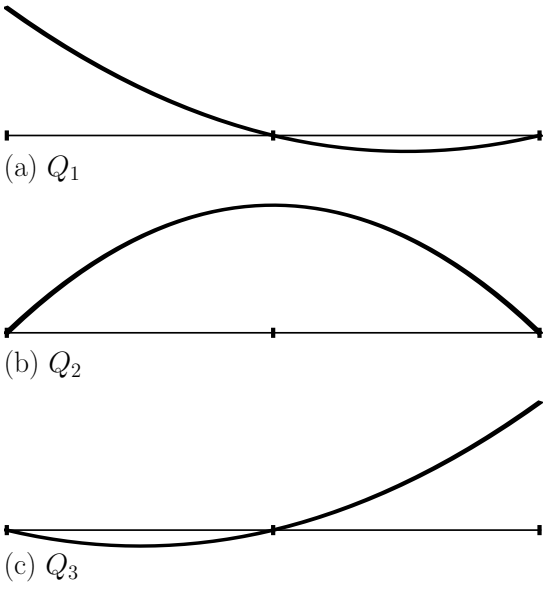

Figure 5.3: Second-order Lagrange functions.

weighted with function samples, the second-order Lagrange functions offer a quadratic approximation to the sampled function over an interval of interest.

5.2 Simplex coordinates for triangular domains

With the MoM being primarily concerned with triangulated models of three-dimensional surfaces, such as shown in Figure 3.5 on page 18, the discussion of two-dimensional basis functions will be restricted to those specifically defined for triangular domains. The definitions and analyses of such functions are facilitated by the use of simplex coordinates.

Simplex coordinates (L_1, L_2, L_3), also known as barycentric coordinates, offer an alternative method of describing the position of a point within a triangle. This discussion

of simplex coordinates will follow a form similar to that given in [2]. A simplex coordinate represents the perpendicular distance from a triangle edge relative to the triangle height, as shown in Figure 5.4. A simplex coordinate of a point, L_n, can also be seen as the ratio

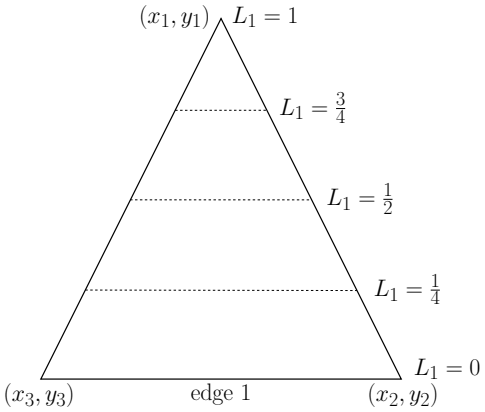

Figure 5.4: Simplex coordinate L_1 defined on a triangular element.

of the area of a triangle, formed by a point and edge n, to the total triangle area. As such, an alternative name local-area coordinates is also in use. From Figure 5.4 it can further be seen that lines of constant L_n are parallel to edge n.

The relationship between the Cartesian coordinates (x, y) of a point, and its simplex coordinates (L_1, L_2, L_3) can be described by the matrix equation

$$\begin{bmatrix} x \\ y \\ 1 \end{bmatrix} = \begin{bmatrix} x_1 & x_2 & x_3 \\ y_1 & y_2 & y_3 \\ 1 & 1 & 1 \end{bmatrix} \begin{bmatrix} L_1 \\ L_2 \\ L_3 \end{bmatrix}, \tag{5.5}$$

where (x_n, y_n) are the coordinates of the n^{th} vertex. The matrix equation also indicates the linear dependence of the simplex coordinates. Inversion of Equation 5.5 yields the formulation of the simplex coordinates as

$$L_n = \frac{1}{2A}(a_n + b_n x + c_n y), \tag{5.6}$$

where A denotes the area of the triangle and

$$\begin{aligned} a_n &= x_{n+1}y_{n+2} - x_{n+2}y_{n+1} \\ b_n &= y_{n+1} - y_{n+2} \\ c_n &= x_{n+2} - x_{n+1}, \end{aligned} \tag{5.7}$$

with the subscripts cycling through the triangle vertices so that $n + 1 = 1$ for $n = 3$. The gradient operator is often applied to quantities that are expressed in terms of simplex coordinates. With the two-dimensional Cartesian form of the gradient operator given as

$$\nabla f = \frac{\partial f}{\partial x}\mathbf{x} + \frac{\partial f}{\partial y}\mathbf{y}, \tag{5.8}$$

the gradient of L_n can be found as

$$\nabla L_n = \frac{1}{2A}(b_n \mathbf{x} + c_n \mathbf{y}). \tag{5.9}$$

5.3 Two-dimensional scalar basis functions

Two-dimensional scalar Lagrange basis functions of up to second-order that relate closely to the one-dimensional Lagrange functions, discussed in Section 5.1.1, are presented in this section. The given functions can be used to form an approximation or discretisation of some desired scalar field over a triangular domain.

5.3.1 Triangular pulse function

The triangular pulse function, shown in Figure 5.5, although not a Lagrangian function, is the simplest scalar basis function and has an order of zero. In terms of simplex coordinates, the pulse function may be given as

$$B_0(L_1, L_2, L_3) = L_1 + L_2 + L_3, \tag{5.10}$$

and takes on a value of unity across the entire triangular domain. Utilising pulse functions to represent a function offers a discontinuous piecewise-constant representation over a triangulated domain.

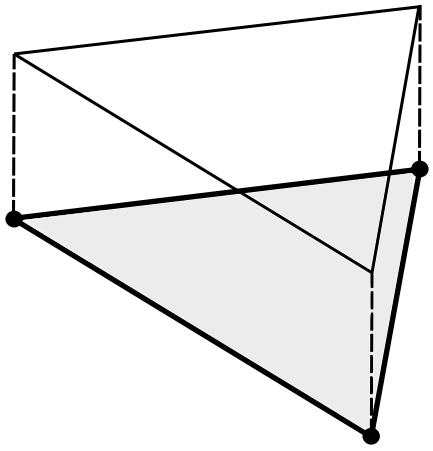

Figure 5.5: Constant basis function B_0.

The surface charge of the RWG MoM, $\tilde{\rho}_s$, is a piecewise-constant field that can be represented by a set of triangular pulse basis functions.

5.3.2 First-order Lagrange functions

The simplest Lagrange functions are first-order functions that were developed to interpolate between function values at the vertices of a triangular domain. The basis function associated with vertex n is given by the simplex coordinate of that same vertex, and thus has the representation

$$B_n(L_1, L_2, L_3) = L_n, \tag{5.11}$$

with B_1 illustrated in Figure 5.6.

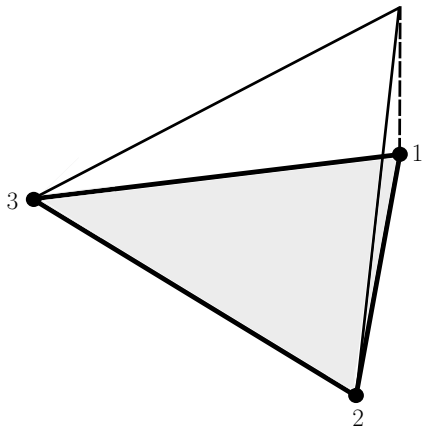

Figure 5.6: Linear Lagrange basis function B_1.

Since the sample taken at the local vertex, $n = 1$ in Figure 5.6, is common to all elements of the triangulated surface that share the particular node, it is possible to give linear basis functions with a nodal definition rather than a triangular definition. Such an approach results in pyramid basis functions, centred at each node of the mesh, as shown in Figure 5.7.

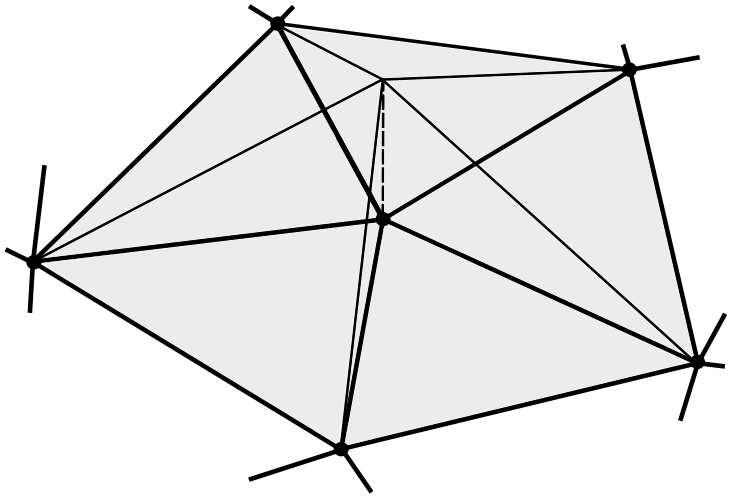

Figure 5.7: Linear pyramid basis function.

Pyramid functions have unity amplitude at one node and vanishes at all other nodes of the mesh, and are the two-dimensional equivalent of rooftop functions. The elements that make up the support of a pyramid function are not required to be coplanar. Pyramid functions, i.e. first-order Lagrange functions, offer a continuous piecewise-linear representation over a triangulated domain.

Nodal averaging and the Zienkiewicz-Zhu patch-recovery procedure, as introduced in Section 2, are employed in this study to recover improved charge values at mesh nodes. First-order Lagrange functions are then used to construct the final recovered charge distribution.

5.3.3 Second-order Lagrange functions

The second-order Lagrange function requires three additional samples on the triangular area in order to achieve an exact representation of any quadratic function. The six functions are closely related to the one-dimensional quadratic Lagrange functions given in Equation 5.4, and are depicted in Figure 5.8

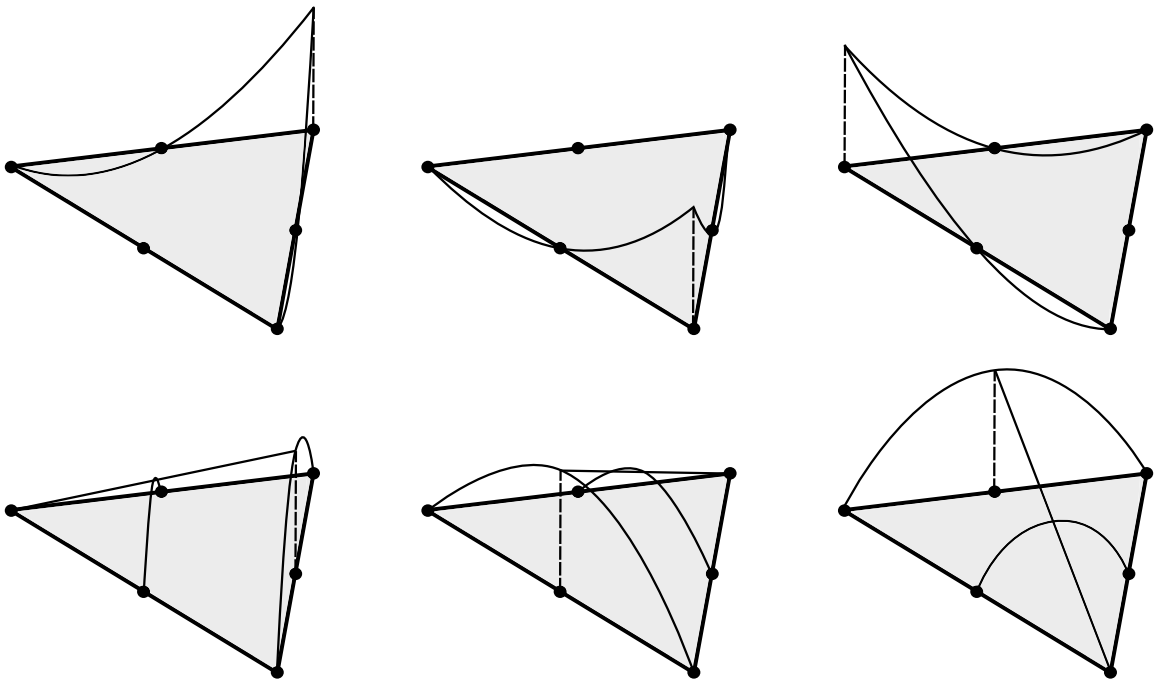

Figure 5.8: Quadratic Lagrange basis functions B_{ijk}.

These basis functions can be expressed in terms of simplex coordinates as

$$\begin{aligned} B_{200}(L_1, L_2, L_3) &= L_1(2L_1 - 1) \\ B_{020}(L_1, L_2, L_3) &= L_2(2L_2 - 1) \\ B_{002}(L_1, L_2, L_3) &= L_3(2L_3 - 1) \\ B_{110}(L_1, L_2, L_3) &= 4L_1L_2 \\ B_{011}(L_1, L_2, L_3) &= 4L_2L_3 \\ B_{101}(L_1, L_2, L_3) &= 4L_1L_3. \end{aligned} \tag{5.12}$$

Each quadratic function has a value of unity at one of the six nodes (three vertex nodes and three nodes at the edge midpoints) and vanishes at the remaining five nodes, as seen in Figure 5.8. Using quadratic Lagrange functions to represent a function in a triangulated domain would result in a continuous piecewise-quadratic representation of the function.

5.4 Vector basis functions

Although scalar basis functions are of some relevance to this study, the primary field quantities of the MoM are vector fields. A fundamental step in the formulation of the MoM, as investigated in Chapter 3, involves obtaining a mathematical expression for the discretised current distribution $\mathbf{J}$ on an arbitrary PEC surface. Suitable vector basis functions $\mathbf{B}_n(L_1, L_2, L_3)$ are required with which the surface current may be approximated as

$$\mathbf{J} \cong \sum_{n=1}^{N} I_n \mathbf{B}_n(L_1, L_2, L_3), \tag{5.13}$$

where I_n belongs to the set of N coefficients required for the discretisation.

The MoM calculates induced surface currents from the electric field relations described by the EFIE. As seen in Section 3.1.1, the surface divergence of the unknown current density is present in the integrodifferential formulation. From this, it is clear that the expansion functions $\mathbf{B}_n(L_1, L_2, L_3)$, used in Equation 5.13, need to ensure a finite divergence across triangle boundaries. Such a set of divergence-conforming functions will thus maintain normal continuity between mesh cells.

Analogous to the curl-conforming FEM vector elements, the divergence-conforming vector functions used in the MoM, can be presented as having two orders, with the solenoidal and divergent orders given separately [26]. Hierarchical vector basis functions up to mixed second-order are investigated in this section. These functions include solenoidal vector functions up to first-order, and divergent vector functions up to second-order. The inexact Helmholtz decomposition is employed with

$$\begin{aligned} \nabla_s \cdot \mathbf{S}_n &= 0 \\ \nabla_s \times \mathbf{D}_n &\approx 0, \end{aligned} \tag{5.14}$$

where **S** are solenoidal functions and **D** are divergent functions.

5.4.1 Divergence-conforming first-order basis functions

In terms of Cartesian coordinates, a general two-dimensional linear vector basis function in the x-y plane may be given as

$$\mathbf{B}(x,y) = (a + bx + cy)\mathbf{x} + (d + ex + fy)\mathbf{y}. \tag{5.15}$$

Such a representation clearly illustrates the six degrees of freedom inherent in a linear vector function expansion. Controlling the normal component of the function at the edges, as required for the construction of a divergence-conforming function, requires fixing two degrees of freedom per edge, and leaves no further degrees of freedom for specifying the tangential component. For divergence-conforming functions, discontinuities in the tangential component are however acceptable. $\mathbf{B}(x,y)$ can be constrained to have a normal component of unity over one edge, and a vanishing normal component at the remaining two edges. A set of three such functions on a triangular domain, as shown in Figure 5.9,

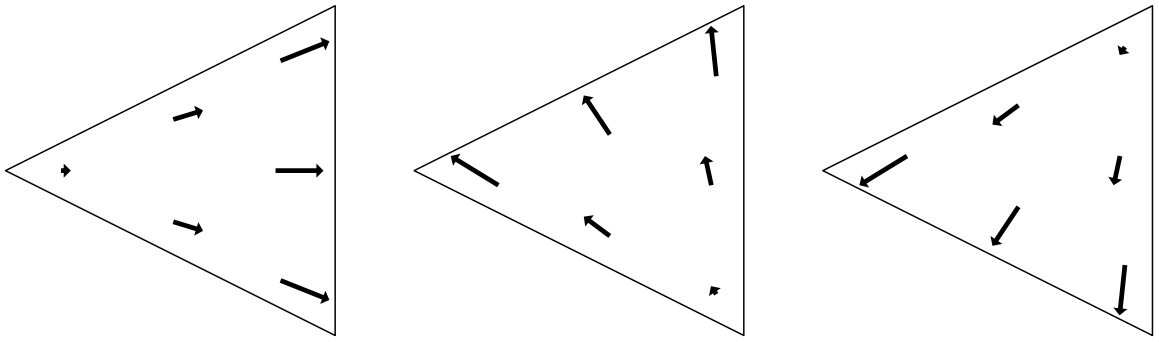

Figure 5.9: Linear divergence-conforming vector basis functions.

enables the representation of a linear vector field with its normal component across all the triangle edges specified. A simplex coordinate representation of each of these basis functions can be found as

$$\mathbf{D}_{1,n}(L_1, L_2, L_3) = l_n \, \mathbf{u}_T \times (L_{n+2}\nabla L_{n+1} - L_{n+1}\nabla L_{n+2}), \tag{5.16}$$

where l_n is the length of the n^{th} edge, and $\mathbf{u}_T$ is the unit vector normal to the surface of triangle T [2]. The formulation presented is a rotation of the curl-conforming basis function of the same order [2, 27]. General divergence-conforming functions can be found from their curl-conforming counterparts as

$$(\mathbf{D}_n)_{\text{div}} = \mathbf{u}_T \times (\mathbf{D}_n)_{\text{curl}}. \tag{5.17}$$

Normal continuity on a global mesh is ensured by having a shared coefficient for triangles that share an edge. A sign change must however be enforced in one of the triangles. Figure 5.10 shows such an edge based basis function with its two-triangle support.

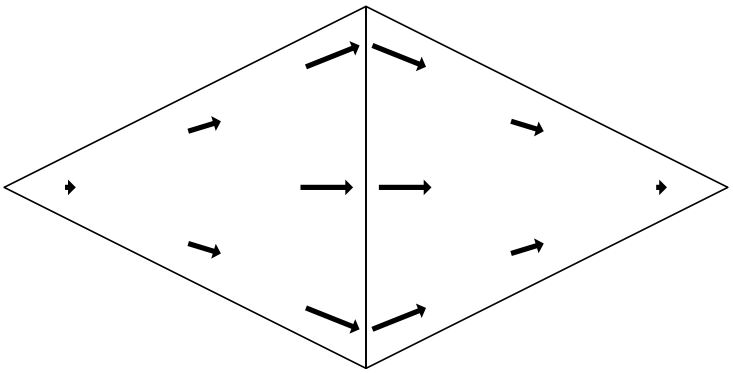

Figure 5.10: Edge based linear divergence-conforming vector basis function.

These basis functions are identical to the Rao-Wilton-Glisson basis functions [4], given in Equation 3.9 and discussed in Section 3.1.2. Linear divergence-conforming basis functions are mixed first-order functions, containing a zero-order solenoidal component along with a first-order divergent component. The zero-order solenoidal component is investigated in the following Subsection.

5.4.2 Solenoidal zero-order basis functions

A constant solenoidal vector function can be derived as a rotated gradient of a first-order scalar function [26]. The first-order Lagrange scalar functions, presented in Section 5.3.2, will be employed for this purpose. These solenoidal functions are still divergence-conforming, and the required normal continuity across elements is upheld by having a common coefficient associated with all triangles sharing a particular vertex node. The pyramid form of the linear Lagrange function, shown in Section 5.3.2, is thus used. Figure 5.11 shows a zero-order solenoidal function on a six triangle support. Note that the triangles are not required to be coplanar. A simplex coordinate representation can be found within each triangle as

$$\mathbf{S}_{0,n}(L_1, L_2, L_3) = \mathbf{u}_T \times \nabla L_n, \tag{5.18}$$

where $\mathbf{u}_T$ is the unit vector normal to the surface of triangle T.

Zero-order solenoidal functions are not usually required in a MoM implementation, but can be utilised in an inexact Helmholtz decomposition of the RWG basis functions of the MoM. This decomposition, given in Equation 5.14, is performed within this study.

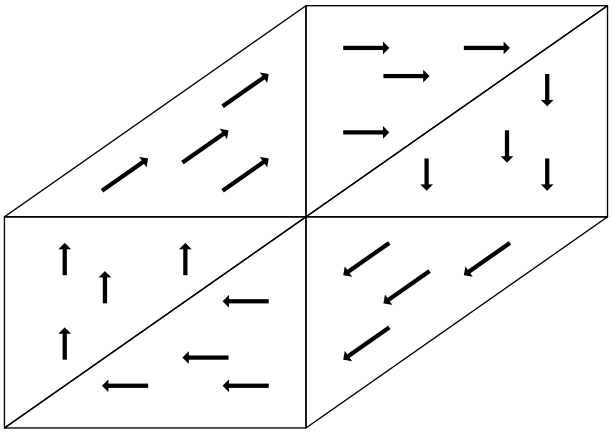

Figure 5.11: Nodal representation of a zero-order solenoidal function.

5.4.3 Solenoidal first-order basis functions

A full first-order vector function representation requires the addition of three more edge functions to the mixed first-order divergence-conforming RWG elements [26]. Rotated gradients of a second-order Lagrange scalar functions, as introduced in Section 5.3.3, can be used for this purpose. The last three functions of Equation 5.12 are quadratic on a single edge only, and from these functions, the following first-order solenoidal edge vector representation is derived

$$\begin{aligned}\mathbf{S}_{1,n}(L_1, L_2, L_3) &= \mathbf{u}_T \times \nabla(L_{n+1}L_{n+2}) \\ &= \mathbf{u}_T \times (L_{n+2}\nabla L_{n+1} + L_{n+1}\nabla L_{n+2}).\end{aligned} \tag{5.19}$$

In a familiar approach, the coefficient associated with an edge is forced equal for the two triangles sharing that edge, in order to ensure normal continuity across the edge. Figure 5.12 shows the first-order solenoidal basis function on its two triangle support.

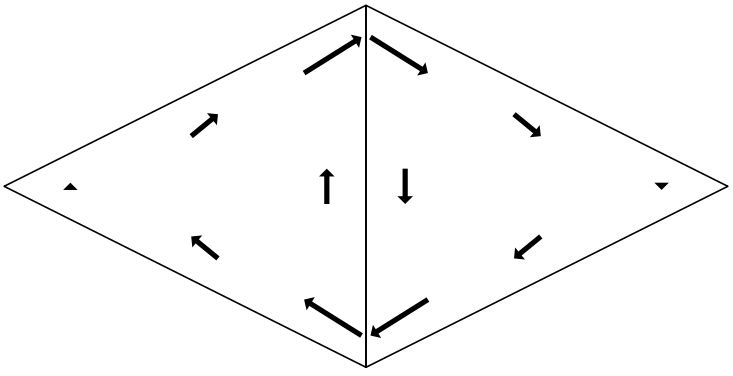

Figure 5.12: Edge based linear solenoidal vector basis function.

In this study, the solenoidal current component contained within an RWG MoM solution is improved with the use of first-order solenoidal basis functions.

5.4.4 Divergent second-order basis functions

The addition of two quadratic divergent face functions are required in order to move up to a mixed second-order vector representation [26]. These two functions are also available from work done within a curl-conforming context [2, 27] and are calculated from the rotational second-order functions given in [26] as follows

$$\begin{aligned}\mathbf{D}_{20}(L_1, L_2, L_3) &= \mathbf{u}_T \times (L_2 L_3 \nabla L_1 + L_1 L_3 \nabla L_2 - 2L_1 L_2 \nabla L_3) \\ \mathbf{D}_{21}(L_1, L_2, L_3) &= \mathbf{u}_T \times (L_2 L_3 \nabla L_1 - 2L_1 L_3 \nabla L_2 + L_1 L_2 \nabla L_3).\end{aligned} \tag{5.20}$$

Figure 5.13 shows the two quadratic divergent functions. These functions are constrained to a single triangle and have a zero normal component to all three the triangle edges.

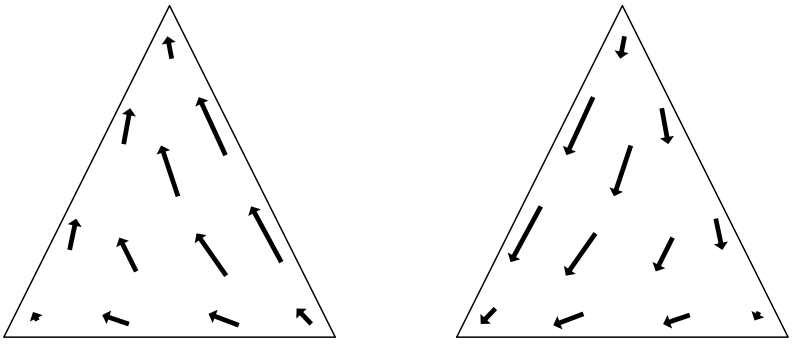

Figure 5.13: Quadratic divergent vector basis functions.

A recovered charge is used in this study to determine coefficients for a set of divergent second-order basis functions in order to improve the accuracy of an RWG MoM solution.

5.5 Tree-cotree decomposition

The collection of functions presented in Section 5.4 are not all compliant with the inexact Helmholtz decomposition of Equation 5.14. The first-order divergence-conforming functions, i.e. the RWG elements, contain within them a solenoidal component of order zero, while also having non-zero divergence. Since the divergent and solenoidal current components are handled separately in this study, it is desirable to decompose the RWG elements into its divergent and solenoidal components.

Loop-star basis functions [27] have been developed to address this problem within the RWG based MoM. With this approach, RWG basis functions are grouped together to form loop functions and star functions across the mesh, with loop functions forming the solenoidal functions, and star functions forming the divergent functions. The use of tree-cotree decomposition, as given in [28, 29, 30], is however equivalent and offers a very structured approach to achieve the inexact Helmholtz decomposition.

Tree-cotree decomposition has its origins in graph theory. Within a connected graph G, a tree is a connected sub-graph that forms no closed loops. A spanning tree of G is a tree graph that connects all the vertices of G. A triangulated surface, as constructed during the MoM surface discretisation, seen as a connected graph and an associated tree graph can be found. Figure 5.14 shows a spanning tree on a mesh of a rectangular plate. The starting node of the tree can be arbitrarily chosen. Note that all the nodes of the

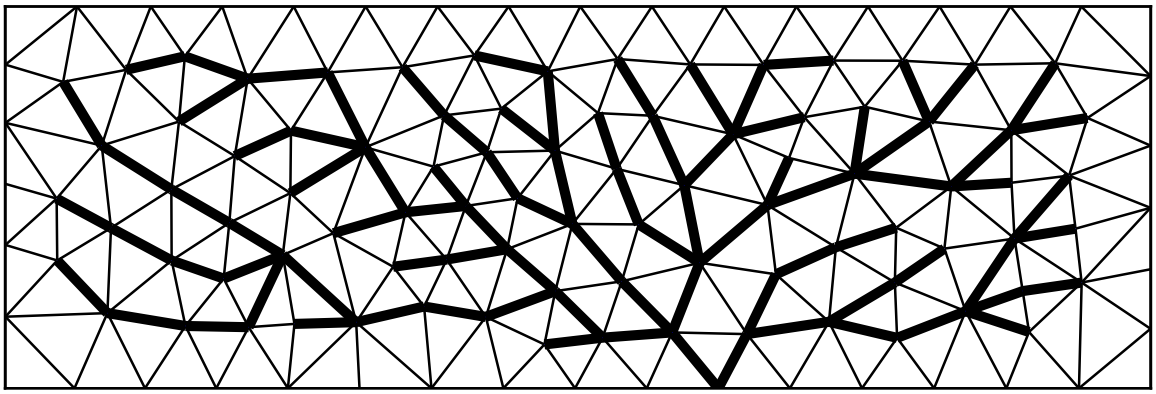

Figure 5.14: Spanning tree on a triangulated rectangular patch.

mesh that form part of the domain boundary are regarded as being a single node during the construction of the tree. The reason for this grouping will become apparent shortly.

After finding a suitable tree graph, the edge-based RWG elements that fall on the tree edges are replaced by the zero-order pure solenoidal functions of Section 5.4.2. RWG functions are still defined on the cotree edges, i.e. the interior edges that do not form part of the tree graph. At this stage, it is clear that boundary edges could not form part of either the tree or the cotree as the functions defined on tree and cotree edges describe a current flow across their edges. The domain boundary is thus regarded as a single tree node. It is convenient to visualise the zero-order solenoidal function that is associated with the tree node that forms the domain boundary. This nodal function has the same simplex coordinate structure as the other zero-order solenoidal functions, namely

$$\mathbf{S}_{0,boundary}(L_1, L_2, L_3) = \mathbf{u}_T \times \nabla L_{boundary}, \tag{5.21}$$

with $L_{boundary}$ the barycentric function of all nodes that fall on the domain boundary. Such a function forms a constant vector loop around the outside of the domain, as shown in Figure 5.15. Structures containing additional domain boundaries would yield similar results at these boundaries.

It should be noted that the tree graph of a graph containing N nodes will have $N-1$ edges [29]. Since the functions removed from the original RWG function space were associated with the tree edges, and the solenoidal functions that are to be added are associated with the tree nodes, one extra solenoidal function exists. This problem is

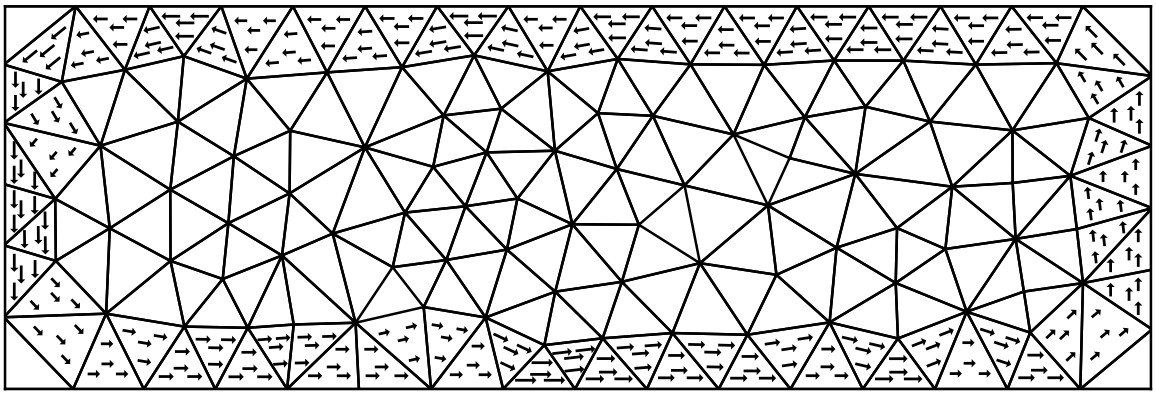

Figure 5.15: Zero-order solenoidal function associated with the domain boundary of a rectangular patch.

solved by not associating a solenoidal function with the base node of the tree graph, leaving exactly N free nodes for the construction of the zero-order solenoidal space.

When considering current approximations that may be constructed with the various vector basis functions of this section, it is important to note the equivalence of the tree-cotree function space to the first-order divergence-conforming function space. By using terminology from set theory, this equivalence is expressed as

$$\{\mathbf{D}_{1,n}; n \in E\} \equiv \{\mathbf{D}_{1,n}; n \in E_{\text{cotree}}\} \oplus \{\mathbf{S}_{0,i}; i \in V_{\text{tree}}\}, \tag{5.22}$$

where E is the set of all internal edges decomposed into E_{tree} and E_{cotree}, V_{tree} is the set of all free vertices, and $\oplus$ indicates the direct sum of the function spaces.

5.6 Conclusions

This chapter discussed one- and two-dimensional scalar and vector basis functions, as needed for the description and construction of quantities related to the MoM.

The higher-order divergence-conforming vector functions are of particular interest within this study, as MoM recovery procedures are developed for function spaces constructed with these functions.

Chapter 6

Recovery of a MoM Charge

The first step in the development of a recovery based local error estimator for the MoM is the design and implementation of a charge recovery procedure. The ideas of nodal averaging and the Zienkiewicz-Zhu patch-recovery procedure posed for FEM formulations form the starting point, with parallels between the FEM and MoM processes drawn.

An article detailing the development of a newly proposed recovery method, and reporting the findings contained in this chapter, has been accepted for publication [31].

6.1 The MoM charge

Consider an RWG-based MoM solution obtained on a triangulated surface, as discussed in Section 3.2. The discretised surface current that approximates the true surface current $\mathbf{J}$ is then represented by

$$\mathbf{J} \cong \sum_{n=1}^{N} I_n \mathbf{f}_n, \tag{6.1}$$

where $\mathbf{f}_n$ is the RWG basis function defined at the n^{th} edge, and I_n represents its coefficient. The RWG basis functions are first-order divergence-conforming basis functions, as discussed in Section 5.4.1 and introduced as per the original RWG paper [4], in Section 3.1.2.

The charge associated with the MoM solution is calculated as

$$\tilde{\rho_s} = -\frac{1}{j\omega} \sum_{n=1}^{N} I_n \nabla_s \cdot \mathbf{f}_n, \tag{6.2}$$

with $\omega = 2\pi f$ the angular frequency. The basis functions for the charge are zero-order scalar functions, or triangular pulse doublets as described in Section 5.3.1. The total surface charge distribution will thus have a discontinuous, piecewise-constant form. If the true surface charge ρ_s were known, the error in the charge could be expressed as

$$e_\rho = \rho_s - \tilde{\rho_s}. \tag{6.3}$$

The objective of a recovery procedure is to produce an improved charge representation $\tilde{\rho}_s^*$, using higher-order triangular scalar functions such as discussed in Section 5.3.2, by post-processing the charge $\tilde{\rho}_s$ of Equation 6.2. The error in the charge could then be approximated by substituting the recovered charge $\tilde{\rho}_s^*$ for the true charge ρ_s in Equation 6.3.

As an example, consider a $1.5\lambda \times 0.5\lambda$ perfect electrical conducting (PEC) plate with an appropriate triangular discretisation in the order of $h = \frac{\lambda}{10}$. The mesh elements and piecewise-constant charge distribution $\tilde{\rho}_s$ of the MoM solution is shown in Figure 6.1.

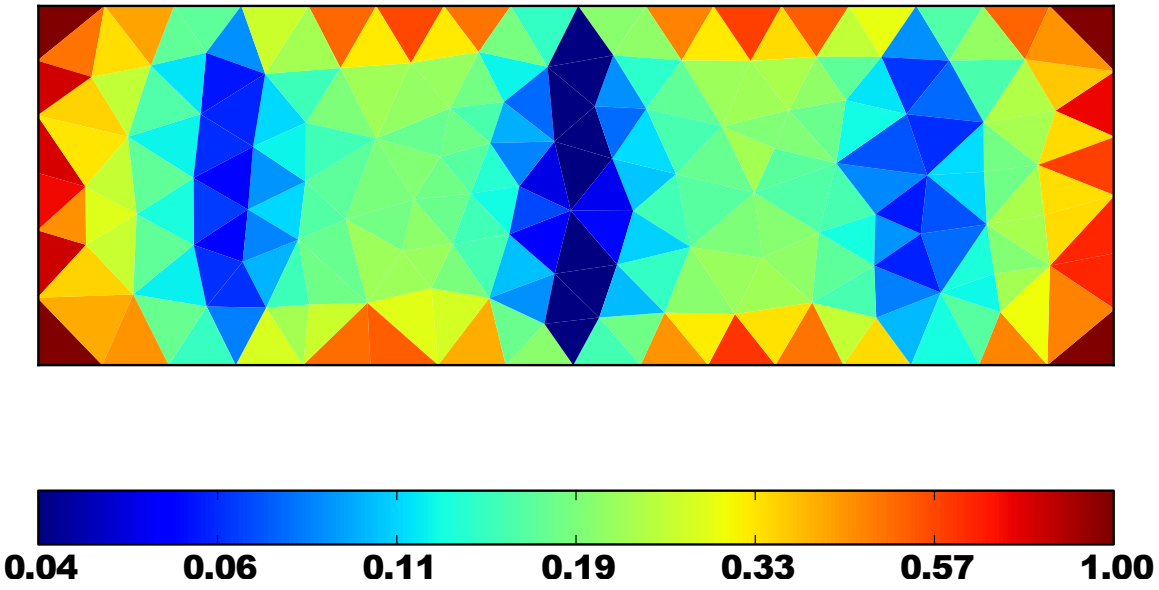

Figure 6.1: Piecewise-constant charge magnitude of a first-order MoM solution on a rectangular PEC plate (log scale).

As a reference charge solution, the numerical charge associated with a MoM solution obtained on a factor-four h-refined version of the original mesh is used. The refinement is uniform and divides each triangular element into sixteen congruent sub-triangles, as shown in Figure 6.2.

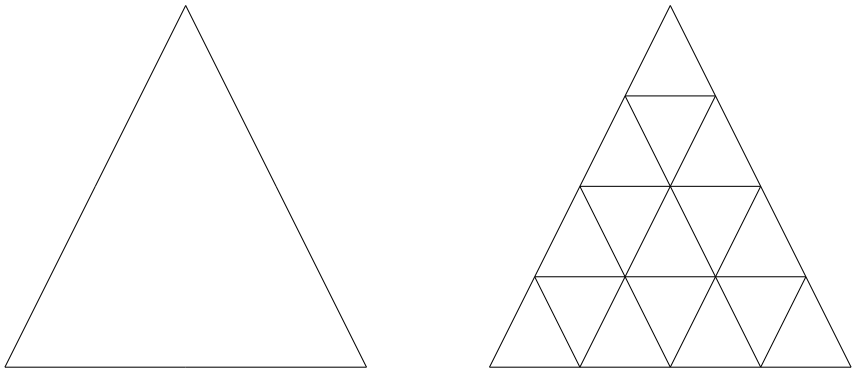

Figure 6.2: Factor-four uniform h-refinement of a triangle.

The reference charge distribution is given in Figure 6.3. Although this reference charge distribution also has a discontinuous piecewise-constant form, it is presented as a contour. The charge values at the triangle centroids, being the points furthest away from any discontinuities, are deemed to be the most accurate and stable points and used for this visualisation.

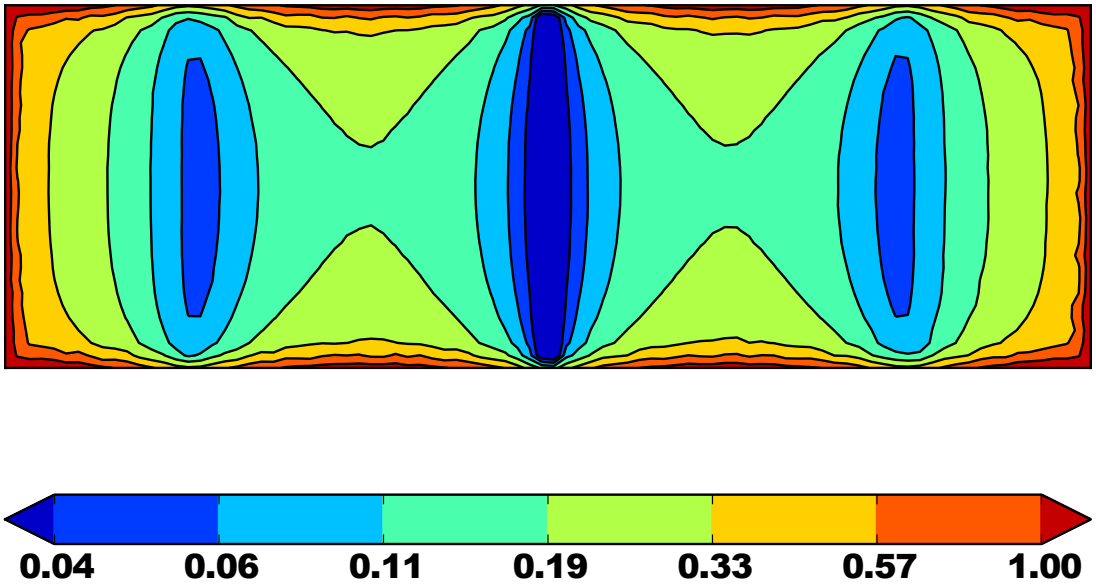

Figure 6.3: Reference charge magnitude distribution obtained on a factor-four h-refined version of the original mesh of a rectangular PEC plate (log scale).

In the sections to follow, the recovery procedures are evaluated by calculating a point-wise charge difference between the recovered charge and the reference solution. This difference is calculated at the triangle centroids of the refined mesh, where the reference solution is most accurate.

In the following section, a *nodal averaging* charge recovery procedure will be developed and evaluated for this example plate.

6.2 Averaging

The zero-order numerical charge $\tilde{\rho}_s$, shown in Figure 6.1, is to be recovered to a first-order improved version. The recovered charge $\tilde{\rho}_s^*$ will thus be piecewise linear on the triangular sub-domains. Since nodal averaging recovers charge values at the mesh vertices, the recovery will also be continuous.

Consider a local patch, formed by the union of all the elements sharing a particular vertex node, such as is shown in Figure 6.4. To recover the charge for the k^{th} node, the average of the surrounding elements is taken, i.e.

$$\rho_k = \frac{\sum_{i=1}^{N} \rho_i}{N} \tag{6.4}$$

with N the number of elements surrounding node k. The locally numbered charge values ρ_i are the constant values of $\tilde{\rho}_s$, sampled on the elements that meet at vertex k.

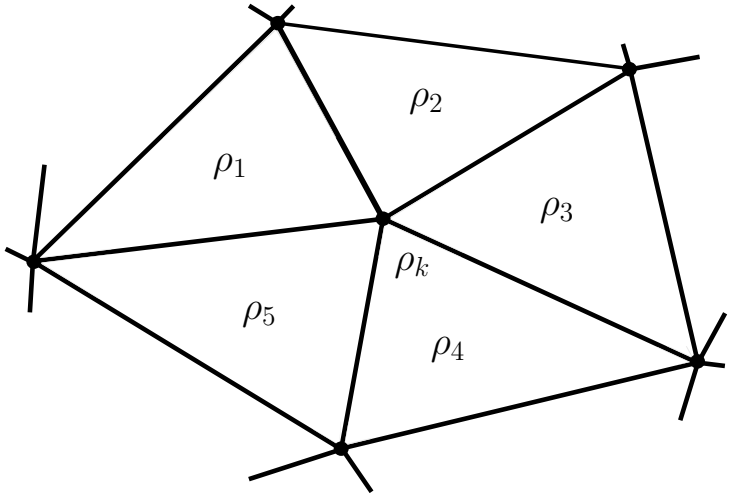

Figure 6.4: Local patch formed by the union of all elements around vertex node k.

6.2.1 Results

The piecewise-linear continuous recovered charge distribution, obtained by nodal averaging, is shown in Figure 6.5 on the same log scale as the reference charge distribution. At

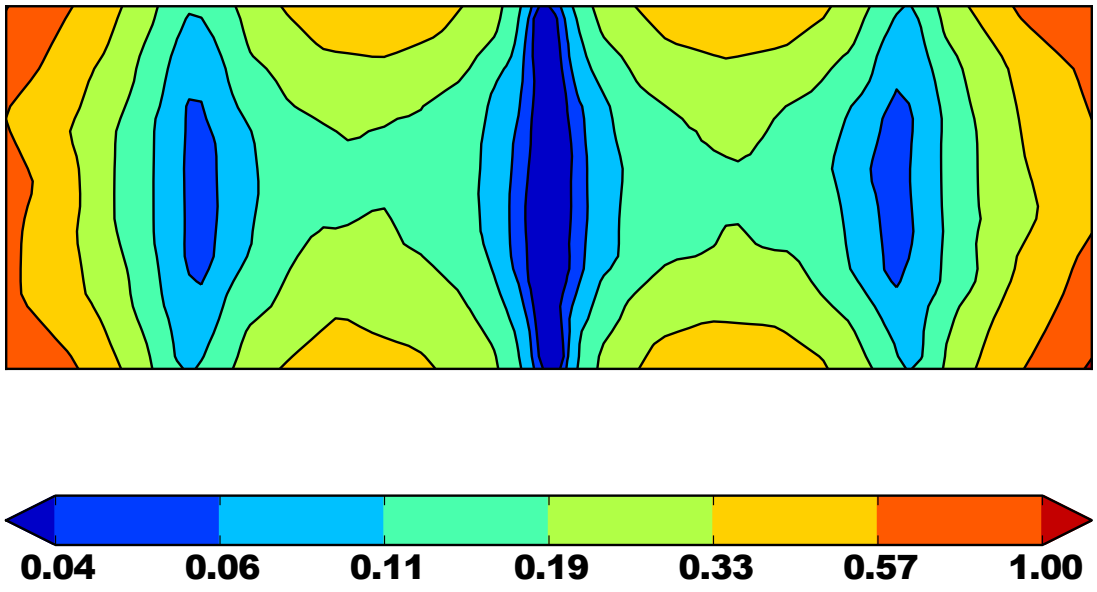

Figure 6.5: Recovered charge magnitude distribution obtained with nodal averaging (log scale).

first glance, it may seem that nodal averaging produces a reasonable charge recovery as it is visually pleasing. This does however not guarantee that averaging would provide

an improvement of the charge distribution. This recovery procedure can be viewed as a low-pass filter acting on the piecewise-constant charge $\tilde{\rho}_s$. The detail of the variation in the charge density is diminished, and the high values of the charge density at the domain boundary are degraded.

Figure 6.6 shows the absolute value of a point-wise difference between the reference solution and the solution recovered with nodal averaging on a log scale. This difference plot displays the shortcomings of averaging at outer elements where high values persist deep into the inner domain of the plate.

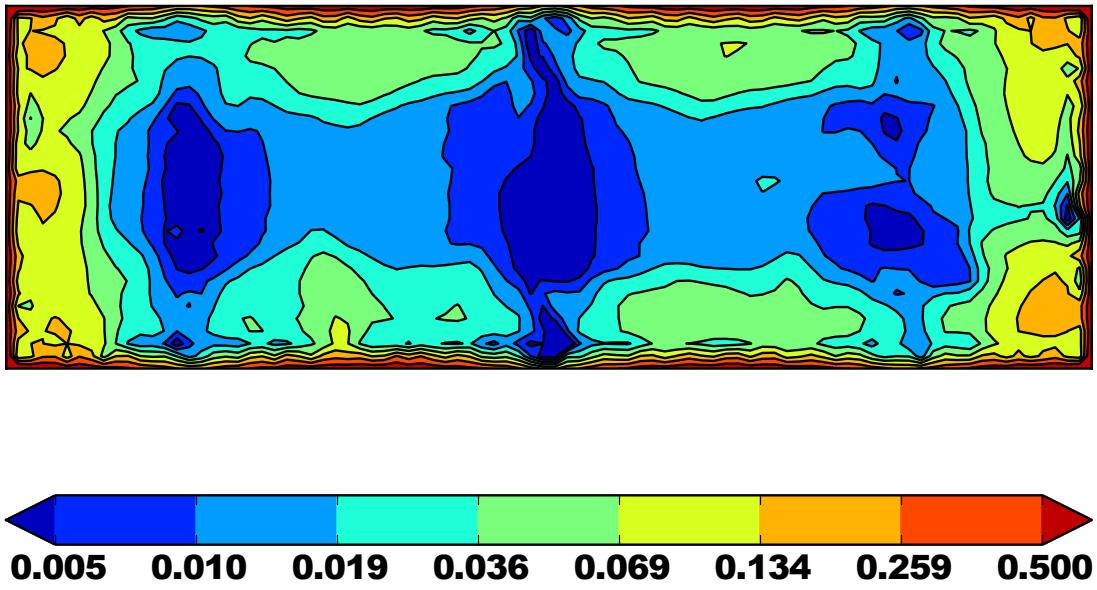

Figure 6.6: Difference between reference charge magnitude and nodal averaging recovered charge magnitude (log scale).

6.2.2 Conclusions

Nodal averaging enforces inter-element continuity, even though numerical charge distributions associated with higher-order MoM solutions do not. Although this might not immediately appear to be a drawback, it should be noted that this constraint effectively limits the recovery function space for no good reason other than convenience. The enforced continuity furthermore degrades the performance of averaging on meshes that have surface junctions.

It would appear that nodal averaging could only be effectively applied to a limited amount of problems, and would best be used as a visual tool only. As far as providing an improved version of the surface charge distribution, averaging proves to be inadequate.

6.3 Zienkiewicz-Zhu patch recovery

In a similar manner to nodal averaging, the ZZ-recovery procedure also recovers charge values at the mesh vertices, and the piecewise-linear recovered charge will also be continuous. The procedure is applied to the same local patch formed by the union of the elements connected to a particular node, as shown in Figure 6.4.

The method involves a least-squares fit of a linear function in the plane of the local patch to the charge values sampled at the centroids of the elements. The recovered value is then a sample of the linear function at the location of the shared node. With the linear function given as

$$\mathbf{P} = [1, x, y], \tag{6.5}$$

and coefficients

$$\mathbf{a} = [a_1, a_2, a_3]^T, \tag{6.6}$$

to be determined, the least-squares fit can be set up by minimising the following expression

$$\sum_{i=1}^{N} (\rho_i - \mathbf{P}(x_i, y_i)\mathbf{a})^2. \tag{6.7}$$

In the above expression, ρ_i is the constant charge value, and (x_i, y_i) the centroid coordinates of triangle i, with reference to the local patch of Figure 6.4. Minimising Equation 6.7 yields the matrix equation

$$\sum_{i=1}^{N} \mathbf{P}^T(x_i, y_i)\mathbf{P}(x_i, y_i)\mathbf{a} = \sum_{i=1}^{N} \mathbf{P}^T(x_i, y_i)\rho_i, \tag{6.8}$$

which may be solved for the coefficients $\mathbf{a}$.

6.3.1 Special considerations

Some mesh geometries require special attention when adapting the ZZ-recovery, that was developed for two-dimensional FEM applications, to the MoM situation considered here.

The first thing to note is that the linear function defined by $\mathbf{Pa}$ can only be constructed if the elements surrounding the common vertex are coplanar. No extensions to general curved surfaces in three-dimensional space are readily available.

Secondly, nodes that fall on the boundary of the structure pose problems, especially where the local patch would only contain one or two elements. For these patches the matrix of Equation 6.8 could be under-determined. Zienkiewicz and Zhu employ an alternative interior patch for these cases [17]. The recovery is then a sample taken at the location of the boundary node that would now fall on the edge of the interior local patch. The authors go even one step further and recommend employing interior patches as a general procedure for boundary nodes [17]. There are however cases where more than one interior patch contains the same boundary node and even cases where there is

no interior patch containing a particular boundary node at all. An example of either case is shown in Figure 6.7. A number of implementations for dealing with boundary nodes

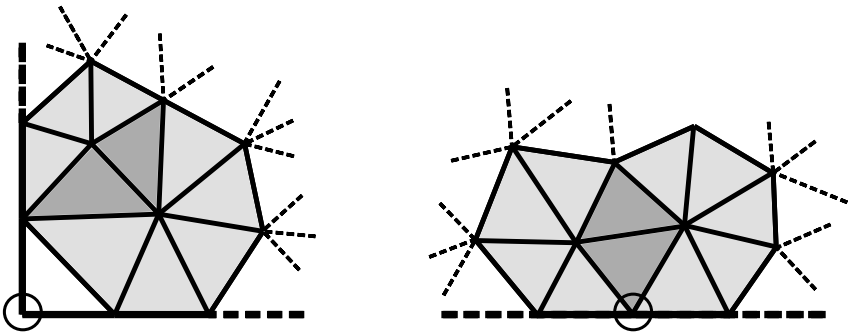

Figure 6.7: A boundary node that does not fall within any interior patch, and a boundary node that falls within two interior patches.

were considered, and the best results were found with the following approach:

1. If the patch constructed around the boundary node contains three or more elements, the ZZ-recovery is applied directly.

2. If the patch formed around the boundary node contains exactly two elements, the interior patch (of which there will be only one) is used to recover the charge for the boundary node.

3. If the patch constructed around the boundary node contains exactly one element, the recovered charge is taken to be the average of the recovered charges at the other two nodes (with 1. and 2. taken into account).

6.3.2 Results

The piecewise-linear continuous charge distribution obtained through ZZ-recovery is shown in Figure 6.8, on the same log scale as the reference charge distribution. The recovery method seems to perform fairly well for internal elements, but appears to degrade near the domain boundary. It also appears as though the total charge on the domain has increased.

Figure 6.9 shows the point-wise difference between the reference solution and the solution obtained by the ZZ-recovery method on a log scale. This difference plot clearly highlights the discrepancies between the reference charge and the ZZ-recovered charge distribution at and near the domain boundary. The nodal-based patches allow for the high charge density on the domain edge to lift internal charge values artificially, and it is only at nodes far removed from the domain boundary where the recovery performs adequately.

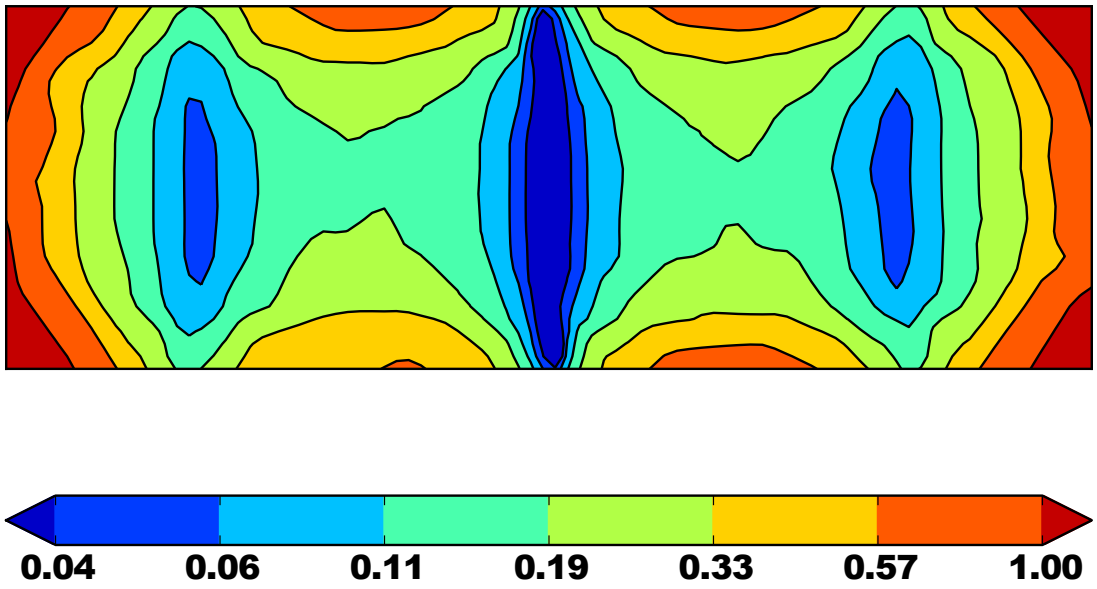

Figure 6.8: Recovered charge magnitude distribution obtained with the ZZ-recovery method (log scale).

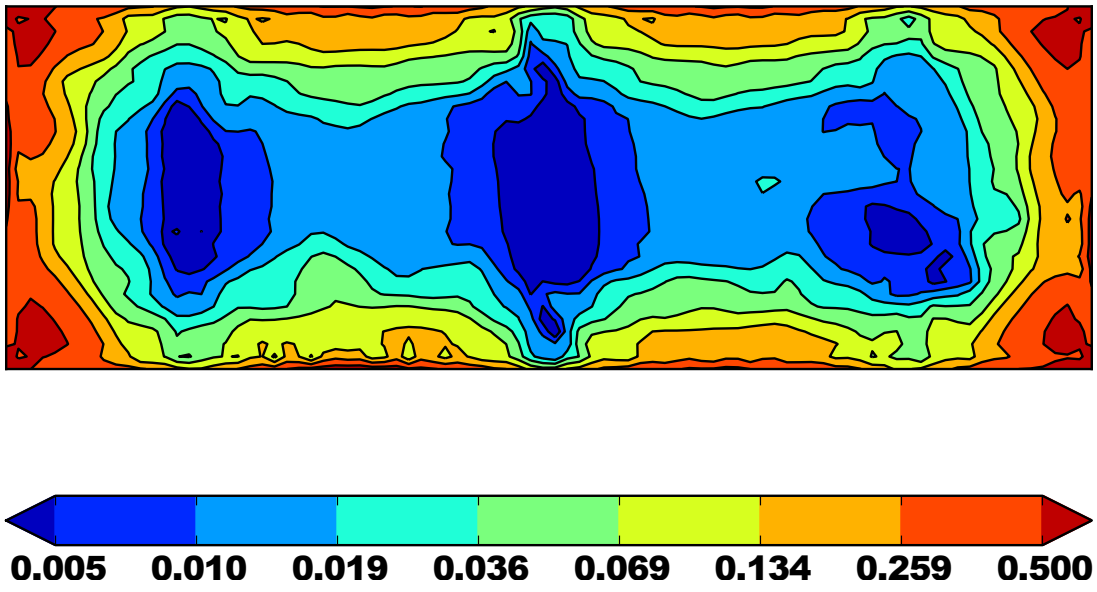

Figure 6.9: Difference between reference charge magnitude and ZZ-recovery charge magnitude (log scale).

6.3.3 Conclusions

ZZ-recovery enforces inter-element continuity, even though numerical charge distributions associated with higher-order MoM solutions do not. The same problems and concerns mentioned with the continuity of the recovery by nodal averaging are thus applicable here, including the limitation of the application to meshes that have surface junctions.

The recovery procedure also does not offer a natural extension to curved surfaces in three dimensions, where the elements surrounding a vertex node would not be co-planar.

Furthermore, a decrease in the inherent accuracy of the ZZ-recovery method can be observed on and near the boundary of the structure, exactly where the charge in the MoM often has high variation.

It would thus appear that a direct application of the ZZ-method in the MoM context is of limited use.

6.4 RWG-based recovery method

In this section, a new charge recovery procedure is introduced that is driven by the particular characteristics of the MoM discretisation. With the ZZ-recovery procedure, data from the elements sharing a vertex node was used as input for the recovery at that node. Using the nodal ZZ-patch in the MoM context is however ill-motivated, since the charge densities on opposite ends of this patch are calculated with various non-overlapping RWG basis functions. As such, the first step in the development of the new recovery process is the consideration of a new local patch.

6.4.1 An RWG-patch

The nodal patch is the support of the first-order Lagrange basis function, as introduced in Section 5.3.2, that is employed in the FEM discretisation. It thus follows that a MoM-specific recovery should be constructed on the elements that form the support of an RWG basis function: two triangles with a common non-boundary edge. The RWG basis functions are the first-order divergence conforming vector functions that were introduced in Section 5.4.1.

In a similar manner to the ZZ-recovery method, a linear model is fit to the charge values obtained from the local patch. The new RWG-patch however only contains two elements. The gradient of the linear model between the two triangle centroids, where the charge density is most accurate, is uniquely determined by the available data. The remaining degree of freedom is represented by the angle of the contour lines of constant charge density. With the only two points of accuracy being the triangle centroids, the choice is made to have the contour lines perpendicular to the line connecting the centroids. Figure 6.10 shows the linear model of the recovery procedure for the triangle pair $T_n^{\pm}$ located at the n^{th} edge. Note that the two centroid charge density values $\tilde{\rho}_s$ of the two triangles used during the recovery process are obtained from the entire MoM solution, and not only the basis function charge densities associated with the common edge.

6.4.2 The recovery procedure

With the newly defined local patches, uniquely recovered charge density values are available along interior mesh edges. These cannot be retained entirely though, as the final

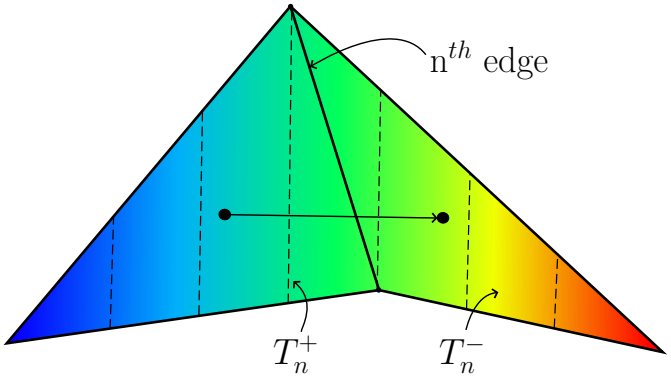

Figure 6.10: Charge density of the RWG-recovery procedure on a local patch.

recovered charge density is set to be linear on each triangular element. It is also noted that continuous interpolation is no longer an option, since the recovery procedure will result in discontinuities at the mesh nodes. This is however not of concern, as the numerical charge associated with a higher-order basis function current representation in the MoM is also discontinuous. To proceed, the recovered values at the midpoints of the edges are retained to form the piecewise linear discontinuous recovery. These values are calculated as

$$\tilde{\rho_n}^* = \tilde{\rho_n}^+ + \frac{\vec{r}_{cc} \cdot \vec{r}_n}{|\vec{r}_{cc}|^2}(\tilde{\rho_n}^- - \tilde{\rho_n}^+), \tag{6.9}$$

where $\tilde{\rho_n}^*$ is the value of the recovered charge $\tilde{\rho_s}^*$ at the centre of the n^{th} edge, and $\tilde{\rho_n}^{\pm}$ is the constant value of $\tilde{\rho_s}$ sampled at the centroid of triangle $T_n^{\pm}$, with reference to Figure 6.11.

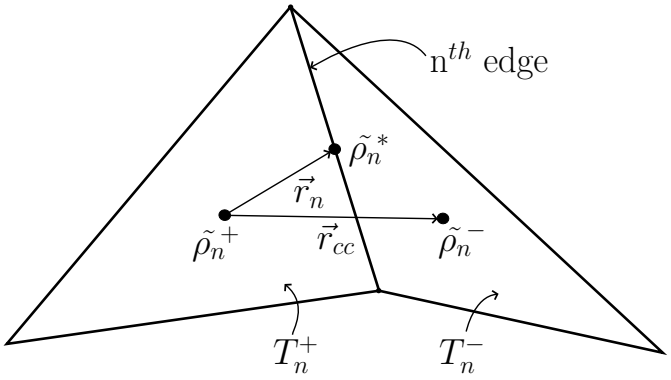

Figure 6.11: Recovery of the charge at the midpoint of the n^{th} edge.

To avoid a loss in the accuracy inherent to the original numerical charge distribution $\tilde{\rho_s}$, and to ensure that the total global value of the recovered charge $\tilde{\rho_s}^*$ is still zero, the recovered charge on each triangle is set to pass through the original charge value at the triangle centroid. A linear plane that is constrained to pass through a particular value at the centroid can be fit to the three recovered values at the midpoints of the edges in a

least squares manner. This is however equivalent to fitting a plane directly to the three recovered values and shifting this plane by a constant value to match the central charge density value. For a proof of the equivalence, see Appendix A.

6.4.3 Special considerations

Some mesh geometries require special attention when implementing the RWG-based recovery method.

The first thing to note is that the linear function used on the local patch of Figure 6.11 to recover the charge at the edge midpoint can only be constructed if the elements of the local patch are coplanar. A general surface in three-dimensional space can be curved, in which case two adjacent elements will not be in the same plane. Before linear recovery is done on the local patch, the two elements are folded out into a single plane.

The second type of elements that require attention are those that fall on the boundary of the structure. These elements will not contain three recovered charge values. The following procedure is followed:

1. If the element contains only one boundary edge, a linear plane is constructed utilising the two recovered values available at the midpoints of the two internal edges along with the original charge density value at the triangle centroid.

2. If the element has two boundary edges, the linear plane associated with the recovery procedure of the internal edge (as shown in Figure 6.10) is taken as the final charge distribution on that element.

A third consideration is that of surface junctions. Where three or more surfaces join, edges exist that are shared by more than two triangles, such as shown in Figure 6.12. For

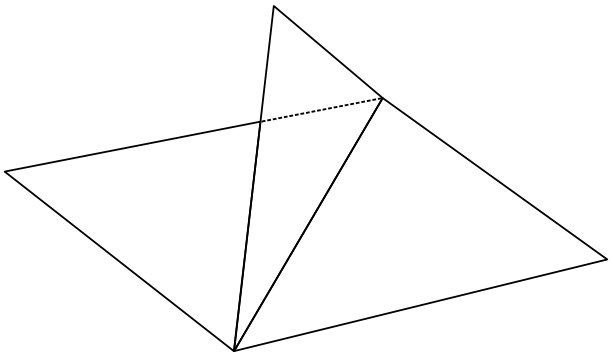

Figure 6.12: A surface junction where three elements meet.

each triangle that meets at the edge, a unique local patch is constructed by collapsing the remaining triangles into a single triangle with the average centroid and a charge density value equal to the summed charge divided by the average area of those triangles. The

triangle that is thus constructed for the local patch formed along with triangle T_n^j has its centroid located at

$$\mathbf{r}_c^* = \frac{\sum_{i=1}^{N} \mathbf{r}_c^i}{N-1}; i \neq j, \tag{6.10}$$

and has a constant charge density of

$$\tilde{\rho} = \frac{\sum_{i=1}^{N} \tilde{\rho}_n^i A_n^i}{\left(\sum_{i=1}^{N} A_n^i\right)/(N-1)}; i \neq j, \tag{6.11}$$

with $\mathbf{r}_c^i$, $\tilde{\rho}_n^i$ and A_n^i the centroid, charge density and area respectively of the i^{th} of N triangles that meet at edge n. It should be noted that each triangle will have a uniquely recovered value associated with the centre point of that edge. The proposed junction formulation has not been tested, due to time constraints.

Lastly, re-entrant corners need to be addressed. Prior to folding the two triangles associated with an edge onto a single plane, the angle between the planes of two elements can be calculated. If it is deemed that a re-entrant corner is modelled, i.e. the two triangles are modelling an edge rather than a smooth surface, no recovery will be made at that edge and the boundary element procedure is directly applied to both triangles.

6.4.4 Results

Figure 6.13 shows the piecewise-linear discontinuous RWG-based recovered charge for the example plate on the same log scale as the reference charge distribution.

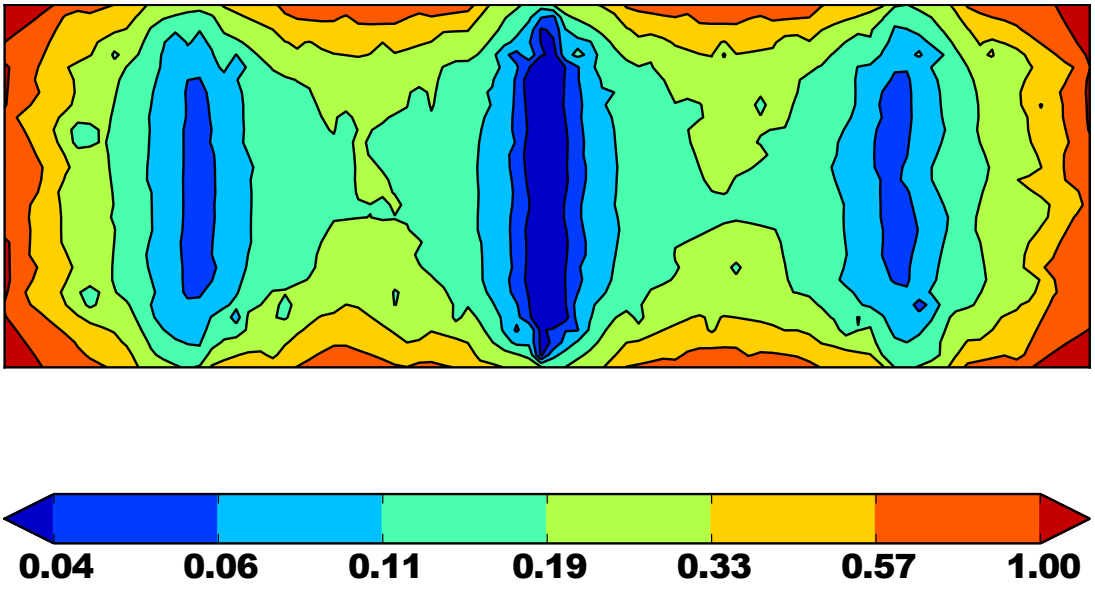

Figure 6.13: Recovered charge magnitude distribution obtained with the RWG-based recovery method (log scale).

The recovery procedure does not result in a visually smooth charge distribution, such as was seen with the previous two methods. This is because charge continuity is not enforced. It can however be seen that the charge distribution follows the trend of the reference solution quite well, with high values achieved at the domain boundary while still maintaining the lower charge density values at internal elements.

Figure 6.14 shows the point-wise difference between the reference solution and the solution obtained by the RWG-based recovery method on a log scale. This difference

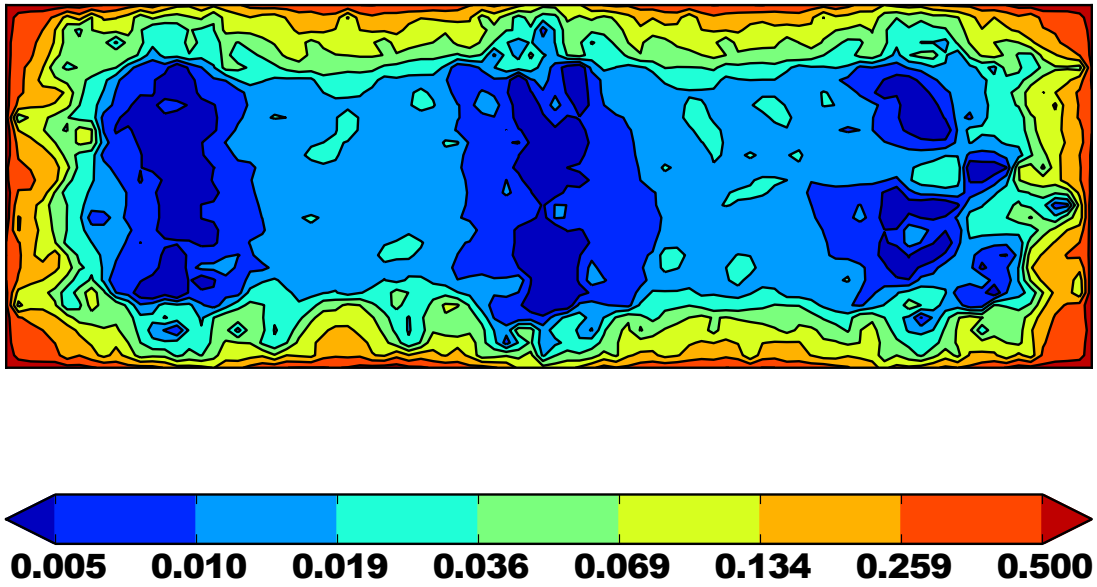

Figure 6.14: Difference between reference charge magnitude and RWG-recovered charge magnitude (log scale).

plot draws attention to the advantages of the RWG-based recovery method. A satisfying extension of the well-matched blue areas up to elements just short of the domain edge can be observed.

6.4.5 Conclusions

The RWG-based recovery procedure introduced here does not enforce inter-element continuity, and as such utilises the available recovery function space entirely. The application of the recovery to curved surfaces and structures containing surface junctions was suggested, and satisfactory performance of the method at the boundary of the structure was illustrated.

A significant benefit to the RWG-based charge recovery procedure is that zero total charge for the solution is maintained. This is not the case with the other considered recovery schemes. It would thus appear that, in this case, the RWG-based recovery procedure produces the best improvement of the charge distribution associated with a MoM solution.

6.5 A posteriori error estimation of the MoM charge

The availability of $\tilde{\rho}_s^*$, an estimate of the true charge ρ_s, enables the constructions of a charge error estimator. An approximation to the true error can be found as

$$e_\rho \approx e_\rho^* = \tilde{\rho}_s^* - \tilde{\rho}_s. \tag{6.12}$$

An element-wise charge error estimator, as well as an estimate of the global error in the charge, can be obtained from Equation 6.12. Define the area-scaled L^1-norm as

$$||\cdot||_{ASL^1(\Omega)} \equiv \frac{\int_\Omega |\cdot| \, dS}{\text{Area}(\Omega)}. \tag{6.13}$$

The element-wise error estimators are then obtained as

$$\eta_\rho^* = ||e_\rho^*||_{ASL^1(T)}, \tag{6.14}$$

on a triangular domain T, and the global charge solution error estimate is found as

$$\bar{\eta}_\rho^* = ||e_\rho^*||_{ASL^1(S)}, \tag{6.15}$$

where S denotes the entire surface of the solution mesh.

6.5.1 Element-wise error estimations

The reference charge distribution of Figure 6.3, that was obtained on a factor-four h-refined version of the original mesh, can be employed to calculate an element-wise reference charge error η_ρ^{ref}, as shown in Figure 6.15.

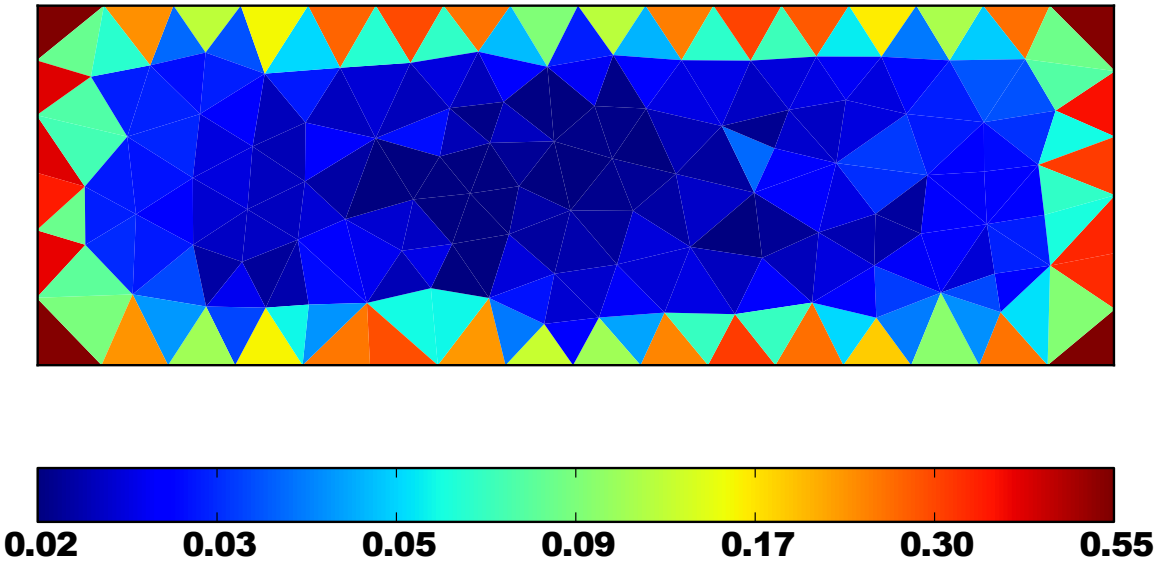

Figure 6.15: Element-wise reference charge error distribution η_ρ^{ref} (log scale).

Now consider the estimated element-wise charge error distributions, as obtained from the various recovery procedures, shown in Figure 6.16. It can be observed that the averaging and ZZ-based methods incorrectly identify elements close to the domain boundary

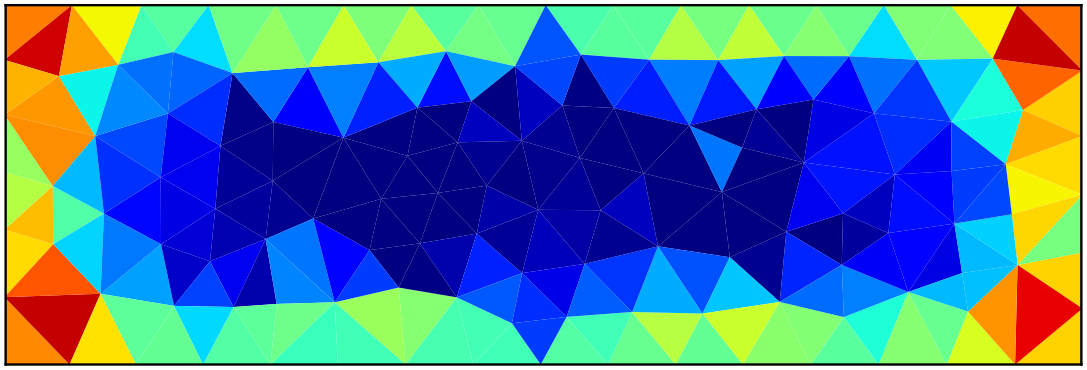

(a) Zienkiewicz-Zhu

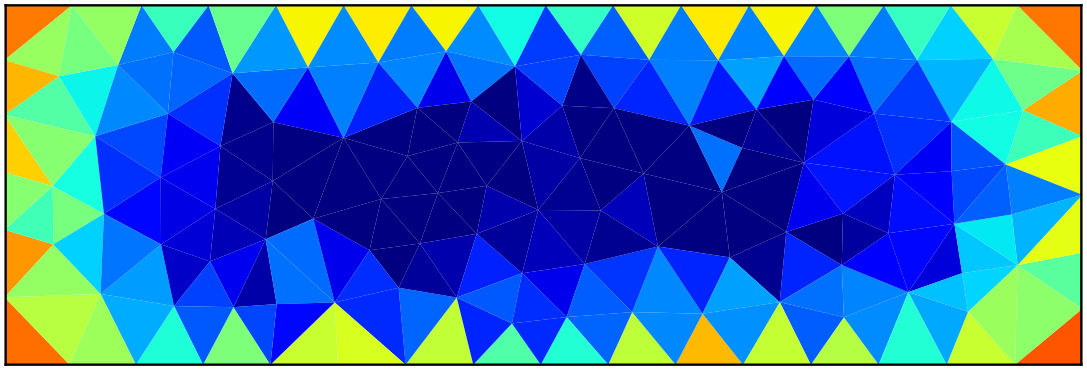

(b) Nodal Averaging

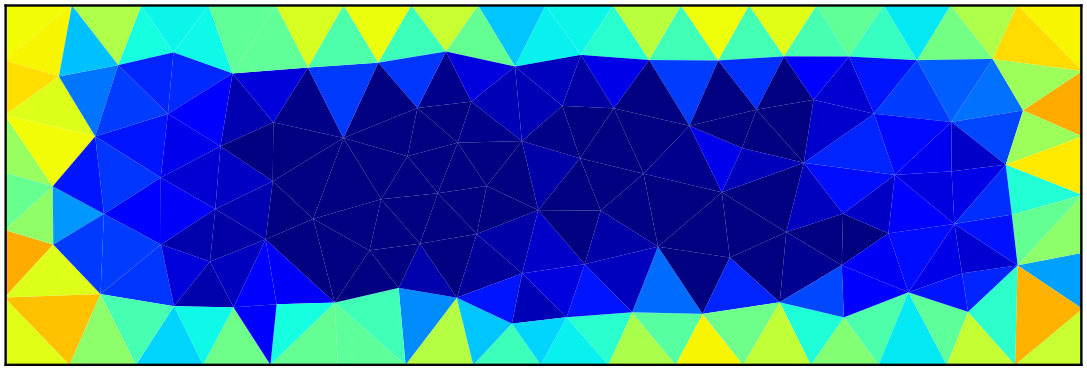

(c) RWG-based

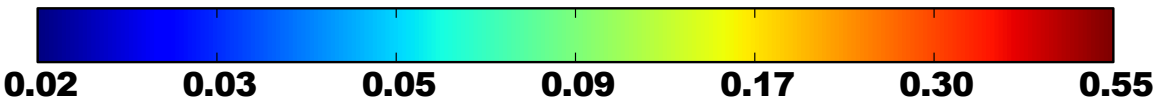

Figure 6.16: Element-wise charge error estimation η_ρ^* calculated with the three charge recovery methods (log scale).

as having a high error value. For some elements near the boundary, the estimated error is even greater than the estimated error in the neighbouring boundary elements. When considering the trend of the error and the locations of minima and maxima, it becomes evident that the RWG-based error estimator qualitatively corresponds best with the reference error distribution.

6.5.2 Global errors and global error estimations

Next, the accuracy of the recovered charges are quantitatively evaluated. The global error of the recovered charge distributions in relation to the reference solution is calculated as

$$||\rho_s^{\text{ref}} - \tilde{\rho}_s^*||_{ASL^1(S)}. \tag{6.16}$$

The results are reported in Table 6.1.

Table 6.1: Global charge errors in relation to the reference solution.

Charge distribution	Error: $\|\|\rho_s^{\text{ref}} - \tilde{\rho}_s^*\|\|_{ASL^1(S)}$
Original solution (substitute $\tilde{\rho}_s$ for $\tilde{\rho}_s^*$)	0.07897
Averaging-based recovery	0.06887
ZZ-based recovery	0.09601
RWG-based recovery	0.06600

The global estimated errors $\bar{\eta}_\rho^*$, as calculated with Equation 6.15, are reported in Table 6.2.

Table 6.2: Global estimates of the charge error in the original solution.

Charge distribution	Estimated error: $\bar{\eta}_\rho^*$
Averaging-based recovery	0.05480
ZZ-based recovery	0.07516
RWG-based recovery	0.05360

Table 6.1 provides a quantitative confirmation of conclusions drawn from the element-wise error distribution results of Figure 6.16. The RWG-based recovered charge is closest to the reference solution in a global manner. It can be observed that the ZZ recovery method increases the overall error, while averaging also manages to provide an improved version of the charge distribution. Even if in this measure, averaging might appear almost as good as the RWG-based method, it should be remembered that the RWG-based method is the only method applicable to general three-dimensional structures with surface junctions.

Looking at the estimated global error values in Table 6.2, it might seem that the RWG-based recovery error estimate is underperforming, and that the ZZ-based error estimator is the best performer, as it reports the closest value to the reference error of 0.07897. This is however not the case. A global error estimate is effectively meaningless if the local correlation of the estimated error with the actual error distribution is not taken into account. The RWG-based recovery, which conforms best to the true error distribution, estimates the global charge error at 0.05360, which can be compared to the error in the original solution of 0.07897. The underestimation is expected and can be mainly attributed to the limited ability of a linear function to model the singular nature of the charge density near the domain boundary.

6.6 Conclusions

This chapter dealt with the development of a recovery based charge error estimator for the MoM. The first step was the implementation of a charge recovery procedure. The ideas of averaging and the ZZ patch-recovery procedure were explored, and a new charge recovery procedure, based on the characteristics of the RWG basis functions, was introduced.

Charge recovery has not received much attention in the MoM community, and FEM-based gradient recovery methods thus posed an appropriate starting point for investigating charge recovery. The direct application of a nodal averaging method and the ZZ-based recovery method was however found to be generally unsuitable. The subsequently proposed RWG-based recovery method was shown to perform satisfactorily, and the use of the recovered charge for *a posteriori* error estimation was illustrated.

Chapter 7

Recovery of a MoM Current

This chapter investigates the unexplored field of MoM current recovery. Charge recovery methods can be used to give an indication of the error in a derivative of the MoM solution current. A direct measure of the error in the current is however desirable, since the current is directly related to many measurements, such as radiation patterns, impedance measurements and near- and far-field analyses. If a mixed first-order MoM current $\tilde{\mathbf{J}}$ is recovered to a higher-order current $\tilde{\mathbf{J}}^*$, the error in the current may be approximated as

$$e_{\mathbf{J}} \approx e_{\mathbf{J}}^* = \tilde{\mathbf{J}}^* - \tilde{\mathbf{J}}. \tag{7.1}$$

Methods of recovering higher-order currents $\tilde{\mathbf{J}}^*$, and the accuracy of such recovered currents, are considered in this chapter. Figure 7.1 shows the current magnitude $|\tilde{\mathbf{J}}|$ of the mixed first-order MoM solution of the example PEC plate introduced in the previous chapter. The improvement of this surface current $\tilde{\mathbf{J}}$ is the main goal of this chapter.

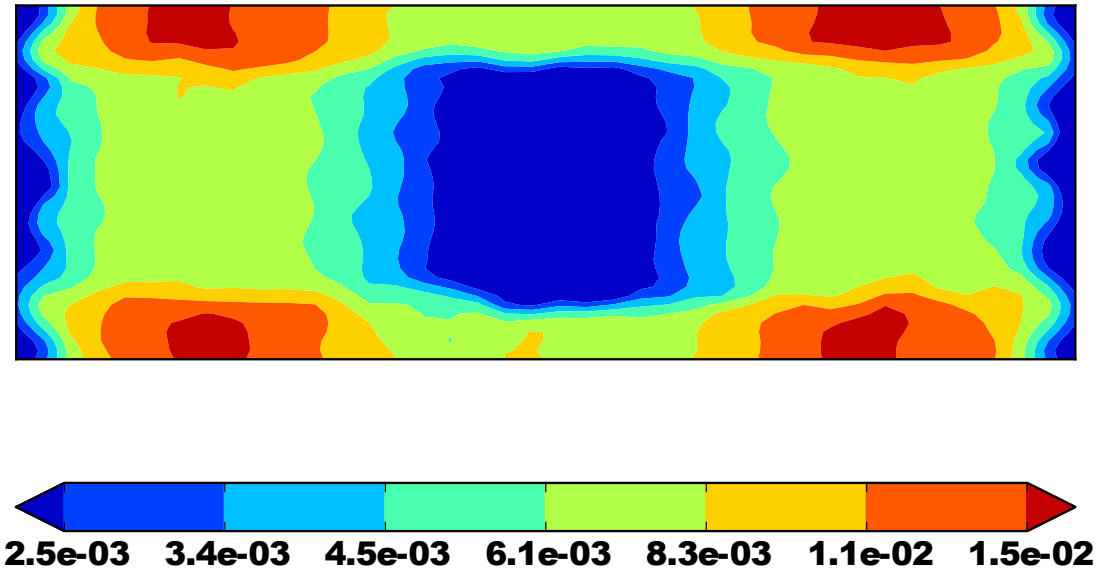

Figure 7.1: Current magnitude of a mixed first-order MoM solution on a PEC patch (log scale).

Recall that the RWG basis functions used in the MoM discretisation are mixed first-order

divergence-conforming functions. As discussed in Section 5.4, divergence-conforming functions ensure normal continuity between mesh elements. In this chapter, higher-order divergence-conforming functions are utilised to construct the improved current $\tilde{\mathbf{J}}^*$.

A reference solution $\mathbf{J}^{\text{ref}}$ is once again obtained with a mixed first-order MoM solution on a factor-four h-refined version of the original mesh, and is given in Figure 7.2.

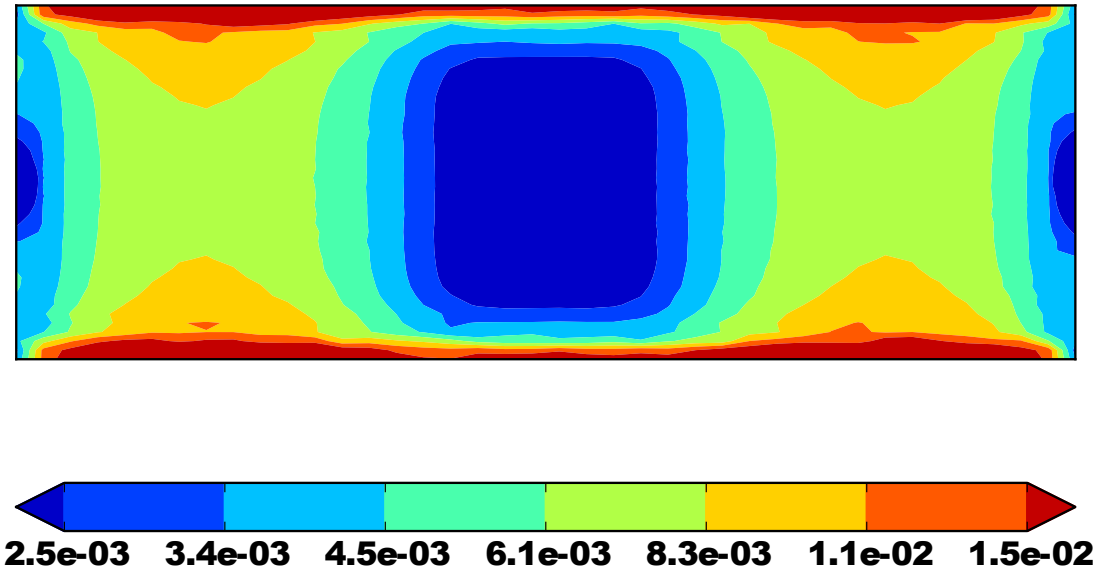

Figure 7.2: Reference current magnitude obtained on a factor-four h-refined version of the original mesh (log scale).

7.1 Extraction of solenoidal components

With the work of Chapter 6, the numerical charge $\tilde{\rho}_s$ of a mixed first-order MoM solution, being a piecewise-constant scalar field, can effectively be recovered to a piecewise-linear scalar function $\tilde{\rho}_s^*$. It follows that a mixed second-order current $\tilde{\mathbf{J}}^*$ could be recovered, with an associated surface charge

$$\nabla_s \cdot \tilde{\mathbf{J}}^* = \tilde{\rho}_s^*. \tag{7.2}$$

The RWG elements that are employed in the original current solution $\tilde{\mathbf{J}}$, however contain a solenoidal component of order zero. The charge constraint of Equation 7.2, imposed on the recovered current $\tilde{\mathbf{J}}^*$, only specifies a recovery of the divergent component of the current, since the solenoidal component has no associated charge. It is therefore required to decompose the RWG-based solution current $\tilde{\mathbf{J}}$ into its respective divergent and solenoidal components, in order to extract and preserve the zero-order solenoidal component of the original solution. The inexact Helmholtz decomposition of the RWG elements, where the elements are decomposed into solenoidal and divergent components, is given in Equation 5.14, in Section 5.4. A tree-cotree decomposition, as introduced in

Section 5.5, is used for the decomposition. With this approach, the function space of the mixed first-order RWG functions $\mathbf{D}_1$, is replaced by the equivalent function space formed by the direct sum of the solenoidal tree function space and the divergent cotree function space.

$$\{\mathbf{D}_{1,n}; n \in E\} \equiv \{\mathbf{D}_{1,m}; m \in E_{\text{cotree}}\} \oplus \{\mathbf{S}_{0,i}; i \in V_{\text{tree}}\}, \tag{7.3}$$

where E is the set of all internal edges decomposed into E_{tree} and E_{cotree}, V_{tree} is the set of all tree vertices, and $\mathbf{S}_0$ are the zero-order solenoidal functions, introduced in Section 5.4.2.

A projection of the solution current $\tilde{\mathbf{J}}$ onto the solenoidal function space of $\mathbf{S}_0$, enables the extraction of the associated solenoidal component $\tilde{\mathbf{J}}_{\text{tree}}$, as shown in Figure 7.3.

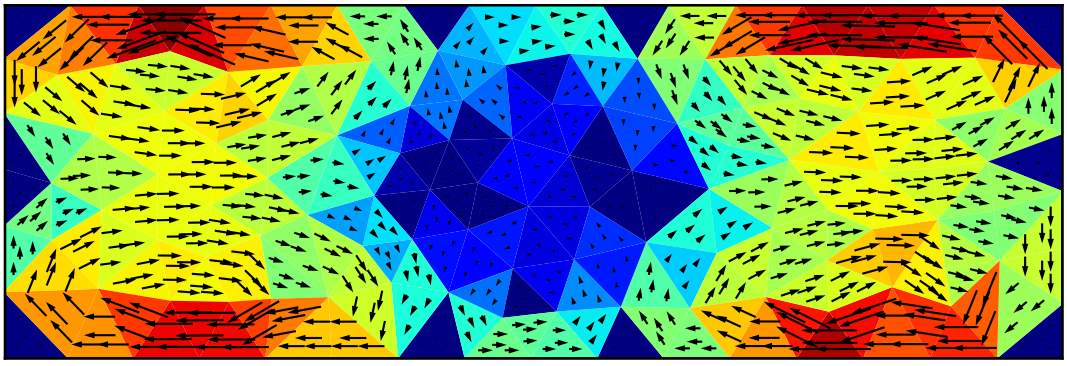

(a) Phase $\omega t = 0^o$

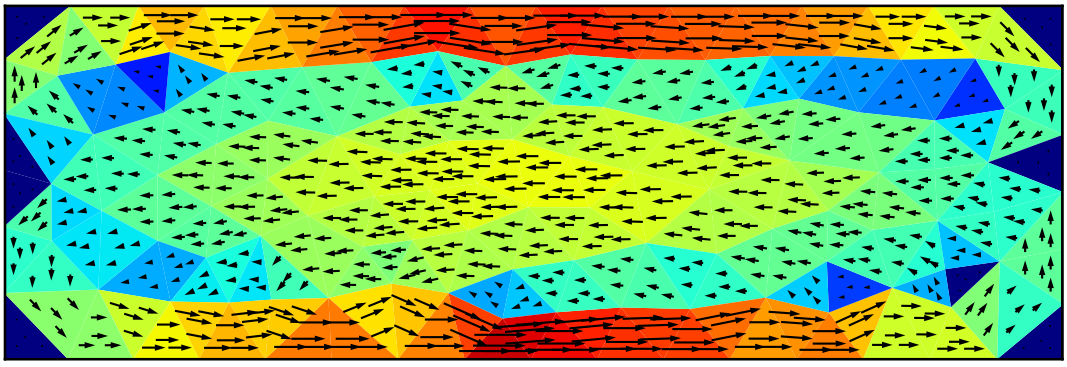

(b) Phase $\omega t = 90^o$

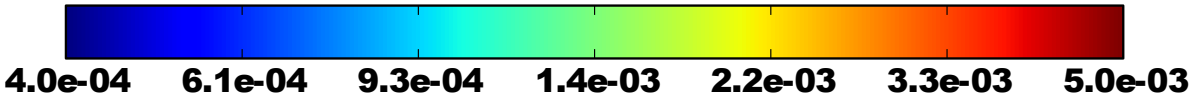

Figure 7.3: Instantaneous current components, $\omega t = 0^o$ and $\omega t = 90^o$, of zero-order solenoidal current $\tilde{\mathbf{J}}_{\text{tree}}$ (log scale).

The projection procedure is similar to the testing procedure of the MoM formulation, as presented in Chapter 3. A symmetric inner product of two functions defined as

$$\langle \mathbf{f}, \mathbf{g} \rangle \equiv \int_S \mathbf{f} \cdot \mathbf{g} \, dS, \tag{7.4}$$

is used for the projection. A set of coefficients I_{tree} is required, with which the expansion of the zero-order solenoidal current component, given as

$$\tilde{\mathbf{J}}_{\text{tree}} = \sum_{i=1}^{N} I_{\text{tree}} \mathbf{S}_{0,i}, \tag{7.5}$$

can be found. The coefficients are calculated by solving the sparse matrix equation

$$\langle \tilde{\mathbf{J}}_{\text{tree}}, \mathbf{S}_{0,j} \rangle = \langle \tilde{\mathbf{J}}, \mathbf{S}_{0,j} \rangle. \tag{7.6}$$

The two components of the solenoidal current of the reference solution, reported in Figure 7.4, are available for comparison.

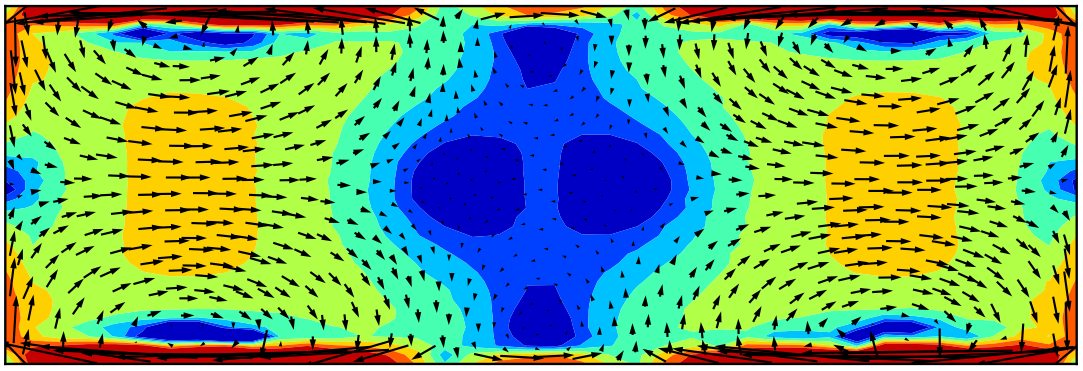

(a) Phase $\omega t = 0^o$

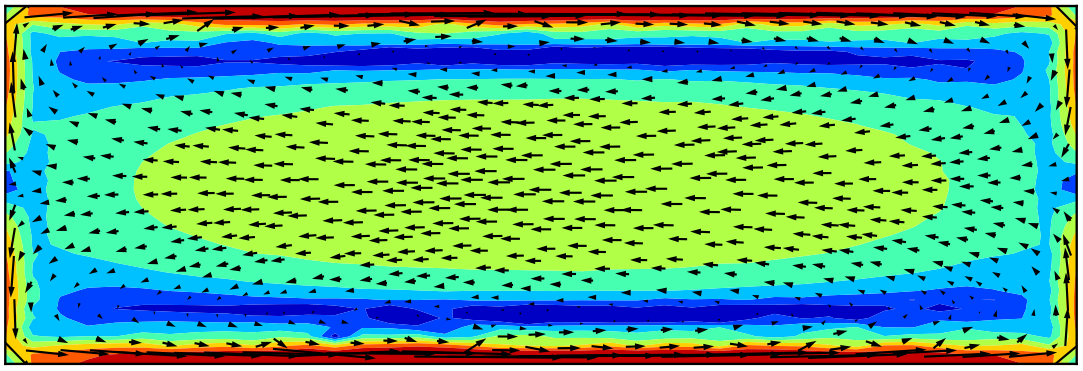

(b) Phase $\omega t = 90^o$

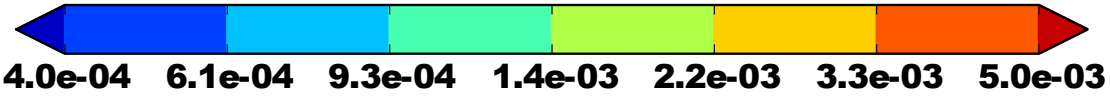

Figure 7.4: Instantaneous current components, $\omega t = 0^o$ and $\omega t = 90^o$, of reference solution, obtained on a factor-four h-refined version of the original mesh (log scale).

The solenoidal current $\tilde{\mathbf{J}}_{\text{tree}}$ can now be added to a recovered divergent current in order to obtain an improved version of the original current. It is necessary to perform further recovery of the solenoidal component prior to constructing the final recovered current $\tilde{\mathbf{J}}^*$ in order to increase accuracy.

7.2 A recovery procedure for the first-order divergent current components

To satisfy the charge constraint imposed on the recovered current $\tilde{\mathbf{J}}^*$ by Equation 7.2, a divergent current component $\tilde{\mathbf{J}}_{\text{div}}$ is required with an associated recovered first-order charge of $\tilde{\rho}_s^*$. The RWG-based recovered charge $\tilde{\rho}_s^*$, as obtained in Section 6.4, is used for this purpose. The required current belongs to a divergent function space, which is represented as

$$\tilde{\mathbf{J}}_{\text{div}} \in \{\mathbf{D}_{1,m}; m \in E_{\text{cotree}}\} \oplus \{\mathbf{D}_{20,t}, \mathbf{D}_{21,t}; t \in T\}, \tag{7.7}$$

where T is the set of all triangles of the mesh and $\mathbf{D}_{20}$ and $\mathbf{D}_{21}$ are second-order divergent basis functions, as introduced in Section 5.4.4. The function space thus consists of two second-order functions per triangle face and one first-order RWG function per cotree edge.

The coefficients of the second-order face functions, $\mathbf{D}_{20}$ and $\mathbf{D}_{21}$, are determined first. These two functions have a first-order associated charge and are the only functions within the combined function space of Equation 7.7 with non-constant surface charge distributions. The coefficients of the two functions of each triangle are calculated by matching the gradient of the recovered charge $\tilde{\rho}_s^*$ on that triangle. This matching is performed on a per-element basis. A constant charge value remains on each triangle to be matched by the first-order functions.

The first-order edge functions overlap since each has a constant charge value associated with two triangles. The coefficients can however still be calculated locally if they are computed in a suitable order. Looking at the base of a tree graph, as shown in Figure 7.5, triangular elements are found that have only one associated cotree edge. The coefficients

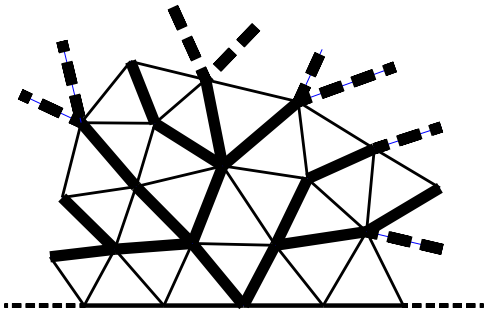

Figure 7.5: Base of a tree graph.

of these cotree edge functions $\mathbf{D}_1$, are thus uniquely determined by the required charge values of these triangles. Moving up the tree, the next group of elements encountered will now be associated with only one free cotree edge that is once again uniquely determined by the charge requirements of these elements. In this manner, all the coefficients of the cotree edge functions $\mathbf{D}_1$ are calculated.

The current $\tilde{\mathbf{J}}_{\text{div}}$, satisfies the charge requirement represented by Equation 7.2. An unspecified solenoidal component is however contained within this current since the divergent basis functions are not orthogonal to the first-order solenoidal function space. The projection method introduced in Section 7.1 can be used to extract and filter out the solenoidal components of $\tilde{\mathbf{J}}_{\text{div}}$. After the filtering is performed, a recovered current is found as

$$\tilde{\mathbf{J}}^* = \tilde{\mathbf{J}}_{\text{div},\perp} + \tilde{\mathbf{J}}_{\text{tree}}, \tag{7.8}$$

with

$$\tilde{\mathbf{J}}_{\text{div},\perp} \perp \tilde{\mathbf{J}}_{\text{tree}}. \tag{7.9}$$

This recovered current, which contains second-order divergent and zero-order solenoidal components, is shown in Figure 7.6.

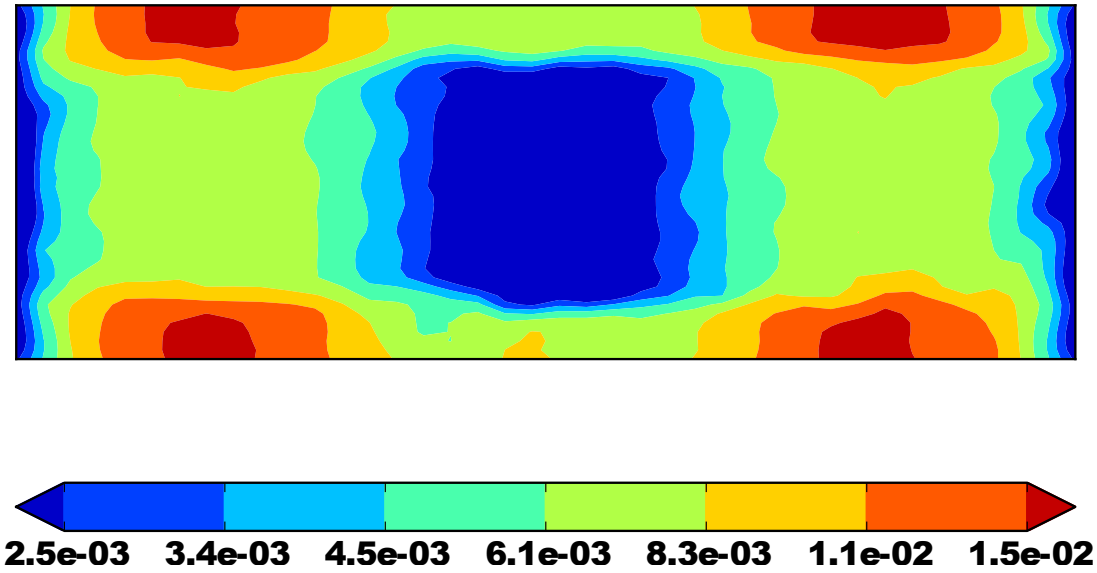

Figure 7.6: Recovered divergent current with solenoidal component of original solution (log scale).

A slight improvement in the smoothness of the current, when compared to the original current solution of Figure 7.1, is noticeable. The recovered current also appears to have slightly higher symmetry, but remains mostly asymmetrical. By looking at the reference current of Figure 7.2, these two changes can be seen to be improvements. The current peaks were however not significantly pushed towards and spread out over the domain boundary, as can be seen to be the case with the reference current. The accuracy of the recovered current may be qualitatively evaluated by considering a plot of the difference between the reference and recovered currents. Such a plot is given in Figure 7.7. This difference plot indicates a fair correlation between the recovered current and the reference current, but confirms prevailing inaccuracies on the domain boundary near the locations of the current peaks. Further recovery of the solenoidal current component is required to increase the accuracy of the recovered current.

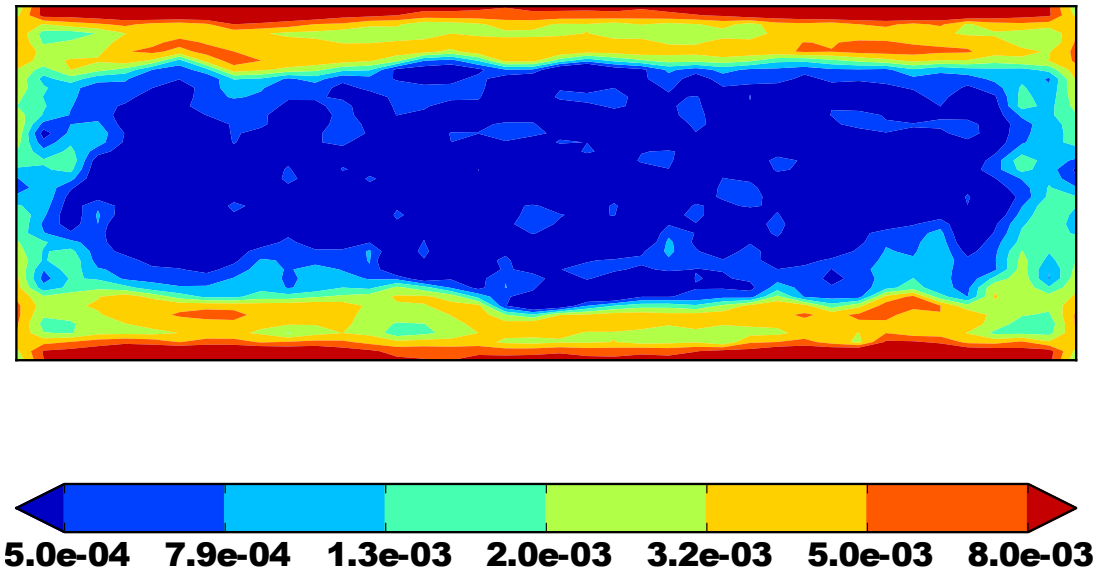

Figure 7.7: Difference between reference current and recovered divergent current with solenoidal component of original solution (log scale).

7.3 Recovery procedures for the zero-order solenoidal current components

The recovered current may be further enhanced by finding an improved solenoidal current representation $\tilde{\mathbf{J}}_{\text{sol}}$. It seems reasonable that the piecewise-constant solenoidal current, $\tilde{\mathbf{J}}_{\text{tree}}$ of Figure 7.3, could also be used to find a recovered piecewise-linear representation, as was done for the piecewise-constant charge. The recovered current belongs to the first-order solenoidal function space, represented as

$$\tilde{\mathbf{J}}_{\text{sol}} \in \{\mathbf{S}_{0,i}; i \in V_{\text{tree}}\} \oplus \{\mathbf{S}_{1,n}; n \in E\}, \tag{7.10}$$

where $\mathbf{S}_0$ are the tree-functions, and $\mathbf{S}_1$ are edge based first-order solenoidal functions, as introduced in Section 5.4.3. Two solenoidal current recovery methods are now introduced.

7.3.1 A potential-based recovery procedure

The first proposed method introduces a scalar potential field Ψ, that is associated with the zero-order solenoidal field as

$$\tilde{\mathbf{J}}_{\text{tree}} = \mathbf{u}_T \times \nabla\Psi, \tag{7.11}$$

where $\mathbf{u}_T$ is the unit vector normal to the surface of triangle T. This potential field is a piecewise-linear continuous scalar field that is defined by the potential values at the tree nodes. The node that forms the base of the tree is chosen to have a zero potential, and subsequent potential values are calculated from a potential difference as

$$\Psi_{ab} = \int_b^a (\mathbf{u}_T \times \tilde{\mathbf{J}}_{\text{tree}}) \cdot d\boldsymbol{\ell}. \tag{7.12}$$

The nodal values of the potential field are directly related to the coefficients of the original solenoidal current $\tilde{\mathbf{J}}_{\text{tree}}$ and carry the highest level of accuracy. The recovered solenoidal current will thus be constructed from an improved potential field with the values at the mesh nodes left unaltered.

Each of the first-order edge-based solenoidal functions $\mathbf{S}_{1,n}$, are defined on a local patch formed by the triangle pair that share the n^{th} edge. Such a function has an associated second-order potential that is zero on the boundary and at the nodes of the local patch. The recovered solenoidal current $\tilde{\mathbf{J}}_{\text{sol}}$ will thus retain the coefficients of the original zero-order solenoidal tree elements in order to maintain the potential values at the tree nodes. Improved potential values at the midpoints of internal edges are however required to calculate the coefficients of the first-order solenoidal functions $\mathbf{S}_1$.

For the recovery of new midpoint potentials Ψ_n, consider the local patch formed around the n^{th} edge, as shown in Figure 7.8. A piecewise-linear continuous potential field, and

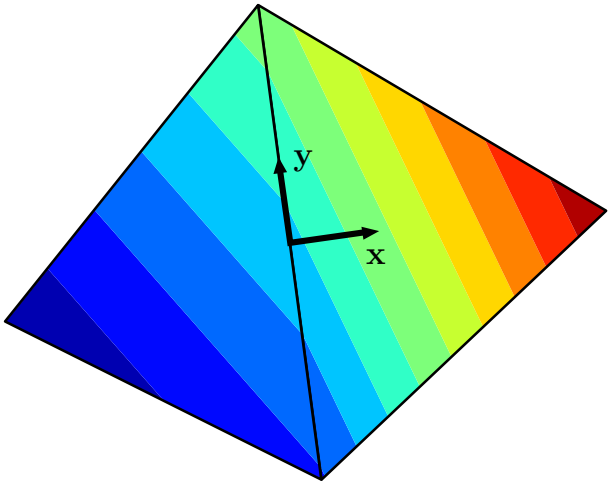

Figure 7.8: Piecewise-linear continuous potential field on a local patch.

a local coordinate system $\mathbf{x}$ $\mathbf{y}$, centered at the midpoint of, and aligned with edge n, are also introduced in Figure 7.8. In terms of the offered local coordinates, the potential field within the two triangles may be described with the use of four coefficients as

$$\begin{aligned} \Psi_{Tn_1} &= Ax + By + C \\ \Psi_{Tn_2} &= Dx + By + C. \end{aligned} \tag{7.13}$$

The variation of the potential field in the $\mathbf{y}$-direction is unchanged throughout the local patch. Since the recovery of this $By + C$ component would yield trivial results, it is subtracted from the potential field prior to applying the recovery scheme. The potential field is now fully described by a piecewise-linear variation in the $\mathbf{x}$-direction, as shown in Figure 7.9 (a different scale to Figure 7.8 is used). The four points indicated on Figure 7.9,

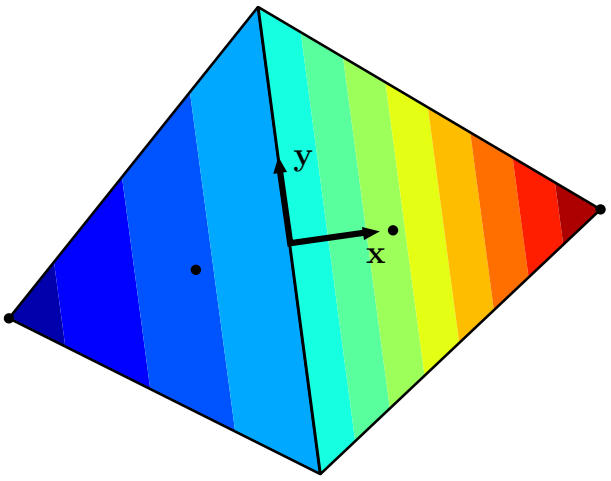

Figure 7.9: Piecewise-linear **x**-variation of a potential field on a local patch.

the two outer nodes and the two triangle centroids, can be used in a least squares fit to a quadratic function

$$\alpha x^2 + \beta x + \gamma. \tag{7.14}$$

This quadratic **x**-variation is employed in the potential field shown in Figure 7.10.

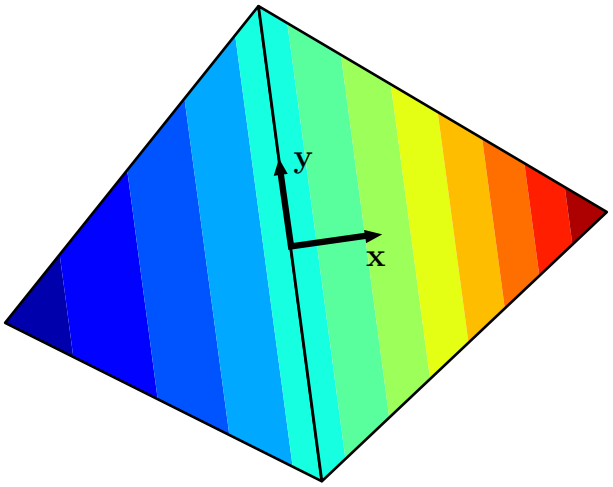

Figure 7.10: Quadratic **x**-variation of a potential field on a local patch.

The previously extracted component of **y**-variation, $By + C$, is now reinserted to form the final local potential field of

$$\alpha x^2 + \beta x + By + \gamma + C, \tag{7.15}$$

from which the edge midpoint potential Ψ_n is extracted as

$$\Psi_n = \gamma + C. \tag{7.16}$$

The complete local potential field, as used for the recovery, is shown in Figure 7.11. The

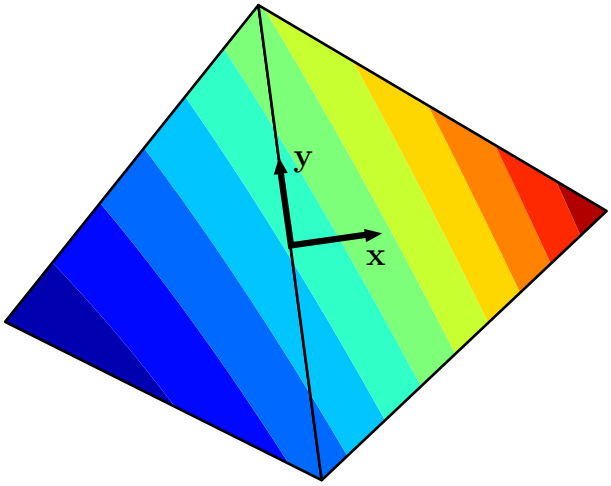

Figure 7.11: Recovered quadratic potential field on a local patch.

locally recovered potential values are used to calculate the coefficients of the first-order solenoidal functions $\mathbf{S}_1$ from

$$\Psi(0) - \Psi(-\ell_n/2) = \int_{-\ell_n/2}^{0} \mathbf{u}_T \times (\tilde{\mathbf{J}}_{\text{tree}} + s_n \mathbf{S}_{1,n})\, dy, \tag{7.17}$$

where Ψ is expressed as a function along edge n with $\Psi(0) = \Psi_n$, ℓ_n is the length of edge n, and s_n is the coefficient of the first-order solenoidal function $\mathbf{S}_{1,n}$. The potential-based recovered first-order solenoidal current is shown in Figure 7.12.

A distinct smoothing of the piecewise-constant loop functions, $\tilde{\mathbf{J}}_{\text{tree}}$ of Figure 7.3, is observed, with the arrows appearing to change direction more gradually. A *spillover* of current from active elements into dead-spots, as found at corner elements, is also expected to be beneficial to the accuracy of the recovery. The reference solenoidal current, given in Figure 7.4, indeed does not have these dead-spots, which indicates them to be artefacts of the coarse solution mesh.

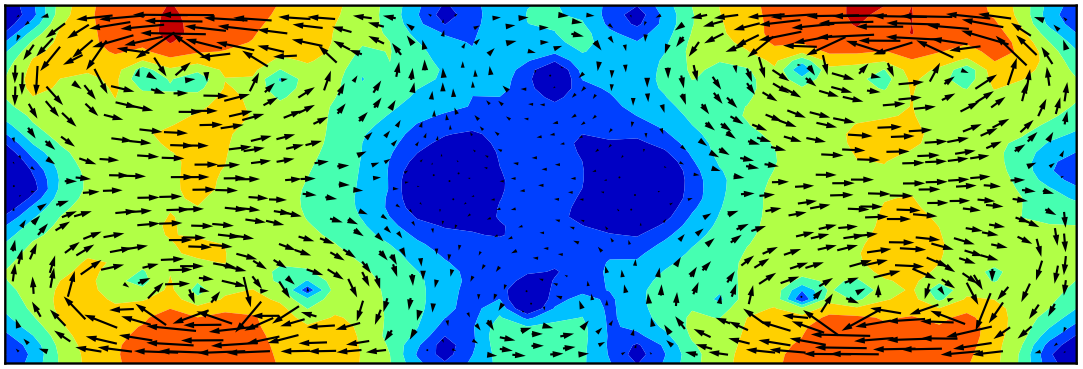

(a) Phase $\omega t = 0^o$

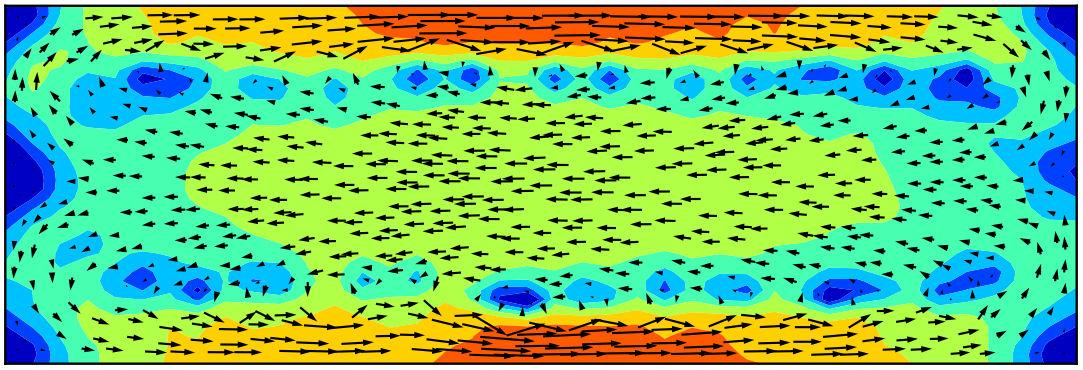

(b) Phase $\omega t = 90^o$

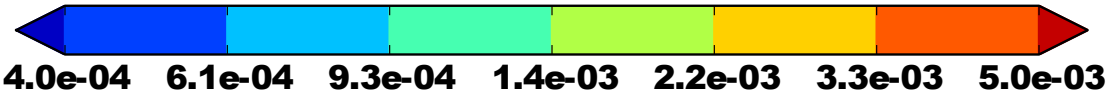

Figure 7.12: Instantaneous current components, $\omega t = 0^o$ and $\omega t = 90^o$, of potential-based recovered first-order solenoidal current $\tilde{\mathbf{J}}_{\text{sol}}$ (log scale).

With an improved solenoidal current component now available, a mixed second-order recovered current is formulated as

$$\tilde{\mathbf{J}}^* = \tilde{\mathbf{J}}_{\text{div},\perp} + \tilde{\mathbf{J}}_{\text{sol}}. \tag{7.18}$$

This recovered current, now containing second-order divergent and first-order solenoidal components, is shown in Figure 7.13. Even further improvement of the smoothness of the current is observed. The recovered current also appears to be more symmetrical, but remains mostly asymmetrical. The current peaks are still not significantly pushed towards and spread out over the domain boundary, as can be seen to be the case with the reference current. The difference between the reference and recovered currents, given in Figure 7.14, is once again used for a qualitative analysis of the recovery. The difference plot indicates a fair correlation between the recovered current and the reference current, but confirms the presence of the same inaccuracies on the domain boundary near the

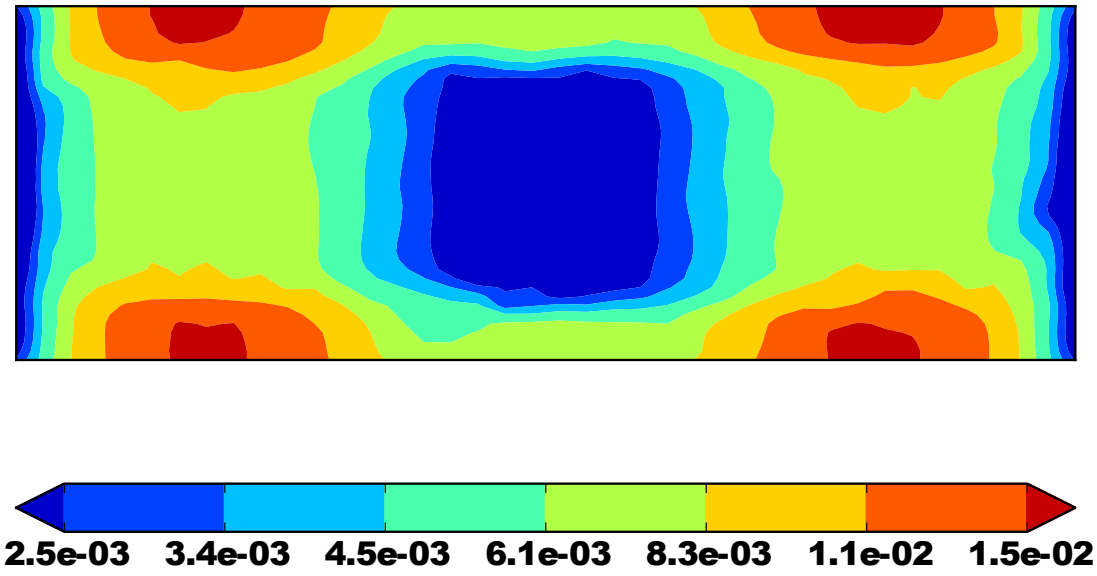

Figure 7.13: Potential-based recovered mixed second-order current magnitude (log scale).

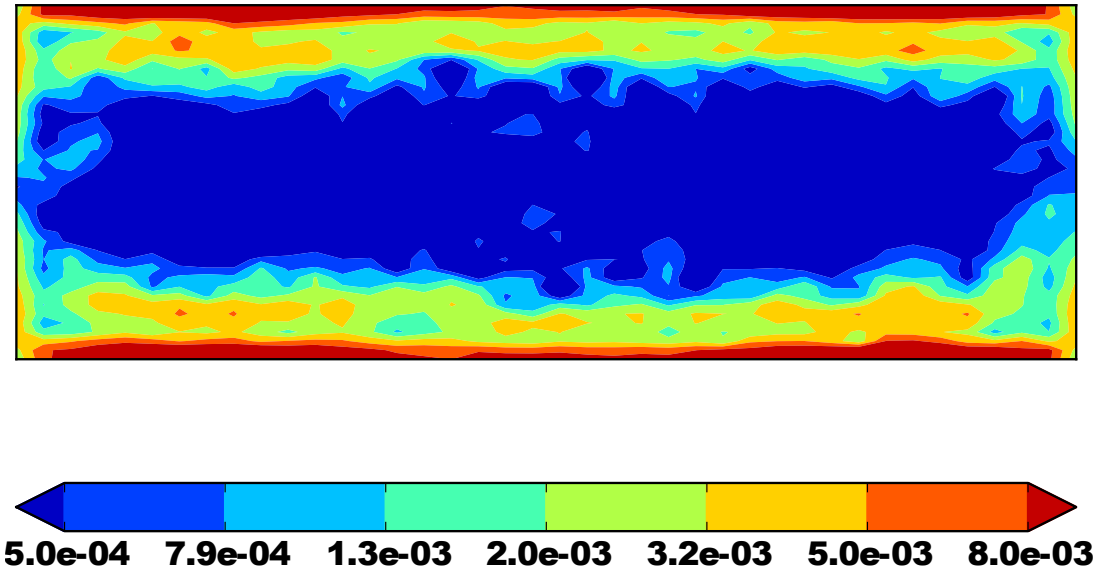

Figure 7.14: Difference between reference current and mixed second-order potential-based recovered current (log scale).

locations of the current peaks. Qualitatively, it does appear as though the addition of the first-order solenoidal components effected a reduction in the overall error of the solution.

7.3.2 A vector-based recovery procedure

The second proposed recovery method is constructed directly from the current components of the zero-order solenoidal field $\tilde{\mathbf{J}}_{\text{tree}}$. Within each triangle T, the solenoidal current may be represented as

$$\tilde{\mathbf{J}}_{\mathbf{tree},T} = A\mathbf{x} + B\mathbf{y}. \tag{7.19}$$

Each current component is thus a piecewise-constant discontinuous scalar field. The RWG-based charge recovery method, that was developed in Section 6.4 for application to the piecewise-constant charge distributions, may be employed directly onto these scalar fields to extract improved values at the midpoints of internal mesh edges.

In the charge recovery context, the functions that were added to match the locally recovered charge values were face functions, each constrained to a single triangle. The first-order edge based solenoidal functions $\mathbf{S}_{1,n}$, considered here, are defined on a local patch formed by the triangle pair that share the n^{th} edge. For each edge function, the component normal to the internal edge has a linear variation along that edge, with zero net flow across the edge (See Section 5.4.3 for further details). The first order solenoidal function space, given in Equation 7.10, thus allows the component of current flow normal to internal edges, to take on a linear variation.

To calculate a desired linear variation across the n^{th} edge, the local patch around this edge is considered. The two current components, as given in Equation 7.19, are recovered at the midpoints of all the edges that do not fall on the boundary of the global mesh. This recovery is achieved through the same procedure as was used for the RWG-based surface charge recovery at edge midpoints (see Figure 6.11). The components of the recovered values in the direction normal to the central edge are retained, as shown in Figure 7.15. These values will form the input data to a least squares problem. The

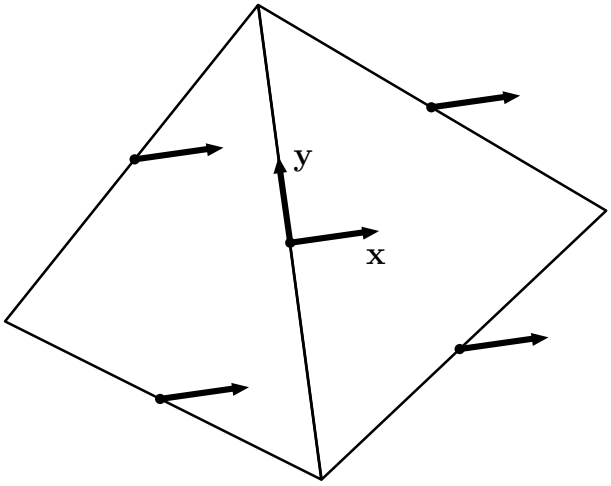

Figure 7.15: Recovered vector components on a local patch.

components of the recovered values in the direction tangential to the central edge are discarded since the present function space cannot be used to match these values. Once again, a local coordinate system $\mathbf{x}$ $\mathbf{y}$, centered at the midpoint of, and aligned with edge n, is utilised. The $\mathbf{x}$-directed vector at the centre of the patch has a trivial recovery, since the normal component of current flow across this edge is constant and continuous. It is desirable to leave this central value unchanged, as it describes the total amount of

current flowing across the edge. The zero-order solenoidal tree-functions are the only functions contributing to the total current flow across the central edge, and as such, the coefficients of $\tilde{\mathbf{J}}_{\text{tree}}$ are once again left unchanged. After subtracting the constant value of the central $\mathbf{x}$-directed vector from all the recovered vectors, four vectors are available for the calculation of the linear variation of the normal component along the n^{th} edge. These vectors may be utilised in a least squares manner to a reduced linear vector field, represented as

$$(\alpha x + \beta y)\mathbf{x}. \tag{7.20}$$

The coefficient of the first-order solenoidal function $\mathbf{S}_{1,n}$ is calculated from the linear variation of this vector field along edge n. This variation is characterised by the non-zero value at the top node of the n^{th} edge, found as

$$\beta \frac{\ell_n}{2}, \tag{7.21}$$

where ℓ_n is the length of the n^{th} edge.

Special considerations

Some mesh geometries require special attention when implementing the vector-based recovery method as proposed here.

The special cases related to the recovery of the vector values needed to construct the local patch of Figure 7.15, are addressed in the discussion of the RWG-based charge recovery method, given in Section 6.4. These cases include the handling of curved surfaces, surface junctions and re-entrant corners.

Since the local patches are now formed by two triangles, as opposed to just one, boundary elements require a new approach. For a local patch constructed with edges that fall on the domain boundary, a recovered vector cannot be assembled for all the edges. The original vector value at the triangle centroid is substituted for each boundary edge in the construction of the least-squares system.

The two instantaneous components of the final vector-based recovered first-order solenoidal current $\tilde{\mathbf{J}}_{\text{sol}}$ is shown in Figure 7.16. The zero-order loop functions, $\tilde{\mathbf{J}}_{\text{tree}}$ of Figure 7.3, can be seen to be smoothed out quite well in Figure 7.16, with the arrows appearing to change direction more gradually. This recovery also accomplishes a *spillover* of current from active elements into dead-spots, which the reference solenoidal current of Figure 7.4 determines to be necessary.

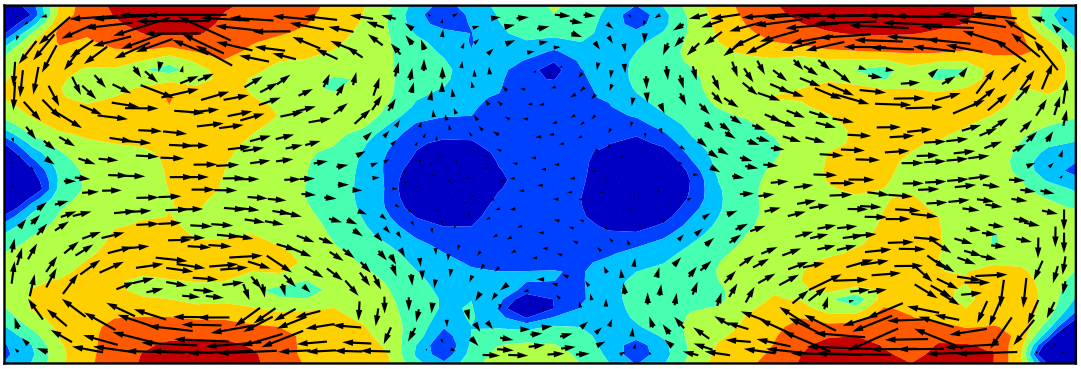

(a) Phase $\omega t = 0^o$

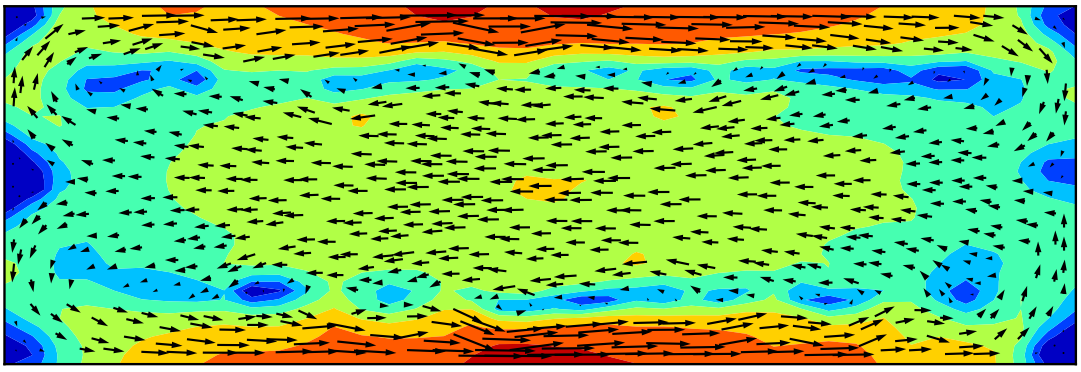

(b) Phase $\omega t = 90^o$

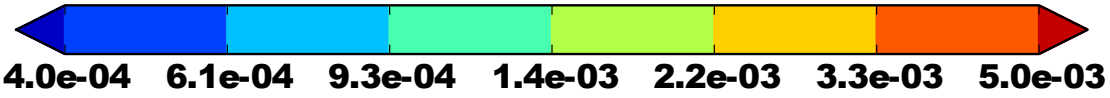

Figure 7.16: Instantaneous current components, $\omega t = 0^o$ and $\omega t = 90^o$, of recovered vector-based first-order solenoidal current $\tilde{\mathbf{J}}_{\text{sol}}$ (log scale).

With an improved solenoidal current component available, a mixed second-order recovered current is formulated as

$$\tilde{\mathbf{J}}^* = \tilde{\mathbf{J}}_{\text{div},\perp} + \tilde{\mathbf{J}}_{\text{sol}}. \tag{7.22}$$

This recovered current, which also contains second-order divergent and first-order solenoidal components, is shown in Figure 7.17.

This recovered current exhibits the highest smoothness and symmetry. Furthermore, the current peaks seem to be effectively pushed towards and spread out over the domain boundary, although it is not quite as pronounced as is the case with the reference current. The difference between the reference and recovered currents, given in Figure 7.18, is once again used for a qualitative analysis of the recovery.

The difference plot indicates the best correlation between the recovered current and the reference current as seen for the considered recovery options. A definite reduction in the size of the red high-difference zones on the patch is observed. The remaining

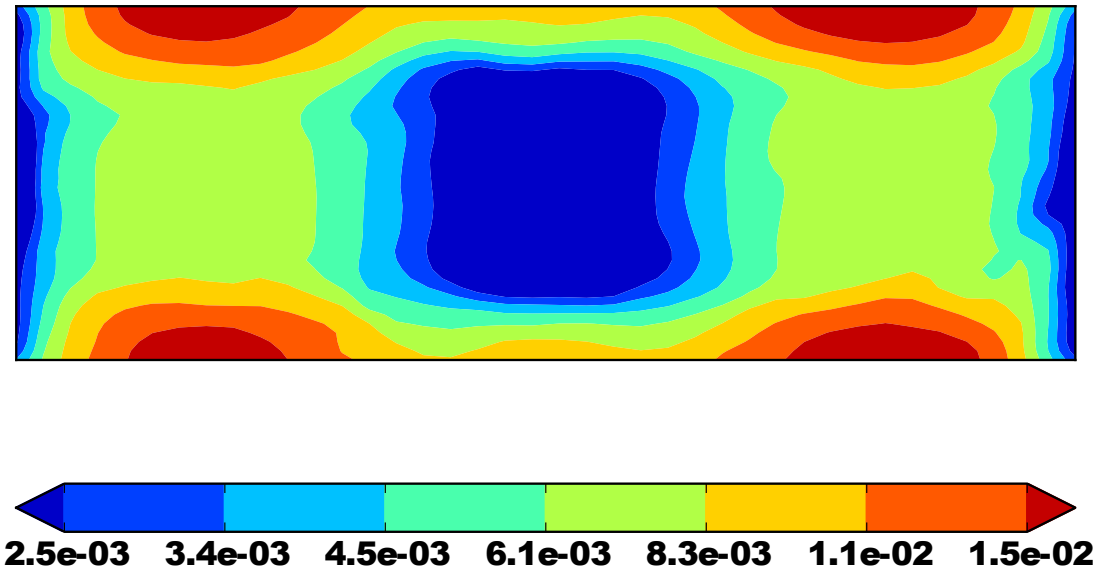

Figure 7.17: Vector-based recovered mixed second-order current magnitude (log scale).

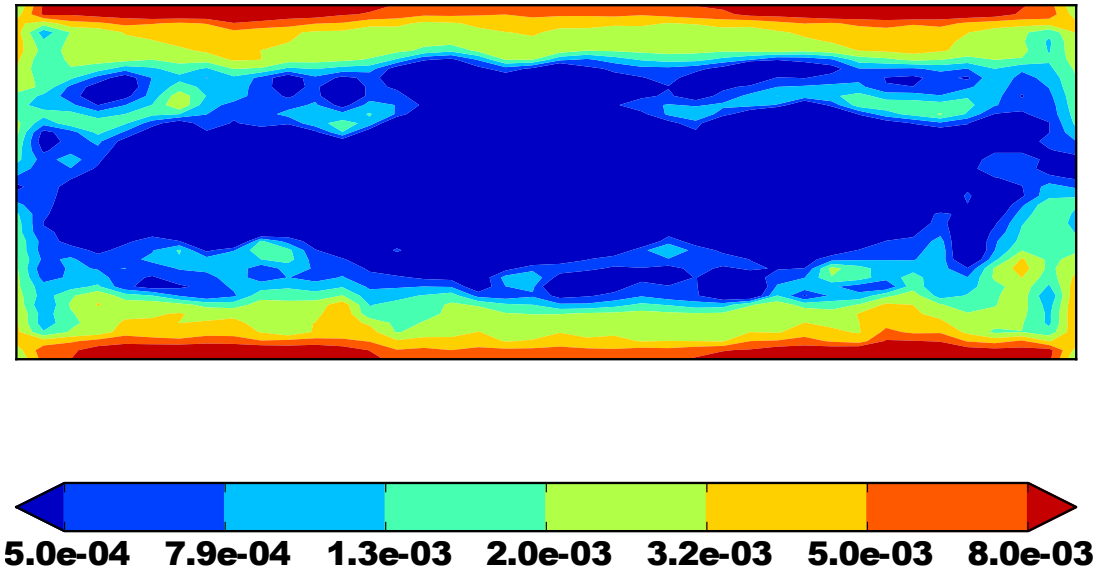

Figure 7.18: Difference between reference current and mixed second-order vector-based recovered current (log scale).

inaccuracies on the domain boundary are to be expected, when considering the limited input received from the coarse mesh and the mixed first-order current solution $\tilde{\mathbf{J}}$.

7.4 A full first-order recovered current

It is also possible to consider a full first-order recovered current, where only the order of the associated solenoidal component is increased. This approach carries the advantage of reducing the involved computational cost by cutting out numerous steps involved in the mixed second-order recovery procedure. The charge recovery step is no longer needed

since the divergent recovery is no longer applied. The tree-cotree decomposition also becomes redundant, since the zero-order solenoidal component needed for the solenoidal recovery procedure may be extracted without explicitly defining a tree-graph.

The vector-based recovered current $\tilde{\mathbf{J}}_{\text{sol}}$, as calculated in the previous section, is considered. A full first-order recovered current is constructed as

$$\tilde{\mathbf{J}}^* = \tilde{\mathbf{J}} + \tilde{\mathbf{J}}_{\mathbf{S}_1}, \tag{7.23}$$

where $\tilde{\mathbf{J}}_{\mathbf{S}_1}$ is the first-order component of $\tilde{\mathbf{J}}_{\text{sol}}$. The zero-order solenoidal component of $\tilde{\mathbf{J}}_{\text{sol}}$ is already contained in the original solution $\tilde{\mathbf{J}}$. This full first-order recovered current is shown in Figure 7.19.

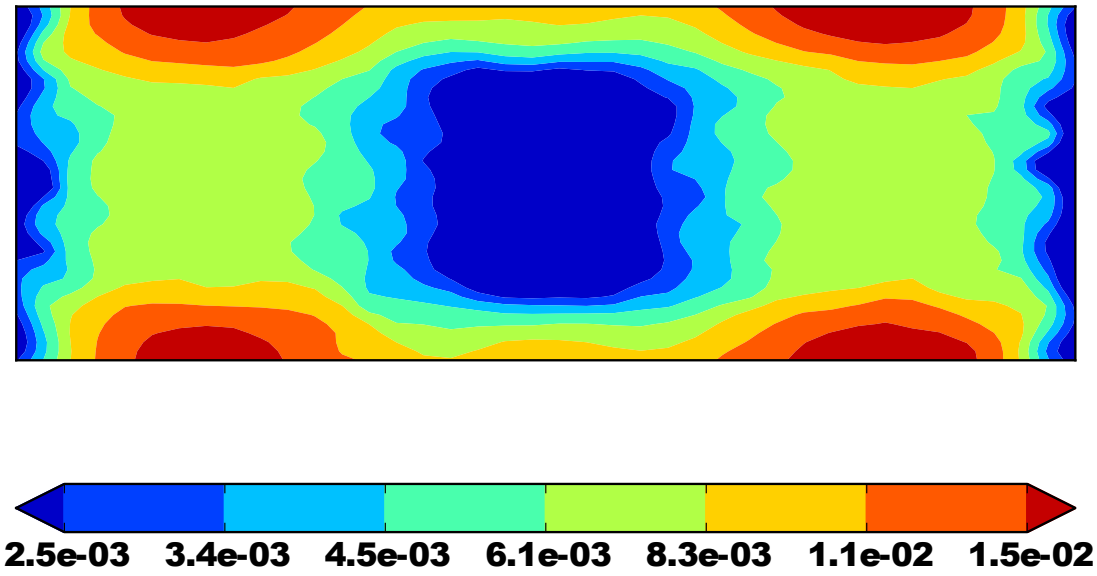

Figure 7.19: Vector-based recovered full first-order current magnitude (log scale).

The recovered current has lost some of the smoothness that was present in the mixed second-order recovered current. The symmetry of the current distribution, and the improvements around the current peaks are largely retained. Given the simplicity of this implementation, the results are particularly encouraging. A difference plot between the reference and recovered currents is provided in Figure 7.20.

The difference plot shows that the accuracy of the recovery on the domain boundary is largely retained. An increase in the error can be seen to occur internally, and the full first-order recovered current is thus expected to have a higher global error than the mixed second-order version.

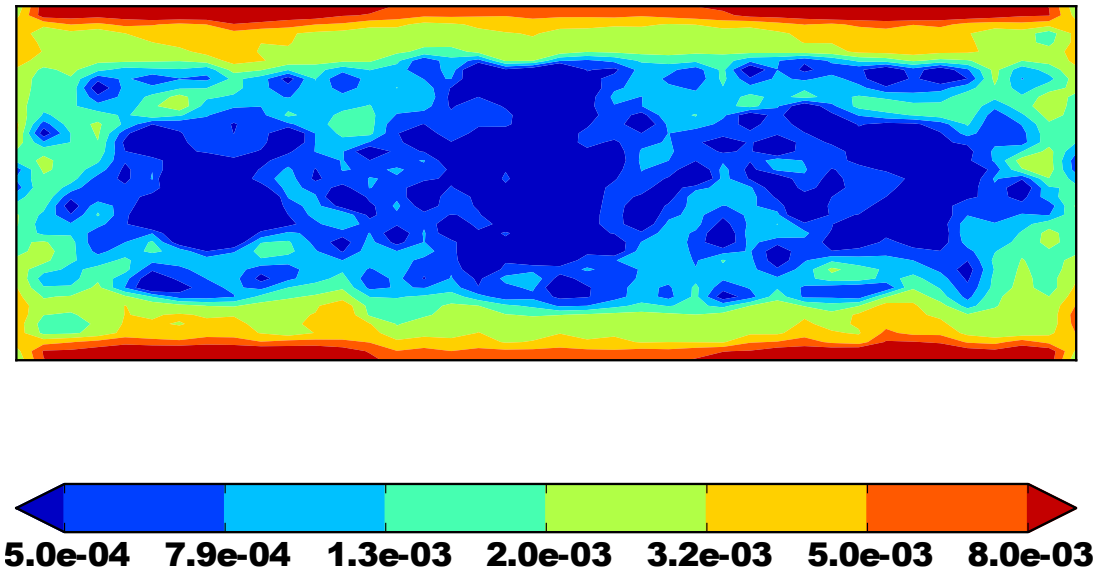

Figure 7.20: Difference between reference current and full first-order vector-based recovered current (log scale).

7.5 A posteriori error estimation of the MoM current

The availability of $\tilde{\mathbf{J}}^*$, an estimate of the true current distribution $\mathbf{J}$, enables the constructions of a current error estimator. An approximation to the true current error can be found as

$$e_{\mathbf{J}} \approx e_{\mathbf{J}^*} = \tilde{\mathbf{J}}^* - \tilde{\mathbf{J}}. \tag{7.24}$$

An element-wise error estimator, as well as an estimate of the global current error, can be obtained from Equation 7.24. Once again, the area-scaled L^1-norm is used.

$$||\cdot||_{ASL^1(\Omega)} \equiv \frac{\int_\Omega |\cdot| \, dS}{\text{Area}(\Omega)}. \tag{7.25}$$

The element-wise error estimators are then obtained as

$$\eta^*_{\mathbf{J}} = ||e^*_{\mathbf{J}}||_{ASL^1(T)}, \tag{7.26}$$

on a triangular domain T, and the global current error estimate is found as

$$\bar{\eta}^*_{\mathbf{J}} = ||e^*_{\mathbf{J}}||_{ASL^1(S)}, \tag{7.27}$$

where S denotes the entire surface of the model.

7.5.1 Global errors and global error estimations

The accuracy of the recovered currents are quantitatively evaluated by looking at the global error in relation to the reference solution. This error is calculated as

$$||\mathbf{J}^{\text{ref}} - \tilde{\mathbf{J}}^*||_{ASL^1(S)}. \tag{7.28}$$

Table 7.1: Global current errors in relation to the reference solution.

Current distribution	Error: $\|\|\mathbf{J}^{\text{ref}} - \tilde{\mathbf{J}}^*\|\|_{ASL^1(S)}$
Original solution (substitute $\tilde{\mathbf{J}}$ for $\tilde{\mathbf{J}}^*$)	0.002326
$\tilde{\mathbf{J}}_{\text{div},\perp} + \tilde{\mathbf{J}}_{\text{tree}}$	0.002218
Mixed second-order (potential-based)	0.002106
Full first-order (vector-based)	0.002085
Mixed second-order (vector-based)	0.001866

The results are reported in Table 7.1 in order of decreasing error, with the first entry being the global error of the original solution.

The first thing to note is that all the recovered currents offer an improvement in accuracy, when compared to the reference solution $\mathbf{J}^{\text{ref}}$. The recovery of the divergent component only is the least effective at reducing the error, while the mixed second-order vector-based recovery, where both the divergent and solenoidal components are recovered, is the most effective. The potential-based solenoidal recovery procedure is not very effective, and even in combination with the recovered divergent component, falls short of the full first-order vector-based recovered current distribution.

The global estimated errors $\bar{\eta}^*_{\mathbf{J}}$, as calculated with Equation 7.27, can be compared to the error in the original solution. The estimated global errors are reported in Table 7.2.

Table 7.2: Global estimates of the current error in the original solution.

Current distribution	Estimated error: $\bar{\eta}^*_{\mathbf{J}}$
$\tilde{\mathbf{J}}_{\text{div},\perp} + \tilde{\mathbf{J}}_{\text{tree}}$	0.000637
Mixed second-order (potential-based)	0.000963
Full first-order (vector-based)	0.000901
Mixed second-order (vector-based)	0.001169

Looking at the estimated global error values in Table 7.2, it is clear that the mixed second-order vector-based error estimate of 0.001169 is closest to the error in the original solution of 0.002326. It is also noted that all the estimators are underestimating the global error. This is however expected, and can be largely attributed to the inaccuracy of the recovered currents near the domain boundary.

7.5.2 Element-wise error estimations

The utility of a current error estimator, even if based on an improved current distribution, relies heavily on its ability to produce an accurate estimated error distribution. As such, the element-wise reference current error $\eta_{\mathbf{J}}^{\text{ref}}$, as shown in Figure 7.21, is considered.

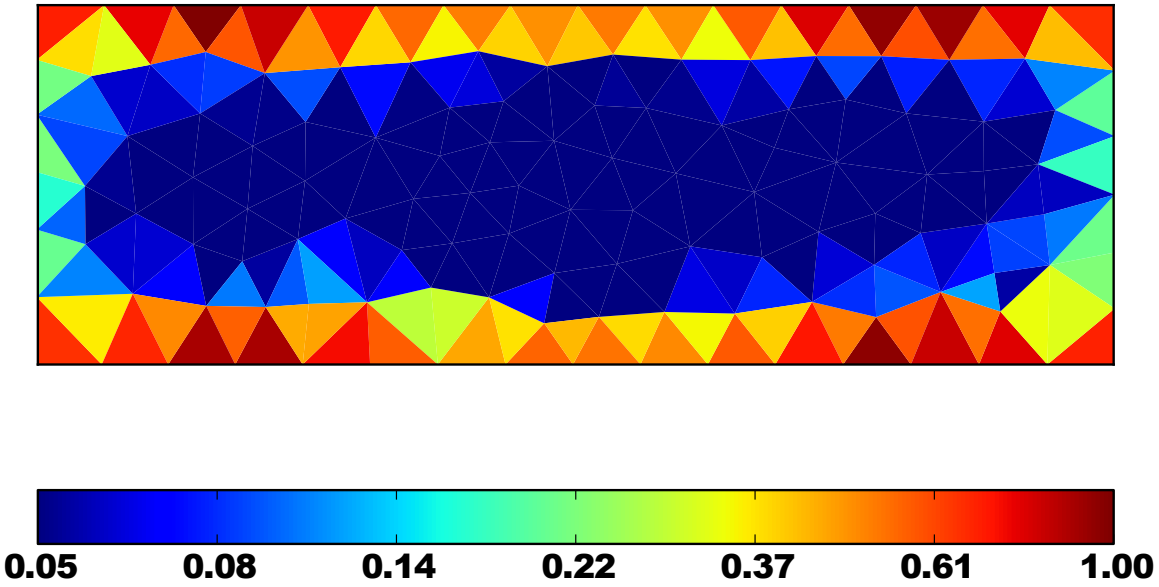

Figure 7.21: Element-wise reference current error distribution $\eta_{\mathbf{J}}^{\text{ref}}$ (log scale).

The data in Figure 7.21 is normalised with the maximum element error value, to aid in the visual comparison of estimated error distributions.

Now consider the estimated element-wise current error distributions, as obtained from the various recovery procedures, shown in Figure 7.22. Each error estimation plot is normalised with the maximum estimated element error, to aid visual comparisons. The accuracy of the recovered current used to construct the estimator should however be kept in mind. The plots in Figure 7.22 are once again ordered from the lowest to the highest accuracy of the underlying recovered current.

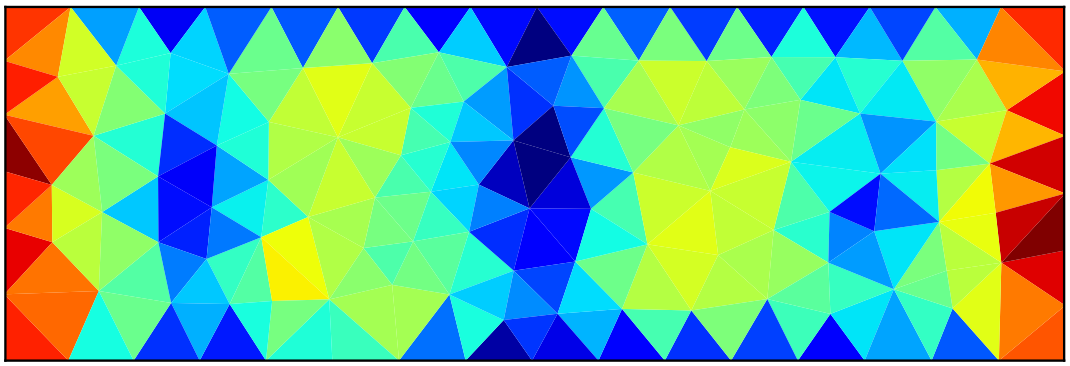

(a) $\tilde{\mathbf{J}}_{\text{div},\perp} + \tilde{\mathbf{J}}_{\text{tree}}$

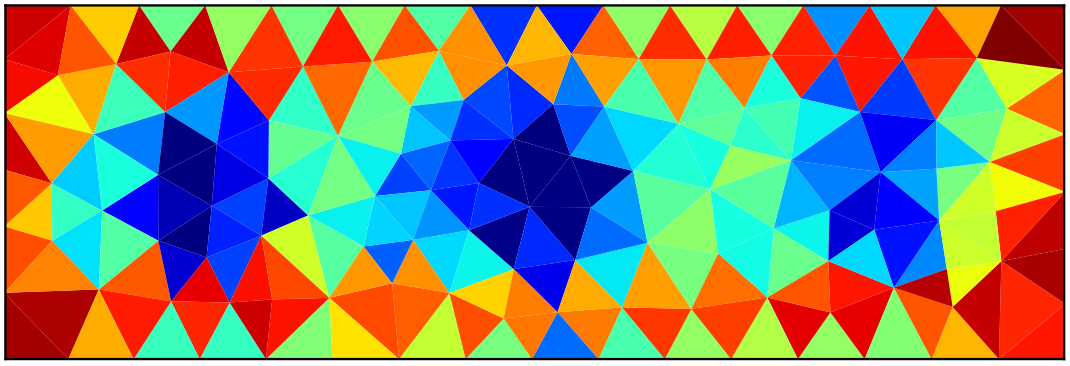

(b) Mixed second-order (potential-based)

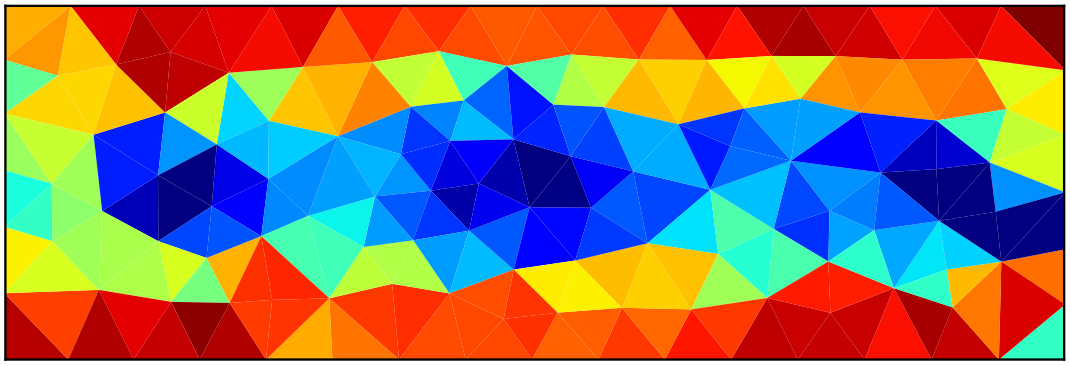

(c) Full first-order (vector-based)

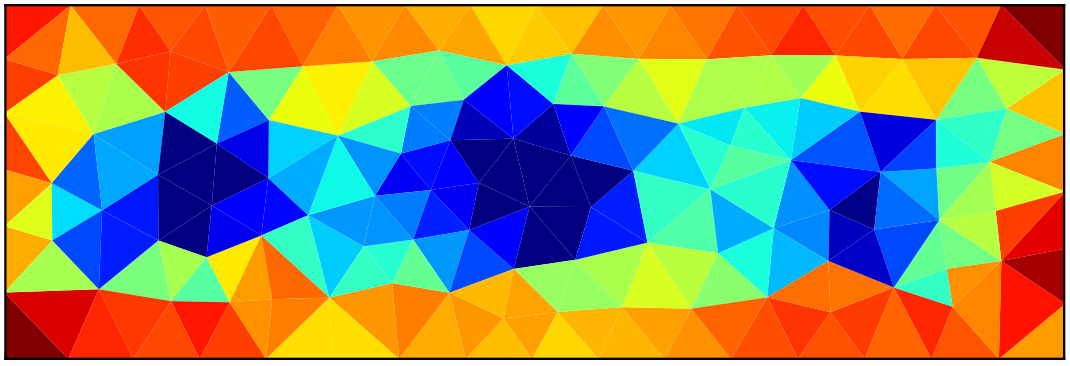

(d)Mixed second-order (vector-based)

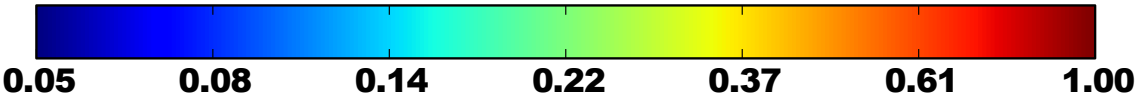

Figure 7.22: Element-wise current error estimations $\eta_{\mathbf{J}}^{*}$ (log scale).

The first two error estimators, although constructed from recovered current distributions with improved global accuracy, show weak correlation with the reference error distribution of Figure 7.21. This is largely attributed to the shortcomings of the recovered current distributions at the current peaks. The last two error estimators of Figure 7.22 show satisfactory performance. This can be attributed to the presence of the vector-based first-order solenoidal current component in the recovered currents used to construct these estimators. Both estimators can be used equally well to gain insight into the distribution of the true current error.

It would appear that there is little to choose from between the full first-order vector-based error estimator and the mixed second-order vector-based error estimator in terms of a qualitative analysis of the error distribution. The mixed second-order method is perhaps slightly more accurate in predicting higher error values all around the domain boundary, whereas the full first-order method predicted small errors on some boundary elements. The full first-order method does however offer a simpler implementation, at a lower computational cost. The mixed second-order estimator is known to be based on a more accurate current distribution than the full first-order estimator, and the predicted global error is also known to be more accurate. The best quantitative error estimator would thus be the one constructed on the mixed second-order recovered current.

7.6 Conclusions

This chapter dealt with the development of *a posteriori* current error estimation techniques for the MoM. The developed error estimators were based on current distributions recovered from a first-order RWG MoM solution. The recovered charge of the MoM solution, available from the work of the previous chapter, was implemented in a procedure with which a second-order divergent current component was recovered. The extracted zero-order solenoidal component of the first-order MoM current was also utilised in the recovery of a first-order solenoidal current component. Two new methods were developed for this purpose, a potential- and vector-based method, and the vector-based method was found to be the most accurate. Recovered currents with either the solenoidal or the divergent component of the original current solution left unchanged, were also constructed.

A full first-order recovered current, formed with the proposed vector-based recovered first-order solenoidal component and the original first-order divergent component, was found to lead to an adequate element-wise error estimator. The mixed second-order current, constructed from the recovered second-order divergent component and the same vector-based first-order solenoidal component, however resulted in an estimator with the best quantitative performance.

Chapter 8

Conclusions and Recommendations

Recovery-based error estimation, which is well-known in the FEM-context but is not at all explored for the MoM, was investigated in this thesis. A very accurate thorough implementation of the EFIE-based RWG MoM was developed and utilised as a platform for the testing of these error estimation schemes. Varying orders of Gaussian quadrature rules were utilised alongside singularity and near-singularity cancellation quadrature rules for the integrals involved in the MoM matrix element calculations.

Recovery based *a posteriori* error estimators for an RWG MoM charge and current were developed in this study.

A newly proposed recovery method, based on the characteristics of the RWG basis functions, was found to produce the most accurate recovered charge distribution of all the charge recovery methods investigated. This proposed recovery procedure has been accepted for publication in [31]. The global error was shown to be less in the recovered charge when compared to the global error in the original RWG-based charge solution. Both global and element-wise *a posteriori* error estimation was performed with the recovered charge distributions.

Error estimators based on recovered surface current distributions were also investigated. A second-order divergent current was constructed from the recovered first-order surface charge. This was added to a first order solenoidal current, calculated with a newly proposed vector-based recovery method, to compose a mixed second-order recovered current distribution. This recovered current was found to yield the highest accuracy of the investigated methods. Again, the global error was shown to be less in the recovered current as compared to the global error in the original RWG-based current solution. Global and element-wise *a posteriori* error estimation of the current was also illustrated.

The error estimation techniques developed in this thesis could find application within adaptive-refinement procedures. These procedures are desirable simulation tools that effect a desired reduction in the global error at the lowest possible computational cost,

through local refinement procedures at positions of high error.

Possible further research could include an extensive analysis of the associated computational costs of the recovery procedures, relative to the effected improvements in accuracy. The utility of a recovered current distribution as a substitute for the original solution current distribution could also be investigated. Such an investigation would involve an evaluation of the accuracy of derived quantities of the recovered current, such as antenna input impedance and near- and far-field values. The extension of the proposed methods to higher-order elements could also be investigated.

Appendix A

Linear Function Fit

Statement

A linear function has to be chosen on a triangular domain with the value fixed at the triangle centroid. If a least-squares fit to the three values at the midpoints of the edges of the triangle is done, the resulting plane will have the same gradient as the plane passing directly through the three points. An equivalent approach would thus have been merely shifting this plane to pass through the required centroid value.

Proof

Begin with a triangle and local axes set up so that one vertex of the triangle is at the origin and one edge falls on the **y**-axis, as shown in Figure A.1. Any arbitrary triangle

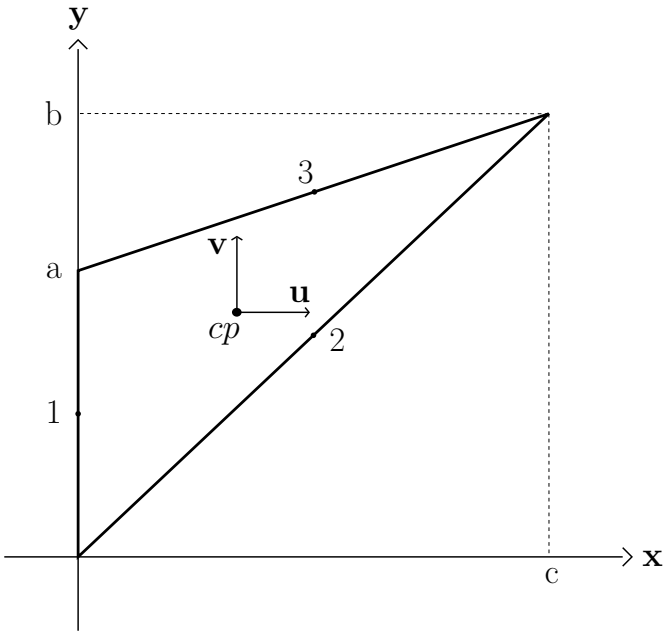

Figure A.1: Local coordinates for an arbitrary triangle.

may be defined by the three distances, a, b, and c, marked along the **x**- and **y**-axes. For the linear fit, use local coordinates $\vec{u}$ and $\vec{v}$, centered at the triangle centroid. The linear function on the triangle will have the form

$$\rho_{uv} = \rho_{cp} + uk_1 + vk_2 \tag{A.1}$$

with k_1 and k_2 to be determined from a least-squares fit to the following three values:

$$\begin{aligned} \rho_1 \quad &\text{at} \quad \left(-\frac{c}{3}, \frac{a-2b}{6}\right) \\ \rho_2 \quad &\text{at} \quad \left(\frac{c}{6}, \frac{b-2a}{6}\right) \\ \rho_3 \quad &\text{at} \quad \left(\frac{c}{6}, \frac{a+b}{6}\right) \end{aligned} \tag{A.2}$$

The least-squares model can be found as

$$\sum_{i=1}^{3} \begin{bmatrix} u_i^2 & u_i v_i \\ u_i v_i & v_i^2 \end{bmatrix} \begin{bmatrix} k_1 \\ k_2 \end{bmatrix} = \sum_{i=1}^{3} \begin{bmatrix} u_i \\ v_i \end{bmatrix} \rho_i$$

$$\begin{bmatrix} \frac{c^2}{6} & \frac{2bc-ac}{12} \\ \frac{2bc-ac}{12} & \frac{a^2-ab+b^2}{6} \end{bmatrix} \begin{bmatrix} k_1 \\ k_2 \end{bmatrix} = \begin{bmatrix} -\frac{c}{3}\rho_1 + \frac{c}{6}\rho_2 + \frac{c}{6}\rho_3 \\ \frac{a-2b}{6}\rho_1 + \frac{b-2a}{6}\rho_2 + \frac{a+b}{6}\rho_3 \end{bmatrix} \tag{A.3}$$

Solving this for k_1 and k_2 yields

$$\begin{aligned} k_1 &= -\frac{2}{c}\rho_1 + \frac{2b}{ac}\rho_2 + \frac{2a-2b}{ac}\rho_3 \\ k_2 &= -\frac{2}{a}\rho_2 + \frac{2}{a}\rho_3. \end{aligned} \tag{A.4}$$

Now the three values at the midpoints of the triangle edges can be extracted from the least-squares model as

$$\begin{aligned} \rho_1' &= \rho_1 + \left(\rho_{cp} - \frac{\rho_1 + \rho_2 + \rho_3}{3}\right) \\ \rho_2' &= \rho_2 + \left(\rho_{cp} - \frac{\rho_1 + \rho_2 + \rho_3}{3}\right) \\ \rho_3' &= \rho_3 + \left(\rho_{cp} - \frac{\rho_1 + \rho_2 + \rho_3}{3}\right) \end{aligned} \tag{A.5}$$

The value at each of the three points is altered by the same constant value. This can be seen to be the difference between the required central value and the central value of the plane that goes directly through the three points. Thus it is shown that the least-squares approach is equivalent to shifting a plane fitted to the three edge central values by the required value to match the triangle centroid.

Bibliography

[1] R. F. Harrington, *Field Computation by Moment Methods*. IEEE Press, 1993.

[2] A. F. Peterson, S. L. Ray, and R. Mittra, *Computational Methods for Electromagnetics*. Oxford & New York: Oxford University Press and IEEE Press, 1998.

[3] D. B. Davidson, *Computational Electromagnetics for RF and Microwave Engineering*, 2nd ed. Cambridge University Press, 2011.

[4] S. M. Rao, D. R. Wilton, and A. W. Glisson, "Electromagnetic scattering by surfaces of arbitrary shape," *IEEE Transactions on Antennas and Propagation*, vol. 30, no. 3, pp. 409–418, May 1982.

[5] L. Demkowicz, "Asymptotic convergence in finite and boundary element methods: Part 1: Theoretical results," *Computers & Mathematics with Applications*, vol. 27, no. 12, pp. 69–84, 1994.

[6] F. Bogdanov, R. Jobava, and S. Frei, "Estimating accuracy of MoM solutions on arbitrary triangulated 3-d geometries based on examination of boundary conditions performance and accurate derivation of scattered fields," *Journal of Electromagnetic Waves and Applications*, vol. 18, no. 7, pp. 879–897, 2004.

[7] K. F. Warnick and W. C. Chew, "Error analysis of the moment method," *Antennas and Propagation Magazine, IEEE*, vol. 46, no. 6, pp. 38–53, Dec 2004.

[8] U. Saeed and A. F. Peterson, "Local residual error estimators for the method of moments solution of electromagnetic integral equations," *Applied Computational Electromagnetic Society (ACES) Journal*, vol. 26, no. 5, pp. 403–410, 2011.

[9] M. Bibby and A. Peterson, "On the use of overdetermined systems in the adaptive numerical solution of integral equations," *IEEE Transactions on Antennas and Propagation*, vol. 53, no. 7, pp. 2267–2273, July 2005.

[10] X. Wang, M. M. Botha, and J.-M. Jin, "An error estimator for the moment method in electromagnetic scattering," *Microwave and Optical Technology Letters*, vol. 44, no. 4, pp. 320–326, 2005. [Online]. Available: http://dx.doi.org/10.1002/mop.20623

[11] M. Ainsworth and J. T. Oden, "A posteriori error estimation in finite element analysis," *Computer Methods in Applied Mechanics and Engineering*, vol. 142, no. 1, pp. 1–88, 1997.

[12] I. Babuska and W. C. Rheinboldt, "Error estimates for adaptive finite element computations," *SIAM Journal on Numerical Analysis*, vol. 15, no. 4, pp. 736–754, 1978.

[13] M. M. Botha and D. B. Davidson, "An explicit a posteriori error indicator for electromagnetic, finite element-boundary integral analysis," *IEEE Transactions on Antennas and Propagation*, vol. 53, no. 11, pp. 3717–3725, 2005.

[14] M. Botha and D. Davidson, "The implicit, element residual method for a posteriori error estimation in FE-BI analysis," *IEEE Transactions on Antennas and Propagation*, vol. 54, no. 1, pp. 255–258, Jan 2006.

[15] C. Carstensen, "Some remarks on the history and future of averaging techniques in a posteriori finite element error analysis," *ZAMM - Journal of Applied Mathematics and Mechanics / Zeitschrift fÃ¼r Angewandte Mathematik und Mechanik*, vol. 84, no. 1, pp. 3–21, 2004.

[16] D. W. Kelly, "The self-equilibration of residuals and complementary a posteriori error estimates in the finite element method," *International Journal for Numerical Methods in Engineering*, vol. 20, no. 8, pp. 1491–1506, 1984. [Online]. Available: http://dx.doi.org/10.1002/nme.1620200811

[17] O. C. Zienkiewicz and J. Z. Zhu, "The superconvergent patch recovery and a posteriori error estimates. part 1: The recovery technique," *International Journal for Numerical Methods in Engineering*, vol. 33, no. 7, pp. 1331–1364, 1992. [Online]. Available: http://dx.doi.org/10.1002/nme.1620330702

[18] T. L. Horváth and F. Izsák, "Implicit a posteriori error estimation using patch recovery techniques," *Central European Journal of Mathematics*, vol. 10, no. 1, pp. 55–72, 2012.

[19] M. Khayat, D. Wilton, and P. Fink, "An improved transformation and optimized sampling scheme for the numerical evaluation of singular and near-singular potentials," *Antennas and Wireless Propagation Letters, IEEE*, vol. 7, pp. 377–380, 2008.

[20] C. Geuzaine and J.-F. Remacle, "Gmsh: a three-dimensional finite element mesh generator with built-in pre- and post-processing facilities," http://geuz.org/gmsh/#Download, Version 2.8.5, released July 2014.

[21] "FEKO," http://www.feko.info, Suite 6.3, released September 2013.

[22] D. A. Dunavant, "High degree efficient symmetrical gaussion quadrature rules for the triangle," *International Journal for Numerical Methods in Engineering*, vol. 21, no. 4, pp. 1129–1148, 1985.

[23] S. Järvenpää, M. Taskinen, and P. Ylä-Oijala, "Singularity extraction technique for integral equation methods with higher order basis functions on plane triangles and tetrahedra," *International Journal for Numerical Methods in Engineering*, vol. 58, no. 8, pp. 1149–1165, 2003.

[24] M. M. Botha, "A family of augmented Duffy transformations for near-singularity cancellation quadrature," *IEEE Transactions on Antennas and Propagation*, vol. 61, no. 6, pp. 3123–3134, 2013.

[25] M. G. Duffy, "Quadrature over a pyramid or cube of integrands with a singularity at a vertex," *SIAM Journal on Numerical Analysis*, vol. 19, no. 6, pp. 1260–1262, 1982.

[26] J. P. Webb, "Hierarchal vector basis functions of arbitrary order for triangular and tetrahedral finite elements," *IEEE Transactions on Antennas and Propagation*, vol. 47, no. 8, pp. 1244–1253, 1999.

[27] J.-F. Lee, R. Lee, and R. J. Burkholder, "Loop star basis functions and a robust preconditioner for EFIE scattering problems," *IEEE Transactions on Antennas and Propagation*, vol. 51, no. 8, pp. 1855–1863, 2003.

[28] J. B. Manges and Z. J. Cendes, "A generalized tree-cotree gauge for magnetic field computation," *IEEE Transactions on Magnetics*, vol. 31, no. 3, pp. 1342–1347, 1995.

[29] S.-C. Lee, J.-F. Lee, and R. Lee, "Hierarchical vector finite elements for analyzing waveguiding structures," *IEEE Transactions on Antennas and Propagation*, vol. 51, no. 8, pp. 1897–1905, 2003.

[30] J.-F. Lee and D.-K. Sun, "p-type multiplicative schwarz (pmus) method with vector finite elements for modeling three-dimensional waveguide discontinuities," *IEEE Transactions on Microwave Theory and Techniques*, vol. 52, no. 3, pp. 864–870, 2004.

[31] W. J. Strydom and M. M. Botha, "Charge recovery for the RWG-based method of moments," *Antennas and Wireless Propagation Letters, IEEE*, 2014, DOI:10.1109/LAWP.2014.2362195.